Università degli Studi di Roma "La Sapienza"

PhD Thesis in Biophysics

Federico Giove

Energetics and Activation of the Central Nervous System by In Vivo Nuclear Magnetic Resonance

Supervisor:
Prof. Bruno Maraviglia

PhD Coordinator:
Prof. Alfredo Colosimo

XVII CYCLE – 2001/2004

Cover drawings: past and present of the brain activation studies. Front: BOLD–based functional map of a finger–tapping task performed by a motor–impaired patient, after rehabilitation. Back: first measurement of functional hemodynamic variations in the human brain (fluctuations of intracranial blood pressure monitored through a breach in the skull. The arrow indicates the beginning of a cognitive task. Angelo Mosso, Über den Kreislauf des Blutes im menschlichen Gehirn, Leipzig: Viet & Comp., 1881).

federico.giove@roma1.infn.it

Yo sueño que estoy aquí
destas prisiones cargado,
y soñé que en otro estado
más lisonjero me vi.
¿Qué es la vida? Un frenesí.
¿Qué es la vida? Una ilusión,
una sombra, una ficción,
y el mayor bien es pequeño,
que toda la vida es sueño,
y los sueños, sueños son.

Pedro Calderón de la Barca, *La vida es sueño*, Jornada II

Contents

Introduction

In the latest years, the contributions of the Magnetic Resonance (MR)[1] to the neuroscience were of fundamental importance, greatly increasing our knowledge of the human brain. Recent neuroimaging methods like Blood–Oxygenation Level–Dependent (BOLD) or perfusion–based functional imaging and Magnetic Resonance Spectroscopy (MRS), offer several chances for the knowledge of the function, and consequently the dysfunction, of the human brain.

In particular, functional Magnetic Resonance Imaging (fMRI) has been validated as a widely applicable and valuable tool for the scientific and medical investigation of the Central Nervous System (CNS). However, fMRI suffers from various theoretical and practical limitations, mainly related to its methodological approach, that relies on metabolic and vascular phenomena. In fact, the observed signal does not reflect directly the neuronal electrical activity, but it depends on the paramagnetic properties of deoxyhemoglobin (dHb): the local variations of dHb content modify the tissue T_2, thus resulting in a variation of opportunely weighted MR images. dHb content in tissues is in turn related to several parameters: vascular, such as blood flow and volume, and metabolic, such as oxygen consumption. The functional variations of such parameters, and their connections with neural activity, are still partially unknown, although there is some evidence of a strong connection

[1] For a list of all acronyms utilized in this Thesis, see the Appendix B at page 101. Acronyms are always defined at their first occurrence, and also afterwards when this is suggested by clarity reasons. Atomic symbols, measure units and non–scientific acronyms are not defined.

between neuronal electrical activity and BOLD signal [1, 2].

From a practical point of view, BOLD maps are characterized by poor temporal and not optimal spatial resolution: they are partially limited by the intrinsic Signal–to–Noise Ratio (SNR) of the method, but definitively by the vascular role in the signal generation, that introduces a temporal and spatial spreading of information [3].

In this framework, a depth knowledge of the brain energetic and vascular physiology is strictly required to optimize the use of current techniques.

As far as the vascular issue is concerned, the spinal cord is a possible, simplified model useful to study the characteristics of BOLD contrast; its vascular anatomy shows a remarkable axial symmetry, which allows a simpler modelling of fMRI signal. In the first Chapter, after a brief introduction to the physics of the BOLD contrast, we will discuss in detail the perspectives of spinal cord fMRI, and we will underline the medical consequences of a non–invasive tool for assessing the functionality of the injured spinal cord.

Drawing a comprehensive model of the physiologic–metabolic events underlying neuronal activity is impaired by the difficult assessment of the single dynamics of the parameters which generally influence the functional signals. As already emphasized, the BOLD effect, at the basis of the most widely used functional technique, results from the interplay of cerebral blood flow, cerebral blood volume and cerebral oxygen consumption. While the haemoglobin oxygenation has been evaluated with high spatial and temporal resolution through the BOLD contrast and optical methods, thus far the Cerebral Blood Volume (CBV) and Cerebral Metabolic Rate of Oxygen (CMR_{O_2}) have not been suitably quantified. A discussion on the role of these parameters for the investigation of the physiologic features of brain activation, and the relevant modelling studies, are given in the second Chapter.

A limited spatial and temporal resolution generally affects also the in vivo measures of important metabolites, such as glucose or lactate. This feature impairs the complete understanding of the basic events of the activation metabolism. Proton Magnetic Resonance Spectroscopy (^{1}H–MRS), in particular, is often used in the study of brain metabolism, in healthy subjects as well as in subjects suffering from several pathologies. In the latter case, studies are aimed to identify possible markers for the pathology characterization and diagnosis. The third Chapter is devoted to our approach to quantitative ^{1}H–MRS and to an application to a specific pathology, the so called Migraine With Aura (MWA).

As far as the metabolic issue is concerned, it was raised by the observation by Fox et al. [4, 5], obtained with Positron Emission Tomography (PET), regarding a focal mismatch between CMR_{O_2}, Cerebral Metabolic Rate of Glucose (CMR_{Glc}) and Cerebral Blood Flow (CBF) during prolonged neuronal activity. This phenomenon was called 'uncoupling' and, in the opinion of the authors, it would be the manifestation of anaerobic metabolism. To justify this assertion, they supposed that the aerobic capacity of neurons is already saturated during basal condition. Even though the hypothesis of non aerobic metabolism subserving neuronal activity was consistent with Fox's findings, it was not generally accepted by the scientific community (see, for example, [6]), above all because it appeared improbable that neurons were inefficient just when they must work.

Despite the above described limitations in the general knowledge of the basic events of the brain activation and in the techniques themselves, several models of activation have been proposed during the latest decade. Although none of them is able to give account of all the experimental (and controversial) evidence presented in literature, they constitute a valid basis for further developments.

A fundamental contribution in the interpretation of neuronal energetics was presented by Pellerin and Magistretti in 1994 [7]. These authors proposed that astrocytes have a pivotal role in neuronal metabolism, and that an Astrocyte–Neuron Lactate Shuttle (ANLS) could support brain energetics by conveying lactate from astrocytes to neurons. Consequently, lactate and not glucose was proposed as the principal metabolic neuronal substrate during functional activity. In this context, the importance of investigating the lactate variations in vivo is evident. Changes in lactate concentration have been reported by means of Nuclear Magnetic Resonance (NMR) spectroscopy upon prolonged stimulations, and an increase of lactate concentration has been detected by several authors during the first minutes of stimulation [8–10]. These kind of studies [8, 9] were initially performed to investigate Fox's hypothesis, as an increase of lactate concentration was expected in consequence of anaerobic glycolysis.

However, the above mentioned spectroscopic studies are not really crucial to determine the basic events of activation; this is due to the low temporal resolutions they achieved, and to the very prolonged stimulations applied, during which the metabolic processes surely reach some form of steady–state. Essentially, these studies were not able to detect the *metabolic dynamics*, that necessarily follow a shorter time–scaling.

A time–resolved ^{1}H–MRS strategy was implemented by us in order to measure the dynamics of lactate during the first seconds following a very brief stimulus [11, 12]; during this temporal scale, a transient lactate decrease was observed. This decrease was interpreted by assuming that the neuronal metabolism is aerobic from the early stage of their activation and that the beginning of functional activity is accompanied by lactate consumption. The fourth Chapter is entirely devoted to the discussion of the metabolic events of the brain activation.

CHAPTER 1

Functional Imaging of the Central Nervous System

1.1 An introduction to BOLD contrast

The BOLD contrast relies on the paramagnetic properties of deoxyhemoglobin, that acts as endogenous contrast agent. The increase of metabolism triggered by neuronal activity induces an enhancement of oxygen consumption and a subsequent increase of local blood flow and volume. The overcompensating increase of hemodynamic parameters produces an overall decrease of tissutal deoxyhemoglobin content and thus an increase of T_2 and $T_2^\star$; consequently, T_2 and $T_2^\star$–weighted images show an intensity increase in activated regions. Such an increase enables the localization of the underlying neuronal activity.

The locally increased blood flow in regions of the brain chat become active appears to be a consequence of increased energy utilization, mainly at the synapse [13]. Precisely which processes account for the metabolic changes is unclear. A major contribution to increased energy utilization may arise from metabolic changes in adjacent astrocytes with the uptake of the excitatory neurotransmitter, glutamate [14]. Astrocytes are abundant in the brain and are found in close proximity to the neurones. Elegant Carbon Magnetic Resonance Spectroscopy (^{13}C–MRS) experiments have suggested a $1:1$ coupling stoichiometry of oxidative glucose metabolism with glutamate neurotransmitter cycling between neurons and astrocytes [15]. However, it does not appear as though there is necessarily a simple relationship between increased energy utilization and increased blood flow. This is obvious particularly

with consideration of inhibitory synaptic activity. More work needs to be done to clarify the interpretation and mechanisms of coupling the hemodynamic response to neuronal activity.

These observations highlight a fundamental characteristics of the BOLD fMRI response. First, it should be useful for identifying changes activation–related in grey matter (where the synapses are found). Second, the changes measured reflect synaptic activity or a combination of synaptic and dendritic electrical changes, but not neuronal activity directly. Third, as cortical signal changes are triggered mainly by excitatory synaptic activity, at least under some conditions there should be a direct relationship between neuronal discharge rate and the magnitude of the BOLD signal. The exact nature of this relationship was clearly assessed by Logothetis et al. [1], that obtained simultaneous fMRI responses and intracortical recordings of neural signals in monkeys. They observed that the BOLD responses can be estimated from Local Field Potentials, thus suggesting that the BOLD contrast mechanism reflects the input and intracortical processing of a given area rather than its spiking output.

BOLD fMRI images signal contrast arises from changes in the local magnetic susceptibility. Normal blood can be considered simply as a concentrated solution of haemoglobin ($10 \div 15$ g/100 cm^3). When bound to oxygen, haemoglobin is diamagnetic, while deoxygenated haemoglobin is paramagnetic. Magnetic flux is reduced in diamagnetic materials, i.e. the applied magnetic field is repelled. Paramagnetic materials. in contrast, have an increased magnetic flux. A change in haemoglobin oxygenation therefore leads to changes in the local distortions of a magnetic field applied to it. Thulborn et al. [16] demonstrated that the T_2 of blood varies exponentially with the proportion of deoxygenated haemoglobin in a fashion precise enough to allow determination of blood oxygenation directly from the line width (which is proportional to T_2) of the water proton . The effect was shown to increase with applied magnetic held strength, as predicted for a phenomenon based on differences in magnetic susceptibility. However, it was Ogawa who described the first true Blood–Oxygenation Level–Dependent (BOLD) contrast imaging experiment with a report that gradient–echo MR images of a cat brain showed signal loss around blood vessels when the animal was made hypoxic [17]. This effect was reversed with normoxia. Ogawa then had the insight to suggest that the effect could be used to image the smaller changes in the blood oxygenation that accompany neuronal activation in the brain. In fact, the experiments of Thulborn (characterizing T_2 changes) and

Ogawa (characterizing $T_2^\star$ changes) define distinct phenomena, although they are related.

Increased oxygenation of blood gives rise to increased signal from water both in blood vessels and from the surrounding brain tissue, but the mechanisms are somewhat different. Both T_2 and $T_2^\star$ changes contribute to BOLD contrast.

As regards as the signal inside a vessel, this is effectively a single compartment. Water diffuses freely between red blood cells and serum, but cannot exchange across the vessel wall to a significant extent in the time course of a single Echo Time (TE) (typically 50 ms or less). However, during this time, a water molecule can diffuse in or out of a red blood cell. In consequence, its resonance frequency shifts because of the rapidly changing magnetic fields immediately around and inside each red blood cell. As the blood oxygen content decreases, the magnitude of these local magnetic field differences increases with the proportion of haemoglobin that changes from a diamagnetic to paramagnetic state. This gives rise to water Magnetic Resonance Imaging (MRI) signal decrease from a T_2 effect.

As regards as the signal immediately surrounding a vessel, with blood deoxygenation, extravascular water within a voxel located close to the vessel experiences a significant local field gradient across the voxel, the magnitude of which depends on the proximity and relative orientation of the vessel and the extent of the change in haemoglobin oxygenation.

In fact, modelling the vessel as an infinite cylinder with axis $\overrightarrow{a}$, the perturbation to B_0 in a point P outside the vessel can be expressed, in terms of angular frequency, as follows [18]:

$$\Delta\omega_B(P) = 2\pi\Delta\chi_0(1-Y)\omega_0\left(\frac{r_b}{r}\right)^2 sin^2(\theta)cos(2\phi), \tag{1.1}$$

where $\Delta\chi_0$ is the susceptibility difference corresponding to blood totally deoxygenated, Y is the fraction of oxygenated blood, r_b is the radius of the vessel, r is the magnitude of the distance $\overrightarrow{r}$ of P from the vessel, θ is the angle between $\overrightarrow{B_0}$ and $\overrightarrow{a}$, and ϕ is the angle between $\overrightarrow{r}$ and the component of $\overrightarrow{B_0}$ in the plane perpendicular to $\overrightarrow{a}$ that contains P. As it is apparent from Eq. (1.1), (and as it was repeatedly observed, see for instance [19]), the perturbation in P is maximal when the vessel is perpendicular to the static magnetic field and vanishes when the vessel is parallel to $\overrightarrow{B_0}$.

The variation in magnetic field across the voxel leads to signal dephasing and hence to a $T_2^\star$ signal loss. Additional T_2 loss occurs if the

water diffuses significantly through the field gradient. The ratio between T_2 and $T_2^\star$ components of the extravascular BOLD signal loss depends essentially from the size of the vessel: the $T_2^\star$ component prevails when the radial diffusion path of the water molecules is small related to the typical size of the vessel generating the gradient, or, in other words, in proximity of large vessels, while the T_2 component prevail in proximity of small vessels.

The model developed in 1993, Ogawa et al. [18] was able to successfully account for the main peculiarities of BOLD contrast, as the dependence on the kind of sequence utilized, the dependence on the orientation of the magnetic field, and the dependence on the degree of blood oxygenation. The physical analysis of BOLD phenomena has later been deepened also by other groups [20, 21], which described the BOLD signal in terms of static and dynamic averaging, differentiating between intravascular and extravascular effects. In any case, by simply considering the contribution of the extravascular spins [18], two important formulas can be derived:

$$R_2^\star = \alpha\{\Delta\chi_0\omega_0(1-Y)\}b_{Vl} \quad \text{(large vessels)} \tag{1.2}$$

$$R_2^\star = \eta\{\Delta\chi_0\omega_0(1-Y)\}^2 b_{Vs}p \quad \text{(small vessels)} \tag{1.3}$$

where $R_2^\star = 1/T_2^\star$, α and η are constants, $\Delta\chi_0$ is the maximum susceptibility difference which is expected in the presence of fully deoxygenated blood, ω_0 is the static magnetic field in angular units, Y is the fraction of oxygenated blood, b_{Vl} and b_{Vs} are the blood volumes for large vessels and small vessels, p is the fraction of active small vessels (i.e. filled with dHb–containing red blood cells). Eq. (1.2) and (1.3) have the key features of linking the measured signal with those physiological parameters, which vary during activation. The deoxygenated blood fraction $1-Y$ is related to oxygen consumption and blood flow according to $1 - Y = \mathrm{CMR_{O_2}}/\mathrm{CBF}$. From Eq. (1.2) and (1.3) it is evident that an increase of blood volume or oxygen consumption results in a signal decrease, while a CBF increase corresponds to a signal rise.

During neuronal activation, a positive signal peak is detected in the activated region (for example, see [22]). Whereas this observation is unquestionably related to a decrease of dHb content, how such a decrease in dHb occurs is not clear. In fact, while it is widely accepted that CBF and CBV rise during activation, the entity of the elevation of $\mathrm{CMR_{O_2}}$ is not definitively established. Previous data, obtained by means of PET [4, 5], indicated a small increase of $\mathrm{CMR_{O_2}}$ $(+0 \div 5\%)$ compared to the

large increase of CBF ($+30 \div 50\%$) during elevated neuronal activity. Qualitatively, the BOLD signal increase is certainly consistent with this finding when considering the extravascular effects alone. Nonetheless, the changes in neuronal physiology in response to a stimulation remains a matter of intense debate, since the BOLD signal derives from the multiple interaction of CBF, CBV and CMR_{O_2}, each of which may have a characteristic temporal behavior.

When high temporal resolution and sensitivity is achieved, the BOLD signal can show a complex time–course. In addition to the large, well–studied signal rise usually detected in order to assess the activated areas, an early (weak) dip of the signal within the first 3 s was observed by some groups at high magnetic fields [23–27], and also (but with scarce reproducibility) at 1.5 T [28]. For stimulation longer than 4 s, moreover, a signal decrease below the baseline was seen towards the end of the time–course. This later undershoot was observed even in the very first fMRI papers, and probably originates from the different time–scales necessary to CBV and CBF to recover the basal condition (volume effects).

The initial dip of the BOLD signal proves very interesting in what it tells us about the dynamical coupling of oxygen metabolism and blood flow. It can be interpreted in terms of an early increase in oxygen metabolism accomplished by an increase in oxygen extraction before the flow increase has started, as suggested by Malonek and Grinvald [6]. Nonetheless, in principle, the initial dip could simply derive from volume effects [29, 30]: an initial dip would indeed result if blood volume reacts more rapidly than blood flow, without making any particular hypothesis about the evolution of oxygen consumption.

Changes in $T_2^\star$ relaxation times for extravascular water become greater with higher imaging magnetic field strength, but for large vessels the increase is linear and for small vessels the increase is quadratic (see Eq. (1.2-1.3)) . Thus, at higher magnetic fields the contribution of small vessels should increase [3, 31]. However, at usual clinical 1.5 T field strengths, there is a major intravascular component which can limit the accuracy with which an activation volume in the brain parenchyma can be mapped.

1.2 Towards a simplified model: fMRI of the spinal cord

The fMRI based on BOLD contrast [1, 17, 32–35] has gained a primary role in the study of human brain, both for the characterization of normal

brain activity and in clinical practice. After its introduction in the early Nineties, the BOLD–based functional imaging was widely utilized for non–invasive studies on human brain function; up to now, however, only few studies of the human spinal cord by functional imaging have been presented, starting from the work published in 1996 by Yoshizawa et al. [36], with a subsequent strong contribution of Stroman et al. [37–45].

Even if the complex interplay of phenomena producing the BOLD contrast in brain is still under investigation, it is expected that similar phenomena should appear also in the spinal cord, and techniques based on the standard BOLD contrast should be in principle applicable also to the spinal cord, thus revealing areas of spinal activation in correspondence of a given task involving peripheral nerves activity. In particular, a motor task should activate motor neurons, in the anterior horns of the spinal grey matter, while sensory and proprioceptive input produces diffused response, with synapses in different locations [46], mainly in the posterior horns (Fig. 1.1). A second source of functional contrast has been hypothesized as active in the spinal cord fMRI: the so–called Signal Enhancement by Extravascular water Protons (SEEP) [41]. The same contrast was observed also in the brain [43, 47, 48].

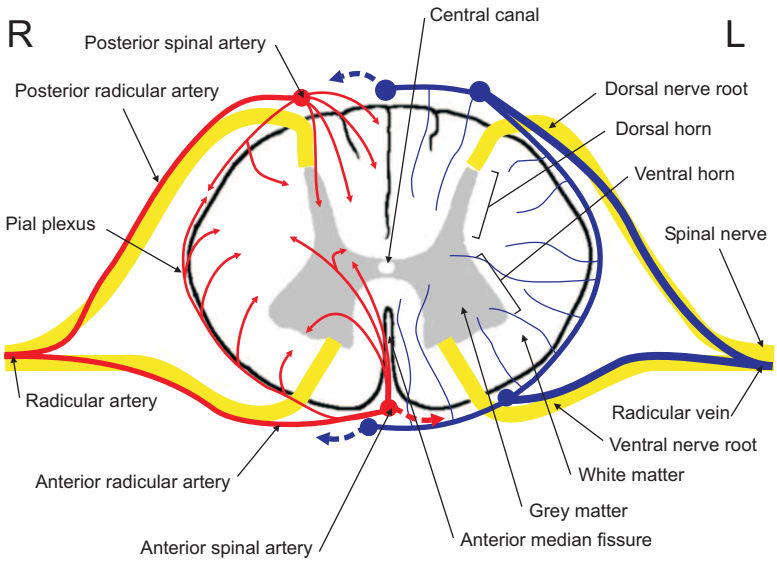

Figure 1.1: Schematic of the human spinal cord. For clarity reasons, arteries are drawn only on the right side of the cord, veins only on the left. From [49].

The current knowledge on spinal cord function is based on invasive

neurophysiology experiments, mainly on cats and primates [50]. At moment, no adequate and reliable methods are widely available for the non–invasive clinical evaluation of spinal function. The regular application of fMRI of human spinal cord would be of great importance in the clinical practice, in particular for the assessment of functionality after injuries, especially when patients are unable to report sensation or to produce a movement, for the follow–up of the treatments, for the design and assessment of rehabilitation programs. Moreover, the study of spinal activity anomalies, also upon electric nerve stimulation, could improve the comprehension and the treatment of chronical pain.

In the recent years, several progresses have been made in the treatment of spinal injuries; the recent technical advances, like the regeneration of damaged neural tissue after injuries up to now considered intractable [51–60], require a reliable method to assess the recovery of functional activity.

A challenging perspective would be the integration of current knowledge of spinal cord neuroanatomy with several different magnetic resonance measures, like fMRI, ordinary imaging, MRS, Diffusion Tensor Imaging (DTI). In particular, MRS can provide useful data on spinal cord metabolism, while DTI can give information on spatial and causal relations between activated regions. MRS [61, 62] and DTI studies [63–70] on human spinal cord have been conducted so far, demonstrating the feasibility of such techniques in this problematic region.

Spinal cord activation has been observed in cervical and lumbar spinal cord, for both sensory stimulation [37–42, 44–46, 71] and motor task [36, 38, 39, 45, 46, 71]. Spatial specificity for the stimulation of different dermatomes has been shown [40] and also the differentiation of motor and sensory areas was observed, although large overlaps were found (see page 24 for a discussion on the spatial localization of signal and Table 1.1 for a global survey of spinal cord fMRI experiments published so far). However, obtaining BOLD images of the spinal cord activation still remains a technical challenge. This is due mostly to the small cross–sectional area of the spine, to cardiac–related motion of Cerebro–Spinal Fluid (CSF) and of spinal cord itself [72–75], and finally to the susceptibility artifacts, related to the proximity of tissues with different magnetic properties (e.g. the vertebral processes [62], and organs like lungs, that have variable volume and several tissue–air interfaces).

Table 1.1: Summary of fMRI experiments on human spinal cord.

Ref.	Sequence	Region	Field/coil
[36]	FLASH–2D (FC), TE/TR = 40/190 ms, FA = 40 °, FOV = 200 mm, 256 × 256	S C7–C8	1.5 T/neck coil
	Fist clenching of the right hand @ 2 Hz.		
[37]	A: Modified FLASH (FC, †), TE/TR = 30/80 ms, FA = 30 °, FOV = 200 mm, 256 × 128	S C8	3 T/surface coil (⌀ 17 cm)
	B: Modified FLASH (FC, †), TE/TR = 30/80 ms, FA = 30 °, FOV = 200 mm, 256 × 128	*Sagittal*	
	Squeezing a rubber bulb with the dominant hand @ 1 Hz. † : Spatial selective pulses outside the imaging slab, breath holding during acquisition.		
[38]	A: GE EPI (FC, SSP, ‡), TE/TR = 31/5000 ms, FOV = 100 mm, 64 × 64	B C6–T1	1.5 T/surface coil
	B: SE EPI (FC, SSP, ‡), TE/TR = 34/5000 ms, FOV = 100 mm, 64 × 64		
	Squeezing a rubber bulb with the hand @ 1 Hz (A–B). Blowing puffs of air onto the center of one hand (A). ‡ : Images acquired only after end–expiration.		
[39]	SSFSE (FC, SSP), TE/TR = 36, 66, 96/7000 ms, FOV = 120 mm, 128 × 128	B C6–T1	1.5 T/phased–array spine coil
	Squeezing a bulb with one hand (left and right in separate experiments) @ 1 Hz. Thermal stimulation with a bag of cool (5 ÷ 7°C) water on the palm of one hand (left and right in separate experiments).		
[71]	GE EPI (RS), TE/TR = 50/3000 ms, FA = 90 °, FOV = 140, 160, 200 mm, 128 × 128	B C4–T2	1.5 T/neck coil
	Flexing the forearm about the elbow from 0 °to 90 °and back (1 ÷ 2 Hz). Wrist extension task with clenched fist (1÷2 Hz) Fingers abduction–adduction task (1 ÷ 2 Hz) Holding random weights (from 0.3 to 1.2 kg) in one hand, with fixed flexed–arm position, 30 s for each weight.		
[46]	A: Multishot EPI (SSP, §), TE/TR = 50/68 ms, FA = 15 °, FOV = 250 mm, 128 × 128,	*Sagittal*	1.5 T/neck coil
	B: Multishot EPI (SSP, §), TE/TR = 50/100 ms, FA = 30 °, FOV = 250 mm, 256 × 256,	B C6–C7	
	Alternated fist clenching @1 Hz. Alternated electrical median nerve stimulation at the elbow @ 1 Hz. § : Cardiac gating.		
[40]	SSFSE (SSP), TE/TR = 38/9000 ms, FOV = 120 mm, 128 × 128	B C4/C5–T1	1.5 T/phased–array spine coil
	Thermal stimulation provided by circulation of water (5 ÷ 7°C, 30 ÷ 32°C) in coils of rubber tubing in contact with three different sensory dermatomes on the right hand and forearm.		
[41]	FSE (FC), TE/TR = 11, 22, 44, 55, 66/3000 ms, FOV = 120 mm, 128 × 128	S C6–C8	1.5 T
	Thermal stimulation provided with a cold pack (7°C) placed on the palm of the right hand.		
[42]	SSFSE (FC, SSP), TE/TR = 34/8250 ms, FOV = 120 mm, 128 × 128	S L1–L5	1.5 T/phased–array spine coil
	Thermal stimulation provided by different temperatures probe (2 ÷ 32°C) placed on the inner calf.		
[44]	SSFSE (FC, SSP), TE/TR = 34/8250 ms, FOV = 120 mm, 128 × 128	S T11–L2	1.5 T/phased–array spine coil
	Thermal stimulation provided by different temperatures probe (10 ÷ 32°C) placed on the inner calf.		
[45]	SSFSE (SSP), TE/TR = 42.3/11000 ms, FOV = 120 mm, 128 × 128	S S3–L1	1.5 T/phased–array spine coil
	Rhythmic flexion and extension movements (active and passive) of the ankles with a pedaling device.		

The table contains the main parameters of all spinal cord fMRI experiments published on journals, in chronological order. Ref.: reference of the study; Sequence: pulse sequence with relevant parameters and (between parenthesis) additional settings; Region: localization of slices, reported as spinal cord segments (S) or vertebral bodies (B); Field/coil: Magnitude of the magnetic field and receiver coil utilized; FC: Gradients for the compensation of flux through slices; SSP: Spatial Saturation Pulses; RS: Ramp Sampling. Slices are axial or perpendicular to the spinal cord if no otherwise stated. Also a brief description of the task executed by the subject is given. From [49].

1.2.1 Technical challenges

Vasculature

The spinal cord receives blood from 3 major arteries that run through the length of the cord, one anterior spinal artery that lies in the anterior median fissure, and two posterior spinal arteries that run near the dorsal roots entry zones (Fig. 1.1, in red). The anterior spinal artery branches and penetrates into the grey matter of the cord by way of the anterior median fissure. It supplies the anterior two–thirds of the cord. Posterior spinal arteries supply the dorsal white matter and the dorsal horns, for about one–third of the cord. There is a limited anastomosis between the anterior and posterior spinal arteries. The spinal arteries receive blood from segmental radicular arteries which enter the vertebral canal through intervertebral foramina, continue along the nerve root and branch into anterior and posterior radicular artery, which join the spinal arteries. There are numerous anastomoses among spinal and radicular arteries. Together, they form an irregular net of arteries and arterioles on the surface of the pial matter called the pial plexus. Radicular arteries arise from large vessels outside the vertebral column, such as cervical arteries, intercostal and lumbar branches from the abdominal and thoracic aorta [76]. Therefore larger arteries (diameter $0.1 \div 0.2$ mm) lie externally to the spinal cord, and have longitudinal symmetry, while only small arterioles (maximum 50 μm) penetrate radially into the cord.

The veins draining the spinal cord (Fig. 1.1, in blue) are arranged roughly like the arteries. There are usually 3 anterior and 3 posterior (in general larger) spinal veins, one medial and two lateral, that run longitudinally. They communicate freely and drain into radicular veins that cross the subarachnoid space attached to the nerve roots, like the radicular arteries. Radicular veins course into the epidural plexus and join veins of the vertebral bodies. There, they run to the vertebral, intercostal, lumbar and sacral veins. Also for veins, the main vessels are external to the cord and longitudinally disposed, while the internal drainage is provided by small, radial venules (diameter less than 50 μm) [76].

This particular distribution of large vessels, only on the surface of the spinal cord, should enhance the specificity of BOLD signal, even with $T_2^\star$–weighting, due to the inherent elimination of the confounding, unspecific effect of larger vessels [77] from the grey matter signal. Nonetheless the small cross–sectional diameter of the spinal cord makes possible the large pial vessels to obscure the weaker signal from inside

the cord, especially if motion artifacts are not under control.

However, the BOLD signal arising from large venous vessels should be greatly reduced, due to their axial symmetry, parallel to the static magnetic field $\overrightarrow{B_0}$. Similarly, the disposition of small vessels, all radial and thus orthogonal to $\overrightarrow{B_0}$, should emphasize the dephasing effect of deoxyhemoglobin. (see Eq. (1.1)); moreover, the intravascular contribution can be neglected for large vessels, as they lie externally to the spinal cord.

Therefore the vascular anatomy of spinal cord is optimally organized for the generation of strong and spatially specific BOLD effect. This can help in overcoming the numerous other difficulties that involves the spinal cord fMRI. However, it must be pointed out that some cases of activation following the shape of small radial veins have been reported [71].

Motion artifacts

The motion of CSF and spinal cord during cardiac and respiratory cycles produces significant degradation of the functional MR signal. Although the different motions are related to physiological rhythms and not to the stimulation paradigm, partial volume effect can mimic the functional contrast via partial volume averaging, especially at the boundary of spinal cord with CSF and with the main vessels. The onset of partial volume averaging contrast at the boundary of white and grey matter appears less serious, given the low imaging contrast generally obtained between grey and white matter [45]. In this case, the more prominent effect would be rather a decrease of functional contrast, due to the average of active grey matter with white matter zone, that doesn't show signal increase.

Motion artifacts arise from several correlated factors: blood and CSF flux, motion of spinal cord itself [72, 78] and body movements, enhanced by the intrinsic mobility of the spinal cord [73]. Internal body movements are mainly respiratory related, but unfortunately there is also a task–related component (especially for motor tasks or with nerve stimulation) that can be managed with more difficulties than in conventional brain fMRI. This fact introduces the further problem of possible misregistration of images, likely to occur also due to the inhomogeneity of surrounding tissue. Task–related movement artifacts were observed on the cord surface, within large vessels and within neck and shoulder muscles [37, 42, 46]. Very often the functional analysis was conducted only inside

the spinal cord tissue, thus masking external artifactual activations.

In particular, the peak velocity of CSF, reported to be about 3 cm/s (see below, page 16) can easily cause the inflow of unsaturated CSF. Even if in the typical slice acquisition time the CSF can cover at most one fourth of the slice thickness, the TR utilized generally allows a complete CSF turnover in the slice slab.

A further complication for the application of spinal cord fMRI in clinical routine is introduced by pathological movements of the spinal cord, that are possibly larger, faster or simply different from the normal ones, especially in compressive or degenerative diseases [74, 79, 80]. The effects on quality of functional images are still unknown.

It has been suggested that the motion contribution to the signal can be assessed at the spinal cord boundary, as the relative increase of signal due to motion artifacts is greater than the true BOLD signal in a ratio of at least 2 : 1 and has a greater variance [37, 45]. Sometimes, the excessive magnitude of the contrast was assumed as a proof of motion and thus utilized to exclude regions of artifactual activation [37, 38, 45], but this approach is clearly unsatisfactory as it merely excludes the more gross errors. Functional increases of signal as large as 12% [46] and 18% [45] at 1.5 T have been reported, and a substantial contribution of task–related motion is supposed to contribute to such conspicuous variations.

The proposed approaches to reduce the quality degradation due to motion rely mainly on subject constrain, breath holding and cardiac triggering of the scans. Subject constrain was adopted [36, 37, 71] in the form of head and neck restraining. Breath holding was sporadically adopted [37, 38] to minimize the body movement and thus the related artifacts; moreover, it reduces the susceptibility issues arising from lungs volume variation. Nevertheless, breath holding can negatively affect the functional imaging because it influences the hemodynamic and blood oxygenation, and its effectiveness relies on the subject ability in maintain uniform lounge volume during the repeated breath holdings, so the real advantages and consequences of this maneuver are not clear. Cardiac triggering [46] permits to acquire slices with the most reproducible saturation conditions of CSF, thus reducing the confounding effect of unsaturated CSF inflow. However, the effects of task–related variations of blood pressure cannot be avoided.

A further approach to motion artifacts relies on reducing the pixel dimension, to improve the in–plane resolution. In fact, keeping small the pixels reduces partial volume averaging and helps the recognition of confounding structures, like vessels. Nevertheless the SNR decreases

and can become too low, even when maintaining a comparably larger slice thickness.

The software registration of images was always performed, sometimes in the k–space [37, 39]. The rigid body rototranslation approach was generally adopted. In order to minimize the effects of the shape or tone changes of surrounding tissues, in particular muscles, the registration procedure was often restricted to the spinal cord zone [36, 37, 39, 41, 42, 44, 45]. The resampling of the images has been also adopted to optimize the spatial registration algorithm. [36, 37, 39]. Indeed, this stratagem, that corresponds to a zero–filling in the k–space data, can minimize the calculation errors for sub–pixel movements. A further proposed post–processing step is the spatial averaging between adjacent slices [38], that is expected to reduce the problems related to CSF flow, but at the expense of loss of specificity and sensitivity.

Motion related artifacts can be minimized by acquiring the fMRI time series time–locked with the relevant physiological parameters, respiration [37, 38] and cardiac pulsation [46]. In particular, the oscillating CSF pulsation is a response to the transient increase of intracranial blood volume during the cardiac cycle. The arterial inflow of blood has an early systolic peak about 100 ms after the R wave of the ECG, while the venous outflow is almost continuous with only a subtle diastolic flow increase in the internal jugular vein. By considering the brain as the main pump for the circulation of the CSF, an increased systolic intracranial blood volume occurs mainly in the richly vascularized compartments of the brain. This causes the expansion of the grey matter and then the compression of the intracranial subarachnoid space surrounding the cerebral hemispheres. Therefore, a large volume of CSF is initially displaced from the subarachnoid space into the cervical spinal canal immediately after the inflow of systolic blood [72]. The downward flow of CSF in the cervical spinal canal is delayed of about $100 \div 200$ ms compared to the arterial inflow [81].

In normal subjects, the caudally directed (systolic) CSF flow in the anterior subarachnoid space reaches its maximum velocity immediately after the beginning of the pulsation. In the literature, CSF velocity in the cervical spine is reported to range from 0.8 cm/s to 4.0 cm/s. The diastolic reflux is significantly slower [72, 82, 83]. The velocity decreases as the CSF descends the spinal axis. The maximal velocity in healthy volunteers occurs in the cervical area, at the C4–C5 level, and this is probably due to the fact that at this level the spinal cord has the maximum section and the subarachnoid space is minimum. In the lumbar

area, because the spinal cord extends only to the L2 level, leaving a large subarachnoid space for CSF flux, the velocity is significantly lower.

The periodic changes in CSF flow with the cardiac cycle have a frequency of about 1 Hz. In the cervical canal, this cardiac–related CSF pulsation is superimposed upon an additional bulk component with a period of several seconds, identified as related to inspiration and expiration. The respiration–induced modulation of cardiac–related CSF flow is subtle during normal respiration but clearly increases during forced respiration. The respiration–related flux is directed mainly downwards in the anterior subarachnoid space, upwards laterally. In addition, it can be shown that the opposed components of CSF flow are not only anatomically separated, but they alternate with time: caudal CSF flow in the anterior cervical subarachnoid space dominates during inspiration, whereas expiration is accompanied by an increase in cranial flow. The increase of caudal CSF flow in the anterior cervical subarachnoid space can be identified immediately after inspiration begins [72, 73].

The aforementioned knowledge suggests that the better approach to motion artifacts reduction should be the acquisition of functional images at about half of the interval between two consecutive hearth pulsations.

Pulsatile movement of both the brain and spinal cord is routinely observed during neurosurgical intervention that involves the central nervous system. Data obtained in healthy subjects indicate that the cervical spinal cord moves in a craniocaudal oscillatory damped pattern after cardiac systole. The alternating cranial and caudal spinal cord displacement and velocity decrease to zero in the late cardiac cycle. This pattern of oscillation differs from person to person. Measurements obtained about 100 ms after cardiac systole showed that the spinal cord moves first caudally, at a velocity of about 7 mm/s; this movement is followed (about 160 ms after systole) by a cranial oscillation, with lower velocity (about 3 mm/s), while CSF is still moving in caudal direction. The measurement of caudal displacement of the spinal cord suggest a maximum displacement of approximately $0.5 \div 1$ mm. No definite motion is seen in the middle thoracic spinal cord. Transverse velocities may exist within the spinal cord because of CSF pulsatility and systolic inflow within the spinal cord tissue [75, 84–86].

Susceptibility artifacts

The quality of spinal cord functional maps is affected by local field strong inhomogeneities arising from many different tissues adjacent to

the spine, in particular bone [37]. Cooke et al. [62] recently mapped B_0 inside the cervical spinal cord at 2 T, showing local distortions especially in proximity of spinous processes, with spatial periodicity roughly equal to the length of the vertebral bodies. Nonetheless, B_0 is relatively uniform in the center of spinal cord and, as it is easy to guess, the observed water linewidth decreased when spectroscopic voxel was shorter in the Inferior–Superior ($\overrightarrow{z}$) direction, thus symmetrically spanning the minimum number of interspinous spaces. These results strongly suggest to set the imaging slices perpendicular to the bone and to adjust their thickness and spacing so that each slice covers a vertebral body or an intervertebral disc, avoiding the boundary zones between bone and connective tissue.

Spinal cord fMRI was demonstrated in cervical and lumbar segments, but not in correspondence of thoracic segment lower than T2. Below this level, images quality and stability is compromised, probably by lung and larynx motion, blood flow in the carotid artery, air in the trachea [36].

Sequence–related issues

At moment, a well established protocol for fMRI studies in spinal cord doesn't exist, nonetheless T_2–weighted images were often obtained with Single Shot Fast Spin Echo (SSFSE) sequence [39, 40, 42, 44, 45], that suffers less than spin–echo Echo Planar Imaging (EPI) of quality problems, provides an overall better temporal resolution and is not contaminated by $T_2^\star$-weighting, intrinsic in EPI imaging.

The sequence–related strategies most widely utilized to minimize the effects of CSF flux and disturbing tissues are the presaturation of tissue outside the imaging slab and the employing of gradients in the through–slices direction for the flow compensation [36, 38–40, 42, 44–46], but also the use of more sophisticate strategies is reported. Stroman et al., to maintain the same magnetization steady state inside and outside the imaging sections, applied spatial selective pulses on sections 7.5 cm–thick outside the imaging slab with a flip angle equal to the flip angle of the slice selective pulses of functional imaging [37]. In order to minimize imaging artifacts due to long CSF T_1, they utilized linear phase encoding with Fast Low Angle SHot imaging (FLASH). This strategy allows to obtain a steady state magnetization in CSF while most of the k–space is sampled. The increased sensibility of this sequence to inflow enhancement was managed with the aforesaid spatial selective pulses, also in consideration of the absence of large vessels inside the spinal

cord (see above, page 13). Nonetheless, this approach is reasonable only for single slice imaging.

1.2.2 Signal characteristics

Signal magnitude and time–course

The maximum increase of fMRI signal, averaged on activated areas, has been often evaluated (see Table 1.2 for a list of available measures), and generally is stronger than in brain. See below, page 21, for a discussion on this feature. The magnitude of BOLD response appears to be fairly

Table 1.2: Functional increase of fMRI signal in the human spinal cord.

Ref.	Signal increase		Task	Sequence
	contralateral	ipsilateral		
[36]	5%	2%	Fist clenching	FLASH
[37]†	7%		Rubber bulb squeezing	FLASH
[38]	3.8 ÷ 5.7%		Rubber bulb squeezing	GE EPI
	4.8 ÷ 5.9%		Rubber bulb squeezing	SE EPI
	3.2 ÷ 5.5%		Blowing puffs on hand	GE EPI
[39]	9%		Rubber bulb squeezing, thermal stimulation	SSFSE
[71]	0.5 ÷ 7.5%		Various motor tasks	GE EPI
[46]	8 ÷ 12%		electrical stimulation, fist clenching	Multishot EPI
[40]	5%		Thermal stimulation	SSFSE
[41]	5 ÷ 6%		Thermal stimulation	FSE
[42]	2.6 ÷ 3.2% @29 ÷ 15°C		Thermal stimulation	SSFSE
	7.0% @10°C			
[44]‡	2 ÷ 3% @29 ÷ 15°C		Thermal stimulation	SSFSE
	8% @10°C			
[45]	15% active task		Motor task	SSFSE
	18% passive task			

The table reports the maximum per cent increase of fMRI signal observed during activation in ipsilateral and contralateral areas. Values in the middle are averages off all active areas, ipsilateral and contralateral. Values are intersubject averages, when applicable. Data acquired at 1.5 T, except † : 3 T. ‡: data partially in common with [42]. See Table 1.1 for TE and further details on experimental procedures and task. From [49].

independent of the side, dominant or not, of motor task or sensory stimulation for hand exercises done in the same experimental conditions [38], with a possible slight enhancement of magnitude of motor activation

with non dominant hand [38].

The strength of signal depends on the intensity of stimulus. Stroman et al. observed an essentially biphasic dependence of per cent signal change on the temperature of thermal stimulus: the response slightly increases when lowering the temperature from 29°C to 15°C, while below this temperature the response is much larger [42, 45]. This feature has been related to the superimposition of the responses of two classes of neurons identified in monkeys: high–threshold cold receptors, that discharge at a rate linearly increasing with temperature decrease, and should account for the slowly varying response, and mechanothermal nociceptors, whose discharge rate increases rapidly below 20°C, and should contribute to the sharp increment of response below 15°C [87, 88]. Madi et al. [71] observed a linear relationship between the force applied by the muscles during an isometric task (variable weight holding) and fMRI signal. Both positive and negative correlation were found, in different regions, while no voxel showing quadratic relationship was identified. Invasive electrophysiological studies reported linear relation between neural activity in the spine and contractile force [89]. In connection with this finding, the linear relation found by Madi et al. supports the existence of a linear transfer function between neural activity and fMRI signal in the spinal cord, as directly demonstrated in the brain by Logothetis et al. [1]. However a direct proof of such linearity is still lacking.

The temporal resolution of the studies is often limited by the temporal averaging or filtering [37, 39–41, 46, 71]. Stroman and Ryner [38] obtained the best temporal resolution, about 10 s, using EPI and the breath–holding to reduce motion. The poor temporal resolution is a strong limiting factor for the resolution of the shape of the transient phases of the hemodynamic response.

The time to reach the maximum effect is substantially longer than in brain, and has been evaluated in $20 \div 30$ s for motor task and in about 15 s for sensory stimulation [38]. The slow rise of signal during the stimulation has been regarded as an indirect proof that the observed variation is related to physiology and is not artifactual, as most confounding effects (like motion or task–related flow) should increase immediately after the onset of the task [38]. The ostensible slowness of fMRI signal during blocked tasks strongly suggests an impulsive hemodynamic response function (hrf) different and slower than in brain. The physiological reason for this feature is not clear, even if the SEEP enhancement has been involved (see below, page 21). It is nonetheless crucial the effective as-

sessment of the spinal hrf, necessary also for the ordinary statistical data processing.

Origins of functional contrast

In the BOLD model, the fractional signal change $\Delta S/S$ in $T_2^\star$–weighted images of grey matter tissues can be approximated as a decay linear on TE [19]:

$$\frac{\Delta S}{S} \approx -\mathrm{TE}\Delta\left(\frac{1}{T_2^\star}\right) \tag{1.4}$$

Therefore, if no other phenomena are involved, the expected fractional signal change can be extrapolated to 0 for TE = 0 s

Measures of $\Delta S/S$ vs TE in T_2–weighted images of spinal cord under motor or sensory stimulation gave a good linear fitting, but in the motor task data a strange dependence of the slope of the linear fit on the order of data collection (from longer to shorter TE or vice versa) has been reported [39]. This unexpected characteristic, that doesn't affect data acquired during sensory stimulation, seems to be related to some systematic effect more than to a real physical feature. However, the fittings consistently showed a nonzero intercept, in the order of +2%. Further measures, conducted with shorter TE, seem to confirm the nonzero extrapolation, but suggest also a non linear dependence of $\Delta S/S$ on TE, at TE shorter than about 35 ms [41].

Stroman et al. observed similar functional contrasts with Gradient Echo (GE) EPI and Spin Echo (SE) EPI, in the same experimental conditions [38], while in the brain $T_2^\star$–weighting provides a contrast considerably stronger than T_2–weighting [90]. Furthermore, the contrast is often higher than in brain under similar experimental conditions (Table 1.2). A partial explanation for this feature can be found in the differences of vascular anatomy between brain and spinal cord. As already discussed (see above, page 13), the vessels of spinal cord are optimally arranged for producing a strong and spatially specific BOLD contrast, with little intravascular contribution (that dominates the BOLD effect in brain at 1.5 T) and little static averaging (that is observed in $T_2^\star$–weighted images but not in T_2–weighted ones) [18]. Thus, the signal loss is dominated by diffusion effects and therefore is mainly a T_2–effect, which produces similar contrasts in GE and SE images. A further factor is the anatomy of grey matter, that has a simple shape, without tortuosity and thus allows the best functional homogeneity of imaging

voxel, further enhanced by the good in–plane resolution often reached, giving less partial–averaging effects. However, while these components can account for similar (and increased) T_2 and $T_2^\star$ contrasts, they cannot explain the nonzero extrapolation of $\Delta S/S$ vs TE at TE = 0 s.

This phenomenon can be explained with a non linear trend of $\Delta S/S$ at short TE. Static dephasing and diffusion near vessels contribute non–linearly to relaxation, but static dephasing is likely to have a minor role (see above) and diffusion effects should contribute with a component diverging from linearity only at longer TE and maintaining the zero value at TE = 0 s. Less convincing is the observation of Stroman et al. [39], that constant diffusion weighting vanishes in fractional signal changes expressed as ratio between intensities obtained at the same TE, as the issue is just if variable diffusion weighting, and thus different TEs, can cause a non–linearity sufficient to explain the nonzero intercept of linear extrapolation of T_2– and $T_2^\star$–weighted signals to TE = 0 s.

Stroman et al. hypothesize that the increase of SE contrast and the nonzero intercept of $\Delta S/S$ vs TE are related to a functional increase of the baseline signal, not related to BOLD effect. They observe that, as a consequence of the increased blood flow during activation, the intravascular pressure increases, in particular in arteries. Thus the water flow across the vessels walls can increment and the extravascular water at equilibrium can have a overall increase. As a complemental alternative, an increase in intracellular water can be suggested by the functional decrease of apparent diffusion coefficient observed by Darquié et al. [91], attributed to neuronal swelling during activation. In both these conditions, an enhancement of MRI signal is observed, due to the greater amount of resonant protons [38].

Stroman et al. refer to this phenomenon as Signal Enhancement by Extravascular water Protons (SEEP). In particular, in spinal cord fMRI it is supposed to account for at least half of the functional contrast [39, 41, 47, 92]. In conformity with this hypothesis, a functional increase of signal of 3.3% was observed in T_2–weighted images at TE = 11 ms [41]. Given the long TR (3 s), this enhancement seems to be essentially related to a proton–density change. Probably, the TR utilized is not so long to completely rule out the presence of T_1–weighting or in–flow related enhancement, but similar results were found at TR up to 7 s [39].

The nonzero extrapolation of $\Delta S/S$ vs TE at TE = 0 s in spin echo EPI was observed also in the brain [43, 47, 48, 92], where a nearly zero extrapolation in gradient echo EPI was also observed. Nonetheless, the

extrapolated intercept for SE EPI (about 1%) was minor than in spinal cord. If the baseline increase due to proton–density change occurs in the same compartment where BOLD originates, gradient echo imaging should be as sensitive to it as spin echo imaging. Authors conclude that proton–density change should occur in an extravascular compartment with a $T_2^\star$ shorter than in vessels, where originates the largest fraction of BOLD brain signal at 1.5 T, but with a T_2 at least equal to blood one, as the enhancement effect persists in SE images as long as the echo times sampled. However this explanation implies that the functional variation in T_2–weighted images at 1.5 T reflects mainly the dephasing effect in extravascular compartment, in contrast with the current models [21]. Furthermore, at 1.5 T the brain tissue T_2 is known to be shorter than blood one (either venous and arterial) [93], and not at lest equal, as required by the proton–density change hypothesis. Finally, the nonzero extrapolation was observed in the human brain also at 4 T and at 7 T [94]. In this case, the introduction of diffusion weighting by means of Stejskal-Tanner gradients removed the effect, thus strongly suggesting the intravascular origin of the phenomenon.

In a further formulation, based on the fitting of spinal cord fMRI data with a simple model, allowing for both T_2 and baseline functional variations in two compartments that non exchanges on the time scale of TE, Stroman et al. were able to demonstrate that the observed contrast variation in function of TE, and in particular the nonzero intercept, is related to an increase of the baseline intensity of about $5 \div 6\%$ during spinal cord functional activation [41, 43]. However data are overfitted, and the compartment supposed to be vascular seems to weight for about 45% of the baseline signal at rest, and only 55% of baseline resting signal is referred to the compartment supposed to be tissue.

Neural pathways

The spinal cord is left–right symmetrical. Unlike the brain, in the spinal cord the white matter is external, while the grey matter is inside, with a typical butterfly–shaped section (Fig. 1.1). Spinal cord lies in a vertebral canal, surrounded by CSF. There is also a central canal containing CSF that runs the cord.

The ‘descending tracts’ of the white matter are formed by the axons of motor neurons that extends from the brain and form synapses with dendrites of the neurons which lies in center and anterior (ventral) regions of the spinal cord. The axons of these neurons exit the spinal

cord grouped in the ventral nerve roots. Similarly, the sensory information proceeding from peripheral nerves is relied to the spine by axons grouped in the dorsal nerve roots, which form synapses with neurons within the dorsal areas of the spine; the axons of these latter exit the grey matter and form the 'ascending tracts' of white matter.

In total, 31 pairs of spinal nerves emerge from the spinal cord. Each spinal nerve is formed by a pair of nerve roots (one dorsal and one ventral), that joins at intervertebral foramina; thus the spinal nerves are mixed nerves, as each contains both sensory axons (afferent to the dorsal grey horn) and motor axons (efferent from the ventral grey horn). A pair of spinal nerve and the corresponding four nerve roots define a segment of the spinal cord, that is thus associated with a specific region of the body. Nonetheless impulses reaching the spinal cord from one side eventually pass, at various levels, to tracts running in the opposite side of the spine (crossing over).

Finally, the spinal cord also acts as a minor coordinating center for simple reflexes.

Distribution of neuronal activity with motor and sensory stimulations: signal specificity

The main activation in spinal cord is expected to be ipsilateral with the stimulation (see above, page 23). Nonetheless, also contralateral activation was often observed [36–38, 40, 42, 45, 46], occasionally intense as the ipsilateral one [36, 46]. This is somewhat unexpected, and probably interneurons activity cannot completely account for this phenomenon. At moment, it is not clear whether the contralateral activations are expression of real contralateral activity, or they are simply artifacts. In order to explain these activations, the regulation of motor control, or even the execution of unobserved shadow movements or their conscious inhibition have been involved [36]. Contralateral activation is expected when muscle pain is involved, but a more prominent ipsilateral activation was instead observed with thermal noxious stimulation (2°C) [42].

Very often motor stimulation resulted in an activation of the mediolateral zone of the grey matter, with a slight enhancement of ventral horns. Sometimes also dorsal horns resulted active [36, 37], with intensity comparable or even major than in ventral areas. The presence of unexpected dorsal activation during motor tasks can be partially ascribed to proprioceptive input and – less probably – touch, in particular for larger hand movements. In any case it is likely to reflect also the

insufficient in–plane resolution and the uncorrect registration of images.

Ventral activation in correspondence to thermal stimulus [40, 42, 45] is less surprising, due to interneurons activity. Dermatomes are innervated by fibers from a single nerve, that connects to a single spinal segment, but dermatomes partially overlap; the stimulation of single dermatomes has been shown to roughly map to the corresponding spinal areas [38, 40, 42, 45]. A certain degree of distribution of activation between adjacent spinal cord segments is nonetheless expected, in particular for thermal stimulation, as interneurons can spread the input to several spinal segments [40, 42, 45]. Unfortunately, some differences in the fMRI patterns corresponding to the stimulation of different dermatomes is observed only after the application of a clustering postprocessing routine that facilitates the emergence of such a feature. If no clustering is applied, the stimulation of different hand dermatomes induces fMRI activation patterns that are indistinguishable from each other, and also partially referable to false activations [40].

The activation spreading between segments was observed also during motor tasks [45, 46, 71]. When specific motor tasks are used, designed to require the movement of individual muscle groups innervated by nerves proceeding from different spinal segments, the observed activation spreads on more segments than expected, but the activation in extra segments is less consistent across subjects [71]. This finding suggests a prominent intersubject variability, perhaps in relation of different ability in the accurate execution of the task or also in the muscle innervation. A possible artifactual origin of some unexpected features of the signal can be hypothesized as well. Interestingly, also areas of reduced BOLD response were observed; negative response was more diffuse than positive one and it was similarly clustered [71].

The spreading of activation beyond the expected areas suggest to conduct electromyography studies in conjunction with spine fMRI to exactly assess the activated muscles.

fMRI in the injured spinal cord

Spinal cord fMRI has been recently conducted on subjects suffering from traumatic injuries [42, 45]. Subjects demonstrated persistent activity in the spinal cord below the lesion during a thermal stimulation. The provided thermal stimulation at the inner calf provoked response in the lumbar region of the spinal cord. In healthy control subjects the main activated areas was observed ipsilaterally, in particular in the dorsal

horn, in the intermediate region and in the ventral region (motor area), probably in relation with a withdraw reflex from thermal stimulation [42]. Also a less prominent contralateral activity was observed, mainly in the dorsal and intermediate region. In injured subjects the response was diversified, according to the lesion: subjects with incomplete lesions and capable of feeling, at least partially, the thermal stimulus, had activity patterns similar to that observed in normal subjects. Subject with incomplete lesions, but not able to feel the stimulus, had diminished activity compared with control subjects, in particular in ipsilateral dorsal areas. Subjects with complete spinal cord injuries, while showed consistently less (but not null) ipsilateral dorsal activity, had ventral activity increased both in the ipsilateral and contralateral ventral grey matter [42, 45].

Such increase can be addressed if we accept that the activity in ventral grey matter is normally related to reflex motor activity (withdrawal from cold/noxious sensation) via interneurons; in this case the increased activity would correspond to lack of inhibitory input descending from the brain, due to the complete descending tracts disruption [45]. Following this interpretation, subjects with incomplete lesions, but who cannot feel the stimulus, have less ventral activity due to a descending inhibitory input partially persistent. Nonetheless an objection to this view is that in these subjects the inhibitory input descending from brain should be reduced or absent, due to the interrupted ascending tracts that deprive the brain of the sensory input to which the inhibition is the response. The activation patterns in subjects with incomplete lesions, but who cannot feel the stimulus, should be therefore more similar to those of subjects with complete lesions. In any case, the reduced dorsal activity in subjects that don't feel the stimulus (due to either partial or complete lesions) reflects presumably the disruption of ascending tracts and the consequent lack of functionality (and thus fMRI–observable activity) of neuronal bodies, whose axons has been interrupted, while interneurons that project to adjacent spinal segments or to ventral areas continue to function, and therefore account for the remaining observed activity [45]. Anyway, the simultaneous recording of somatosensory evoked potentials and fMRI response in injured subjects is highly desirable to assess the relationship between the fMRI spinal response and the really perceived stimulation.

The per cent increase of functional signal in activated areas as a function of the temperature of the stimulus was similar in controls and in injured subjects: an increase of $2 \div 3\%$ above the baseline was ob-

served during stimulations between 29°C and 15°C, while below this temperature the increase was larger, $7 \div 8\%$ at 10°C [42, 45]. This suggests that traumatic injuries lower the number of functional neurons, but that the functional neurons responde to stimulation as in non–injured spinal cord.

Even if the amount of fMRI studies of the spinal cord is rapidly increasing, the overall reliability of the functional maps is still debatable. Sometime, functional studies fail, and the functional activation is missed, even in case of no apparent degrading effect of motion [37]; furthermore, the repeatability of results in single subject [44] and in intersubject [46] studies is still not optimal. These factors notably impair the usefulness of spinal cord fMRI in clinical routine, at least until a reasonable assessment of variability sources will be available, either in physiological and pathological subjects. At moment the weight of random factors, like motion and random noise, compared to actual functional variations between trials, can not be evaluated.

Despite the increasing amount of data, the persistent presence of 'unexpected' activation areas, in particular in contralateral zones, makes still debatable the degree of spatial specificity and the origin of the signal. A direct proof that fMRI activation in spinal cord reflects neuronal activity is still lacking. The intrinsic specificity of the SEEP contrast is still unknown, both in brain and in spinal cord, even if it was shown that BOLD and SEEP fMRI maps don't overlap and a better specificity of SEEP–based fMRI was suggested [43, 47].

Spinal cord fMRI in healthy and injured subjects has furnished findings that generally are not surprising, as they were repeatedly observed in animal models. Nevertheless spinal cord fMRI allows us to directly observe those findings on humans, and promises to become a valuable clinical and scientific tool for the non–invasive assessment of spinal cord function.

1.2.3 Methods

In a preliminary study we examined at 1.5 T three healthy subjects on the whole–body scanner (NV/i, General Electric Medical Systems, Milwaukee, WI, USA) of Neuromed institute during a simple, blocked motor task (finger–tapping of the right hand). Five functional slices were acquired, centered on vertebrae and discs from the sixth cervical vertebra to the first thoracic vertebra. In a first stage we investigated the influence of the experimental parameters, such as the kind of coil (volume or

surface), the kind of Echo–Planar sequence (SE or GE, single–shot or multi–shot), the dimension of the Field Of View (FOV), the number of the phase–encoding steps, the presence of spatial saturation pulses.

In order to identify the best TE, we roughly estimated the $T_2^\star$ of the spinal cord tissue, by acquiring with long Repetition Time (TR) fully–relaxed $T_2^\star$–weighted maps and fitting the amplitude of signal in function of TE with a monoexponential decay (GE EPI, TR = 6000 ms, TE = 32 − 80 ms in 5 steps, Flip Angle (FA)= 90 °).

In the functional study two right–handed healthy subjects were examined , using a 3 inches surface coil. Subjects were requested to breath evenly and to keep the neck as still and straight as possible. The subjects' heads were restrained during the experiments by means of a custom head immobilizer.

Gradient–echo (GE, TR/TE = 3000/40 ms, FA = 90 °) planar images were collected during the functional paradigm. The FOV was 10 cm, while images in–plane resolution was 128x64. Seven or five oblique slices were acquired, perpendicular to spinal cord. Slices spanned respectively from the fifth cervical vertebra (C5) to the first thoracic vertebra (T1) (thickness = 9.5 mm, spacing = 0.0 mm) and from C6 to T1 (thickness = 9.0 mm, spacing = 0.0 mm). Thickness and spacing were adjusted so that each slice was centered on a vertebra or on a intervertebral disc. Up to 6 presaturation regions were employed to suppress the signal from outside the FOV and to reduce motion artifacts.

For the seven slices sequence the stimulation design involved 2 conditions alternating every 30 s: rest and fist clenching of the right hand. 3 blocks were acquired, thus implying a total duration of 3 minutes. For the five slices sequence the stimulation design involved 2 conditions alternating every 40 s: fist clenching of the dominant (right) hand and rest. Four functional blocks were acquired. Dummy images were acquired before each fMRI series.

During the postprocessing, images were cropped to select only a subregion containing the entire spinal canal, realigned using rigid body rototranslations and smoothed with a gaussian kernel, Full–Width Half–Maximum (FWHM)= 2.0 mm. Functional analysis [95] was then carried out in the temporal domain on a pixel–by–pixel basis by computing the deconvolution between the time course of each pixel and the task paradigm, to assess the hrf. The signal waveform is supposed to be the convolution of the hrf with the task paradigm; two terms accounting for constant baseline and linear trend were added. Finally, the statistical F map was obtained by solving a least–square problem.

To obtain the time course of the BOLD signal we first averaged voxel by voxel the four task blocks of the five–slices sequence, so obtaining images corresponding to a single temporal series of 80 s, corresponding to an off–on period. Then, voxels which p–value in F maps was less than 0.02, Bonferroni corrected, were averaged. Finally, adjacent time points were averaged two by two, so obtaining an effective temporal resolution of 6 s.

1.2.4 Results

During the preliminary study we found that the quality of the images notably depends on the protocol of acquisition adopted and even on the subject investigated. The application of presaturation pulses contributed to reduce motion and susceptibility artifacts, but these were not completely avoided. In particular, the effect of the CSFflux was very often observed at the boundaries of the spinal cord.

In a second stage the main objective concerned the optimization of post processing, in order to correct the distortions that sometimes impair the quality of functional images, and to adapt the current post–processing algorithms to the peculiarities of the district. We focalized on GE maps, that showed better activations, despite their notably worse quality. By using volume coils the functional analysis of the images was rarely possible. When obtained, the functional maps showed activation spots at the level of the seventh cervical vertebra and adjacent disks, clearly dominated by movement artifacts: the activation was bilateral, with a preferential, unexpected, dorsal localization, almost entirely lying at the boundaries of the cord and in the CSF (Fig. 1.2 A). Also zones of negative signal were identified in adjacent slices (Fig. 1.2 B).

In Fig. 1.3 the same data of Fig. 1.2 A are shown. Unlike in Fig. 1.2, here no correction for geometric distortion is applied, and the functional map is superimposed to the mean EPI. A strong geometric distortion is apparent.

We were able to obtain more reliable activation with the use of the surface coil. To assess the non–artifactual origin of the signal, we estimated the percentage variation of BOLD signal between rest and task condition in activated voxels. The relaxation time experiment gave a value of $T_2^\star = 32 \pm 2$ ms, consequently, we set TE = 40 ms to optimize the Contrast–to–Noise Ratio (CNR). We obtained reliable activation maps in spinal cord, showing strong activation between C7 and T1, as expected. The activation is ipsilateral, even if we observed a slightly

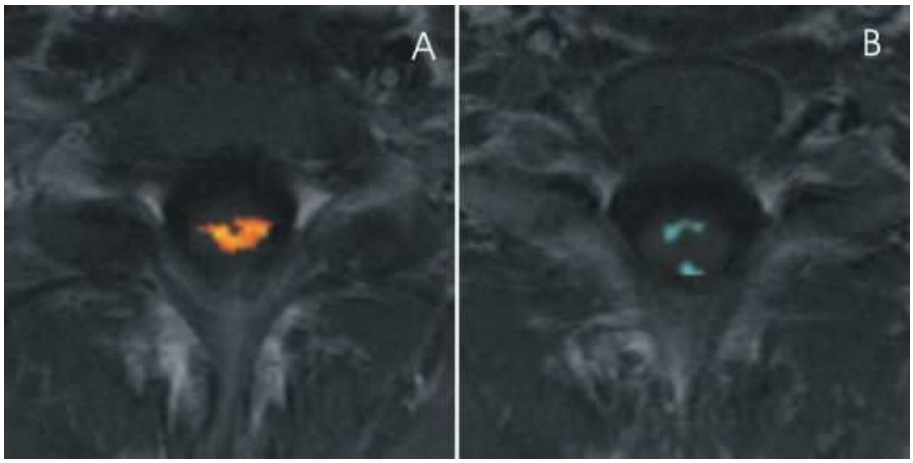

Figure 1.2: A) Artifactual activation detected in GE images (p< 0.01) at level of disc between C7 and T1. B) Regions of negative signal, detected at level of C7 ($p < 0.01$). The maps are superimposed to a T_1 reference. From [96].

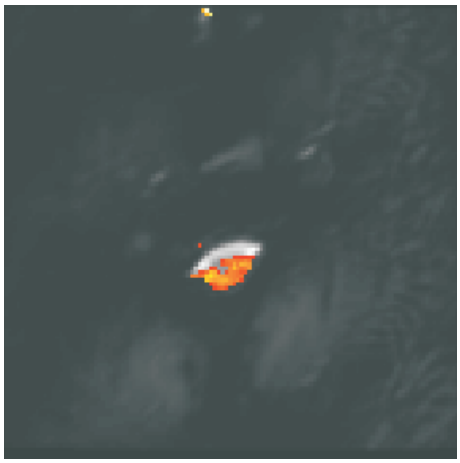

Figure 1.3: The quality of GE images obtained with volume coil is seriously impaired by geometric distortion: the same GE image of Fig. 1.2 A, not corrected for aberration and superimposed to mean EPI. From [96].

enhanced anterior area activation thus suggesting a significant contribution of motor stimulation and a less contribution of sensory stimulation, as expected (Fig. 1.4). The quality of EPI image should be compared to that shown in Fig. 1.3.

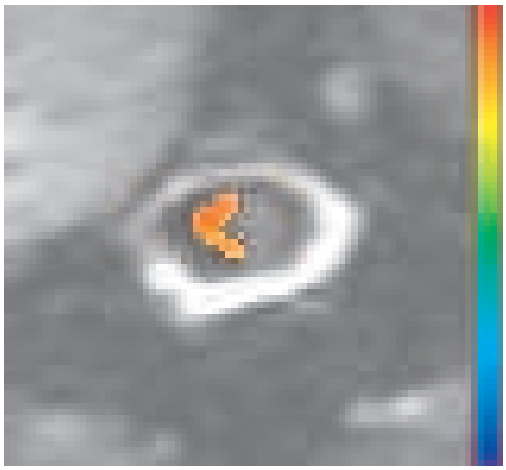

Figure 1.4: A reliable activation was detected in GE images at level of disc between C7 and T1. The map is superimposed to a cropped EPI. The maximum value of colorbar (red) corresponds to F= 8, the minimum one (dark blue) to F= 0. The activation map threshold is F= 6.900 (p= 0.004). From [97].

In Fig. 1.5 is reported the average time course of BOLD signal during a blocked motor stimulation. The average BOLD signal increase over basal level during task condition was about 5.6%. The temporal resolution obtained (6 s) is ameliorative of the best results published so far by Stromal et al. [38], who obtained a temporal resolution of about 10 s. The temporal pattern shows a good agreement with the expected features of a true–BOLD signal, with an initial overshoot (about 6 s after the stimulation start) followed by a lower steady–state level.

Further investigations are required to identify the experimental conditions more suitable to avoid susceptibility and motion artifacts, and in particular to compensate the CSF flux.

In order to test the linearity of the BOLD signal in spinal cord in response to stimulation of variable length, and to verify the possibility to obtain the BOLD time course during these stimulations as convolution of such impulsive response, we are measuring the impulsive hemodynamic response in an event–related experiment.

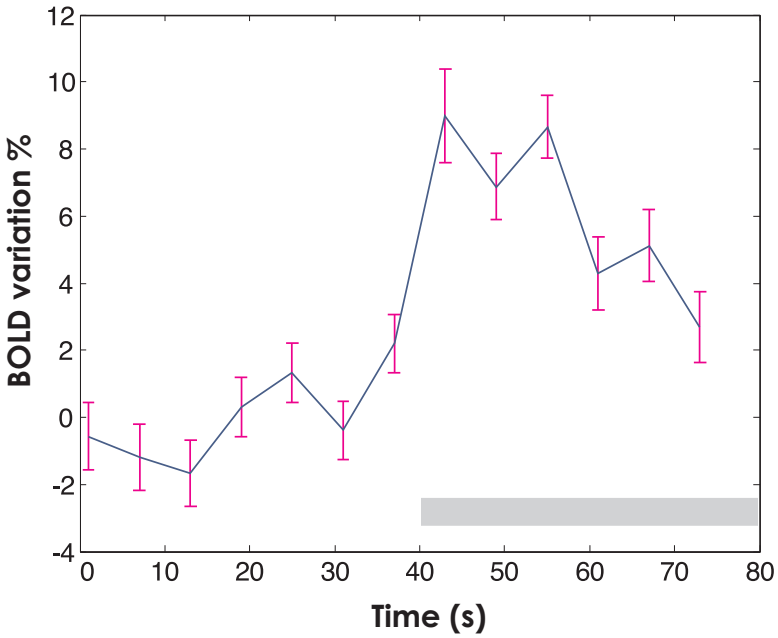

Figure 1.5: The average time course of BOLD signal during a blocked motor stimulation (the gray bar corresponds to the motor task). During the task, the average BOLD signal increase over basal level condition is about 5.6%. Each data point represents a 6 seconds interval. Error bars represent 2 SD of the scaled data. From [97].

CHAPTER 2

Physiology of the Brain Activity

Over the past decade, extraordinarily sensitive new techniques have been developed to allow researchers to see what is happening inside the living, functioning brain. Our knowledge of neuronal physiology and metabolism during activation, nevertheless, still remains at a pioneering stage. In particular, with the advent of the 1990's, MRI techniques became recognized as a revolutionary innovation in the outlining of functional activity.

The most diffused strategy of fMRI relies on the so–called Blood–Oxygenation Level–Dependent (BOLD) contrast [17, 32, 33], in which signal changes in T_2–weighted images are related to local variations in the dHb content of the blood. The BOLD signal is not directly related to electrical neuronal activity, but rather depends on the complex interaction of several metabolic–vascular parameters – such as cerebral CBF, CBV, and CMR_{O_2} – that can not be individually separated and characterized. As a consequence, the absence of a profound knowledge of the metabolic–vascular events of neuronal activation can actually render the interpretation of the signal ambiguous. The possible intervention of modulating factors could also render the same metabolic–vascular dynamics extremely both condition and subject specific [98].

Fortunately, it is also possible to obtain mono–parametric, and thus analytically quantifiable, information about the microvascular flow by means of advanced NMR techniques, which enable a selective study of perfusion without exogenous contrast agents [99]. Perfusion–based methods have been applied to functional imaging (for example, see [100]), and have facilitated the proposal of new models for activation physiology by

virtue of the comparison between BOLD–related and perfusion–related signal changes.

Crucial information also has become feasible with several optical methods, which enable to detect the changes in optical properties of brain tissue associated with functional activity. Most importantly, these techniques permit the tracing of the in vivo dHb dynamics, which can thus be directly related with the time–course of the BOLD signal.

Further useful elements toward the understanding of neuronal activation derive from the in vivo Magnetic Resonance Spectroscopy, which enables the detection of several metabolites that are strictly linked with neuronal activity. Understanding the functional metabolic events is an object of intense debate. The several efforts to link the cellular metabolic phenomena with the macroscopic physiological changes remain to provide definitive conclusions, even on the establishment of the main metabolic substrate for neurons, if glucose or lactate.

2.1 Understanding the vascular network: the Balloon model

In order to quantitatively represent the BOLD signal $S(t)$ as a function of the physiological parameters that create the signal, three independent measures would be necessary, given that:

$$S(t) = f(\mathrm{CBF}(t); \mathrm{CBV}(t); \mathrm{CMR}_{\mathrm{O}_2}(t)) \tag{2.1}$$

Obtaining three independent measures with high temporal resolution is by no means an easy task. During a single session, only two fMRI acquisitions are generally performed (typically BOLD and perfusion). Reasonable physiological models must thus be formulated in order to solve the problem of deducing the lacking parameter and fitting the experimental BOLD signal.

In recent years, the so–called Balloon model, presented by Buxton et al. in 1998 [101], has proved very popular, given that it attempts at providing a simple and exhaustive description of how changes evoked in the blood flow are transformed in the BOLD signal. This model can be considered an evolution of the oxygen limitation model, presented by Buxton and Frank in 1997 [102]. The oxygen limitation model furnished a possible explanation for the large mismatch between the variations of CBF and $\mathrm{CMR}_{\mathrm{O}_2}$ which was originally suggested by PET studies

[4, 5] and later supported by the detection of the positive BOLD signal. Buxton and Frank [101] showed that a large increase of flow is required to support a small increase in oxygen metabolism where it is assumed that:

- all oxygen which leaves capillaries is metabolized
- CBF increases occur through increases of blood velocity alone (absence of capillary recruitment).

The increased blood flow consequently reduces the Oxygen–Extracted Fraction (OEF) due to the decreased capillary transit time. Given the previous assumptions, and given that:

$$\mathrm{CMR}_{\mathrm{O}_2} = \mathrm{OEF} \cdot \mathrm{CBF} \cdot [\mathrm{O}_2]_a \tag{2.2}$$

where $[\mathrm{O}_2]_a$ is the arterial O_2 concentration, the rate of oxygen consumption increases significantly less than blood flow. The oxygen limitation model provides an interpretation of the observed positive BOLD signal in terms of a tight coupling, rather than uncoupling, between blood flow and oxygen metabolism. Nonetheless, it does not explain the fine BOLD time–course (especially the initial dip) [23–28], and it reveals nothing about whether or not blood blow and oxygen metabolism are coupled during *fast dynamic* changes. The Balloon model extends the oxygen limitation model in order to solve the above question.

The essential element of the Balloon model regards the effects of flow (the input of the system) on the blood volume and on the content of dHb, which then reflect on the BOLD signal. Blood volume changes are supposed to occur primarily in the venous compartment, which is also assumed to contain all the dHb. The venous compartment, which is fed by the output of the capillary bed, is considered to expand in the same manner as a balloon in consequence of an increase of the volume flow rate. Another key assumption regards the relationship between blood volume and blood flow, which was mainly suggested by Grubb's law [103]:

$$\mathrm{CBV} = \mathrm{CBF}^{\alpha} \tag{2.3}$$

where $\alpha = 0.4$. In particular, Buxton et al. [101] considered the time–course of volume change during the transition periods as different from the behavior at steady state, as was also confirmed by the studies of Mandeville et al. [104, 105]. The authors showed the Balloon model [101] to successfully reproduce the experimental BOLD data, particularly the

early dip and the subsequent undershoot of the signal. A strong argument in favor of the Balloon model has also been furnished by Friston et al. [106]. These authors demonstrated that the Balloon model, suitably extended to incorporate the dynamics of CBF induction by synaptic activity, is sufficient in reproducing the main non–linearities observed in evoked fMRI responses, such the one resulting from the hemodynamic refractoriness. Nonetheless, different points of view have recently been proposed, as that of Mintun et al. [107]. They constructed a mathematical framework showing that the tissue level of oxygen can be maintained without the need for large increases in CBF, thus suggesting that CBF is regulated by factors other than local requirements in oxygen.

In fact, some assumptions at the basis of the Balloon model still require independent experimental evidence, as the absence of recruitment, which, in turn, implies the limited delivery of oxygen. The description of microvasculature behavior represents one of the most debatable issues in physiology, and it is impossible to exclude the occurrence of recruitment when CBV increases. On the other hand, several recent estimations of CBF and CMR_{O_2} (see Table 2.1) quantitatively disagree with Fox et al's results [4, 5], even if these estimations qualitatively support the concept that CMR_{O_2} changes are smaller than the enhancement in CMR_{Glc} and CBF. Given these evidence, the strong hypothesis of a limitation in the delivery of oxygen seem to be not completely justifiable.

2.2 The measurement of CMR_{O_2}

Of all the parameters which characterize the BOLD signal, CMR_{O_2} is certainly the most problematic, since it is not directly measurable. This parameter, nevertheless, is fundamental in establishing what kind of metabolism occurs during activation. The quantitative value of CMR_{O_2}, which has been obtained in humans only in stationary conditions and with a poor spatial resolution, greatly depends on how the estimation is performed. This explains the large variability of those findings which assess the changes of such parameter during neuronal activation (see Table 2.1).

With regard to the PET strategy, the difficulties associated with these measurements have often led to fervid skepticism about the validity of the data [4, 5, 108, 109, 111–113, 118, 120], which must be accurately deconvolved from multiple measurements [129] with relatively poor SNR. On the other hand, many ambiguities characterize the quan-

Table 2.1: Variations of cerebral metabolic–hemodynamic parameters measured during stimulation in healthy humans.

Ref.	Method	ΔCMR_{Glc}	ΔCBF	ΔCMR_{O_2}
[4]	PET		+29%	+5%
[108]	PET		+7%*	+13%*
[5]	PET	+51%	+50%	+5%
[109]	PET		+40%	+28%
[110]	^{1}H–MRS	+22%		
[111]	PET		+15÷25%	+15÷25%
[112]	PET	+27%	+43%	+0%
[113]	PET	+23.4%† +11.7%‡		
[114]	Kety–Schmidt	+12%	+15%	+0%
[10, 115]	BOLD Perfusion ^{1}H–MRS	+21%		
[116, 117]	PET		+50÷68%	+22÷25%
[118]	BOLD Perfusion		+43%	+6%
[119]	BOLD Hypercapnia		+45%	+16%
[120]	PET			§
[121]	BOLD Perfusion Hypercapnia		+74%	+4%
[122]	BOLD Perfusion Hypercapnia		+44%	+16%
[123]	BOLD Perfusion Hypercapnia		+61%	+2%
[124]	BOLD Perfusion Hypercapnia		+48%¶	+25%¶
[125]	^{13}C–MRS			$< 30\%$
[126]	^{13}C–MRS			$<\sim 60\%$
[127]	BOLD Perfusion Hypercapnia			♢

*: averaged value referred to the entire brain; †: total value; ‡: oxidative value; §: significant increase; ¶: value obtained with the most intense stimulus (with less intense stimuli, what results is that $\Delta CBF : \Delta CMR_{O_2} = 2 : 1$); ♢ $\Delta CBF : \Delta CMR_{O_2} = 3 : 1$. From [128].

titative estimation of CMR_{O_2} also with MRI methods. In fact, the assumptions upon which the procedure is based may well be debatable, as the use of hypercapnia for calibrating the relationship between BOLD and CBF/CMR_{O_2} [119, 121–124, 127]. Hypercapnia could only be used as a control reference upon hypothesizing that:

- there are no metabolic changes involved in the transition to and from hypercapnia;
- hemodynamic responses during neuronal activation and during hypercapnia are similar.

Nevertheless, such hypotheses have not been proven in humans.

NMR spectroscopy can be used to measure the turn-over rate of TriCarboxylic Acid (TCA) cycle following an injection of ^{13}C–labelled glucose, and therefore represent a valid tool in deducing CMR_{O_2} [130]. Nonetheless, by means of such a strategy, Hyder et al. [131] reported a $250 \div 300\%$ increase in CMR_{O_2} in anesthetized rats during single forepaw stimulation, in dramatic contrast with the other data which indicated small CMR_{O_2} increases [4, 5]. These results led to a great deal of criticism about the metabolic pathways utilized for the calculations and about the use of anesthetized conditions. In any case, the recent results obtained in human studies appear more convincing. In particular the results of Chen et al. [125] impose a plausible upper limit of 30% for the fractional changes in CMR_{O_2} induced by a visual stimulation, while the work by Chhina et al. [126] indicates an upper limit of 60%.

A promising alternative approach for CMR_{O_2} measurements in functional studies comes from the use of ^{17}O NMR spectroscopy/imaging. As recently demonstrated, at high fields the $H_2{}^{17}O$ produced by oxidative metabolism can be directly detected in rats during $^{17}O_2$ inhalation [132] and in humans in natural abundance [31]. By means of such approach, Zhu et al. determined [132] the quantitative resting value of CMR_{O_2} in the rat brain, with an optimal spatial and temporal resolution. Further studies are nonetheless needed in order to overcome the great invasiveness of this strategy, which needs an implanted ^{17}O RF coil to monitor the arterial input function related to recirculated $H_2{}^{17}O$.

2.3 The role of CBV

A very central assumption of the Balloon model, and generally of those studies which attempt at providing a quantitative estimation of CMR_{O_2} with MRI, is the validity of Grubb's law Eq. (2.3) for humans.

The only study [133] which reported the measure in humans of the functional metabolic–vascular response by means of three independent fMRI techniques suggests a great deal of caution when applying Grubb's law. The authors performed an experiment where, beside BOLD contrast, two perfusion methods were utilized to single out the changes in CBF and CBV. In comparing the experimentally measured CBV with the value calculated through Grubb's law, the authors found that Eq. (2.3) systematically results in CBV underestimation, which, in turn, may give rise to systematic errors in the estimated CMR_{O_2}. This non–correspondence could arise from the fact that the relationship between CBF and CBV was established by Grubb et al. [103] by means of PET for stationary hypercapnic stimuli in monkeys, whereas it could be argued that the human neuronal activation is notably different from this case. Supporting this idea, Hyder et al. [134] found to be 0.1 in the rat cortex for a wide range of activity, while Wu et al. [135] showed this parameter to be largely region specific.

The critical role of CBV has also been emphasized by Lee et al. [136]. The authors highlighted that separating the contribution of blood volume from the arterial and venous sides of the vascular system is crucial for the quantification of the BOLD signal. In contrast, the NMR or PET methodologies use intravascular contrast agents which are capable of revealing the total CBV alone. The authors utilized a method for the regional measurement of arterial and venous CBV fractions which was suggested by Duong and Kim [137]. This strategy consisted of the use of diffusion–weighted ^{19}F–NMR with the intravascular administration of PerFluoroCarbon (PFC); such an agent possesses two pseudo–diffusion constants, one reflecting more oxygenated blood, and the other reflecting less oxygenated blood. This characteristic allows for the provision of quantitative information about the compartment distribution by means of parameters obtained in the bi–exponential fitting. Lee et al. [136] investigated in rats the modulation of arterial and venous CBV during hypercapnia–induced CBF changes. They found that the arterial CBV changes were about 5 times larger than venous CBV changes, and that the relative CBV changes in venous blood was 50% of the relative CBV changes in the entire blood. Such a finding contrasts from what suggested by Mandeville et al. [104, 105] and by Buxton et al. [101] in the Balloon model, who assumed that changes in venous blood volume dominate the total blood volume increases. The overestimation of CBV changes contributing to the BOLD signal (which corresponds to an underestimation of CMR_{O_2}) can be solved by halving the measured total CBV changes.

The results obtained by Lee et al. [136], nevertheless, cannot directly be applied on humans, because they referred to anesthetized rats, whose blood flow velocities are very different from the case of conscious humans. Even if the study by Lee et al. has the drawback of not providing spatially resolved information, it has however proved of great interest insofar as it focused on the poorly discussed role of CBV in the determination of the BOLD signal. In order to address the issue of region specificity, a recent non–invasive MRI approach has been proposed to estimate the cerebral and arterial blood volumes separately in humans [138], but at the moment it has not been applied to functional studies, nor validated.

As a final consideration, it must be recalled that the increase in blood volume has been here assumed merely to result in a BOLD signal decrease. This assumption is not necessarily true at 1.5 T, where the contribution of intravascular spins is predominant, and renders the effect of CBV more complex. A global model of the phenomenon, more exhaustive from a physiological and physical point of view, continues to be provided.

2.4 Physiological indications from optical methods

Several optical methodologies [139, 140] are currently used to investigate the relationship between blood flow and oxygen metabolism changes. These techniques are able to measure the changes in oxyhemoglobin (HbO_2) and dHb contents, as well as the changes in cerebral blood volume and in the redox status of cytochrome oxidase. Optical methods offer the great advantage of having very high temporal resolution, thus allowing key dynamical information to be obtained. The so–called 'fast response' was reported for the first time by Grinvald and colleagues [6, 141], who utilized in vivo intrinsic optical signals reflected from the exposed visual cat cortex. They revealed an initial increase in dHb after a brief stimulation, around 2.5 s after the task onset, followed by a later and more pronounced decrease about 6 s after the task onset ('slow-response'). This dynamics has been interpreted to correspond to the biphasic behavior of the BOLD signal observed at a high field [23–28]. The existence of an early deoxygenation phase, nonetheless, remains controversial in both the optical imaging and fMRI literature, because this phase is not always found (as an example of this, NMR studies were unable to detect the initial dip in the rat primary sensory cortex even at

very high magnetic fields [142]), and because it can be eventually justified in different ways. It is interesting to note that none of the published optical studies showed a decrease in oxyhemoglobin concomitant with the reported initial increase in dHb content. Instead, a typical finding is that oxyhemoglobin remains constant while the dHb begins to rise. This observation supports the idea that the fast response might result from a complex interplay of changes in CBV and OEF.

On the other hand, a number of critical assumptions must be made in order to interpret quantitatively the optical signal in terms of oxygen metabolism changes. Lindauer et al. [143] did not reveal any dHb increase, and they motivated this result showing how a not correct analysis of the optical path length can lead to an artifactual initial increase. Nonetheless, Jones et al. [144] further spark the controversy, because they found a reproducible initial dHb increase (consistent with earlier works of this group [145]) by using the same rat model and the same sophisticated path length analysis utilized by of Lindauer et al. [143]. The dynamical data of Jones et al. [144] were also used by Mayhew et al. [146] in order to explore the validity of the oxygen limitation model in the original form formulated by Buxton and Frank [101, 102], and in the extended form formulated by Hyder et al. [147], who included a variable oxygen diffusivity proportional to CBF. Mayhew et al. [146] concluded that neither of them gave a particularly good account of the data, and suggested that a more convincing model should consider a non–null tissue oxygen concentration (in the oxygen limitation model, this parameter was implicitly supposed null). According to the authors, the tissue level of oxygen is moderated by changes linked to increased metabolic demand. The presence of O_2 in the tissue could be fundamental in explaining the initial dip variability. In fact Mayhew et al. [146] reported that hyper-oxygenation reduces or eliminates the initial dip, and, on the other hand, Lindauer et al. [143] (who found no initial dip) used a high concentration of inspired O_2. Along the lines stretched by Mayhew et al. [146], Buxton [148] has revised the oxygenation limitation model, by including a buffer of available oxygen and the presence of O_2 diffusion from tissue to capillaries. In this scenario, CBF would be regulated in order to maintain the buffer of oxygen at a constant level.

In order to overcome the ambiguities of earlier optical studies, Vanzetta and Grinvald [149] used an optical technique based on the phosphorescence decay of an oxygen tension–sensitive phosphorescent intravascular probe. A longer phosphorescence life–time implies a decrease in the microvascular pO_2, and implies a decrease in free oxygen concen-

tration. The authors found an initial dip in the average pO_2 of blood, which, again, has been linked to an increased consumption of oxygen not compensated by blood flow. Unfortunately, Lindauer et al. [143] utilized also the technique of Grinvald et al., and they found no initial dip. The authors interpreted the results by Vanzetta and Grinvald, again, as a processing artefact, which derived from the assumption of an oversimplified single well–mixed compartment with a uniform pO_2.

All the above–mentioned optical studies utilized a surface optical mapping of exposed animal brain, and, given their invasiveness, they are not suited for application to humans. In contrast, it has been recently shown that near–infrared light can penetrate biological tissue, thus allowing the non–invasive assessment of brain activity through the intact skull. By means of single–site Near InfraRed Spectroscopy (NIRS), the increase of haemoglobin oxygenation about $5 \div 6$ s after the task onset [6] was confirmed in healthy human subjects during a variety of stimulation paradigms, such as visual [139], motor [150] and cognitive [139] tasks.

CHAPTER 3

Metabolites at Work: *in vivo* Nuclear Magnetic Resonance Spectroscopy

3.1 Quantitative Nuclear Magnetic Resonance Spectroscopy

^{1}H–MRS is currently being investigated as an additional noninvasive tool to monitor the cerebral metabolic profile in the living human brain and to provide more insights into in vivo neurochemistry. This offers the opportunity for studying normal metabolism and development, the aging processes and the pathophysiology in a variety of diseases, as well as to monitor metabolite level changes over time due to disease progression or pharmacological therapies. Nevertheless, quantitation, as well as automation, still remains the fundamental requirement to make MRS an indispensable tool in human neuroscience. Automated pattern recognition analysis of spectra will be the fundamental objective for classification between normal and pathological areas.

As known, proton–containing metabolites and cellular compounds are restricted to a narrow chemical shift range of about 4 ppm. Conventional ^{1}H spectra of human brain tissue, typically obtained from $2-20$ ml Volume Of Interest (VOI) in different locations in cortical gray and white matter, basal ganglia, and cerebellum, contain signals arising from approximately twenty low molecular weight metabolites. The use of shorter TE times in clinical investigations, reducing signal attenuation due to spin–spin relaxation and scalar coupling, makes it possible the detection

of glutamate, γ–AminoButyric Acid (GABA), myo–inositol, and glutamine with minimal distortions due to J–coupling [31, 151–154]. However, only relatively few of them may be unambiguously identified or even quantified at clinical magnetic field strengths, due to the complexity of the spectra and the unpredictable forms of the line shape and baseline. Actually, the strong coupling between proton spins of these metabolites gives rise to complex multiplet spectra, with extensive resonance overlapping, still further complicated by the presence of broad signals from macromolecules and lipids, at least at field strengths acceptable for clinical use. Glutamate and glutamine, for example, split into multiplets in the spectrum due to their chemical structures, overlap to a large extent in their chemical shift range and both show overlapping contributions from GABA. Furthermore the number of scans is necessarily limited in order to keep short acquisition times. Many of these difficulties are overcome at fields higher than those typically used in clinics; indeed, at very high fields the SNR increases and partially overlapping multiplets are better resolved, despite the shorter T_2 of metabolites, due to the fact that the overall signal width of multiplets is dominated by homonuclear J–coupling, which does not depend on B_0. For example, only the singlet component at 3.57 ppm of myo–inositol, which resonates at four chemical shift positions, is detectable at 1.5 T, whereas at 3 T this resonance is resolved into its components at 3.55 ppm and 3.61 ppm [155], and at 7 T its characteristic spectral pattern is completely discernible [152] with a significant improvement of the quantification precision, reproducibility and detection sensitivity of this polyol.

Another factor susceptible to affect the metabolite concentration estimates is ascribable to the different T_1 values between metabolites in the same or different tissues. Actually, in most studies, metabolite peak areas are heavily T_1–weighted because of the short TRs usually imposed by time constraints in clinical studies.

Different procedures are reported in literature in either frequency or time domain [156, 157]. for the spectral quantitative evaluation. In the latest years, time domain processing methods gained great attention because of their several advantages: they require less or any invasive pre–processing, and they are intrinsically free either from spectral distortion due to non ideal Free Induction Decays (FIDs) (e.g. for truncated points), or from baseline problems due to fast decaying signals or imperfect water suppression [158]. On the other hand, in the frequency domain methods, the visual interpretation of the measured signal and the quality assessment of the fitting results are better achieved, and the

frequency–selective analysis is straightforward.

Several 'black-box' time–domain quantification methods are available [157, 159, 160]. They require minimal user interaction and expertise (hence the name of the procedure), but results obtained from the fitting, especially in low SNR spectra, often lack physical meaning. Anyway, such kind of methods produce results with high computational efficiency and without any need for starting values; besides, they can model complex line shapes by the superimposition of Lorenzian curves. All these characteristics allow their utilization in pre–processing steps, such as residual water suppression, and in obtaining starting values for algorithms that exploit prior knowledge.

The possibility of easily incorporating large amount of prior knowledge, typical of the model fitting methods, has a particular interest in the in vivo brain chemistry investigation. Model fitting methods are equally well developed in time–domain and frequency–domain; the a priori knowledge of the spectral pattern of the individual metabolites can be obtained from simulations of model spectra [161] or directly by the effective measurements of model spectra in single solutions [162] NMR investigated in the same experimental conditions as the in vivo spectra. In this latter case, the two main approaches build up the fitting model either from the linear combination in the frequency–domain of the in vitro model spectra [163, 164], or from the superimposition of damped waveforms (generally sinusoids) in the time–domain, where the parameters which determine the spectral line shapes (i.e., amplitudes, linewidth, relative phases, and frequencies) are optimized for the phantom solutions [158, 165]. In both cases the estimates are obtained by minimizing the squared difference between the experimental data and the model.

To date, the software packages more commonly used for quantitation are AMARES [165], a non–linear least square fitting algorithm operating in the time domain as implemented in the MRUI package [166], and LCModel [163], which analyzes an in vivo spectrum as a linear combination of a basis set of model in vitro spectra from individual metabolite solutions, thus exploiting the full spectroscopic information of each metabolite and not isolated resonances.

In this Section we describe our approach to the quantitation of in vivo short–TE spectra of metabolites in the cerebellum of normal subjects by employing LCModel fitting and using relaxation time correction. A set of in vitro spectra of known metabolites was prepared and used as basis functions. We also evaluated the influence of including a macro-

molecular baseline spectrum into the basis set. Furthermore, different line broadenings and noise conditions have been simulated in order to determine the dependence of metabolite estimates on non ideal linewidth and different SNR experimental conditions.

3.1.1 Methods

Sample preparation

A set of individual metabolite samples of L–alanine (Ala), Aspartate (Asp), Choline (Cho), Creatine (Cr), γ–AminoButyric Acid (GABA), D–glucose (Glc), L–glutamine (Gln), L–glutamate (Glu), Myo–inositol (mI), Lactate (Lac), N–acetyl–L–aspartate (NAA), Taurine (Tau) and Glycine (Gly), were dissolved in a pH 7.1 buffer solution of KH_2PO_4 + K_2HPO_4 to a concentration of $50-200$ mM as suggested in the LCModel user's manual [167]. When required, pH value was adjusted using NaOH and HCl and set to pH 7.1 ± 0.1. Chemical shifts were referenced to the methyl signal of 2,2–dimethyl–2–silapentane–5–sulfonate (DSS) at 2 mM concentration. Also Na formate was added, to a concentration of 200 mM. A mixture solution containing Cho, Cr, GABA, Glc, Gln, Glu, mI, Lac, NAA and Tau was then prepared at concentration values similar to average brain values [168]. A small amount of sodium azide (0.10%) was added as germicide to each preparation. Polypropylene bottles (volume 1 l) were used for storage and data acquisition. Samples were positioned with their symmetry axis parallel to the B_0 field.

The individual metabolite data (except Gly) were then used to obtain the basis spectra for the LCModel quantitation [167]. In brief, spectra were automatically corrected for eddy–currents, phased, referenced and scaled by using the singlet of DSS at 0 ppm and of Na formate at 8.44 ppm. Scyllo–inositol (Scyllo) and N–acetyl–L–aspartylglutamate (NAAG) were simulated in the basis by opportunely shifting and scaling the spectra of Gly and NAA, respectively.

Subjects

Seven healthy volunteers (3 women and 4 men, age 28 ± 9 yr, mean$\pm$SD) were recruited for this study. Two or three spectra were acquired on each participant. Informed consent was obtained from all of them.

Data acquisition

All examinations were performed on a 1.5 T whole–body system (NV/i, General Electric Medical Systems, Milwaukee, WI, USA) using a standard birdcage head coil. For the in vivo acquisitions, a Point–RESolved Spectroscopy (PRESS) localization sequence was used with TR/TE = 1500/30 ms, 128 FID averages and 16 unsuppressed water FID averages, sweep width = 2.5 kHz , data size = 2k points. The voxel size was set to $2.0 \times 2.0 \times 1.5$ cm^3 and was centered in the cerebellar area of the subjects.

For the in vitro acquisitions the same sequence was utilized, but with TR = 10000 ms. The long TR was chosen to avoid partial saturation effects. The voxel was $2.0 \times 2.0 \times 2.0$ cm^3 and was put in the center of the bottle. In vitro spectra were acquired all in the same experimental session.

Data simulation

In order to test the reliability of LCModel quantitation in non ideal conditions, spectra with low SNR and broad spectral signals (mimicking poor shimming, subject movements, spectrometer instability) were generated from the original spectra.

The in vivo spectra underwent a preliminary analysis with custom routines written in Matlab [169]. Spectra were eddy–current corrected by means of water–unsuppressed data [170]. When required, manual phasing was performed. Then, the Cr linewidth and the SNR were obtained for each spectrum. Linewidth was measured, as usual, as FWHM, and the SNR was defined as the ratio between Cr amplitude in the frequency spectrum and the standard deviation of the last 100 points of the FID. FWHM and SNR were checked for outliers (defined as values different from the mean value more than 1.5 SD . Spectra had outliers neither for FWHM nor for SNR values.

Two sets of spectra with broadened linewidth were obtained with a gaussian line broadening of 1 and 2 Hz applied to each spectrum. Subsequently, two levels of SNR were simulated for each spectrum of the three sets (the original one and the two line–broadened). Spectra with SNR values equal to a half and a fourth with respect to the original spectrum were obtained by adding white, uncorrelated gaussian noises, with appropriate standard deviation, to real and imaginary parts of FIDs. Therefore, for each spectrum, eight spectra with different levels of noise and line broadening were simulated.

Data analysis

All the spectra were analyzed with LCModel, version 6.1–0 under Linux platform [163] in the spectral window $4.1 - 0.2$ ppm, with prior eddy–current correction by means of water–unsuppressed data [170] and the basis spectra obtained as described above. The water–unsuppressed data were utilized also for scaling the spectral amplitude to the mean water content of grey matter, assumed to be 41.7 M. Analysis was performed both with and without including simulated broad signals from macromolecules and lipids into the basis set.

For the absolute quantification, relaxation times losses were taken into account by considering the T_1 and T_2 values of the main substances under investigation in the cerebellum. The following corrections were applied, where signal intensities were weighted on the basis of TE and TR values employed in the in vivo and in vitro experiments:

$$C_i^{corr} = C_i^{uncorr} \frac{f_i^{T_2}}{f_{H_2O}^{T_2}} \cdot \frac{f_{H_2O}^{T_1}}{f_i^{T_1}} \tag{3.1}$$

where C_i^{corr} and C_i^{uncorr} are the absolute concentrations of metabolite i corrected and uncorrected, respectively, for relaxation effects,

$$f^{T_2} = e^{TE\left(\frac{1}{T_2^{vivo}} - \frac{1}{T_2^{vitro}}\right)} \tag{3.2}$$

is the correction for transverse relaxation in the PRESS sequence, and

$$f^{T_1} = \frac{1 - e^{-\frac{\mathrm{TR}}{T_1^{vivo}}}}{1 - e^{-\frac{\mathrm{TR}}{T_1^{vitro}}}} \tag{3.3}$$

is the correction factor due to longitudinal relaxation to be considered for the same pulse sequence. In practice, as the basis spectra were acquired in fully relaxed conditions, the denominator of Eq. (3.3) was approximated to 1.

Furthermore, the T_2 correction actually concerns a second order effect; as can be seen from Eq. (3.1) and following, the correction is related to the ratio between the correction factors of water and a specific metabolite, and each correction factor is related to the variation of relaxivity between in vitro and in vivo conditions. This is due to the fact that the quantitation method itself automatically accounts for in vitro transversal relaxivity, as it fits the spectrum with in vitro templates.

For this reason, the estimate of T_2 is not critical; therefore cerebellar T_2 values known from literature were employed for the in vivo correction factor [171], while the in vitro T_2 values were roughly estimated from the spectral linewidth of singlets. The concentrations of metabolites, whose in vivo T_2 values are not known from the literature, are not corrected for relaxivity.

The reliability of each single concentration estimate was evaluated by the Cramér–Rao Lower Bounds (CRLB) [172], provided by the program. We did not consider any correction for cerebrospinal fluid contributions to the volume of interest selected for the in vivo spectroscopy investigations, thus assuming that no significant partial volume effects were present.

The absolute concentration estimates are expressed as intersubject averages. As a different number of spectra were acquired for each subject, the evaluations were opportunely weighted, in order to obtain the same weight for each subject in each metabolite quantitation. We set our selection criterion for estimates of acceptable reliability to a value of CRLB $\leq 20\%$.

In most clinical investigations, the changes in metabolite values are often evaluated in terms of a comparison of their relative ratios to creatine with those of normal subjects, although, various pathological states may cause a variability of this metabolite. Moreover, the corrections for relaxation effects are ignored anyway due to the uncertainties in the relaxation times of the various pathologies. Since concentration ratios are less sensitive than absolute concentration to relaxation and partial volume averaging, we also determined metabolite concentrations by assuming creatine as an internal reference.

The reproducibility of metabolite quantitation corresponding to different SNR and line broadening was evaluated in a similar way. As the line broadening affects all spectral peaks, the expected value of T_2 was not modified in the quantitation. Indeed, the fitting lineshape parameters account for the increased transversal relaxation rates from in vitro to in vivo conditions, and a modification of the expected T_2 is only required when metabolites experience differential T_2 variation [163]. Relaxivity was not taken into account in this part of the study. The reliability of each single quantification was evaluated also in this case by the CRLB values. However, due to the specific aim of this part of the study, all successful quantifications were included in the averages, and not only values with CRLB $\leq 20\%$.

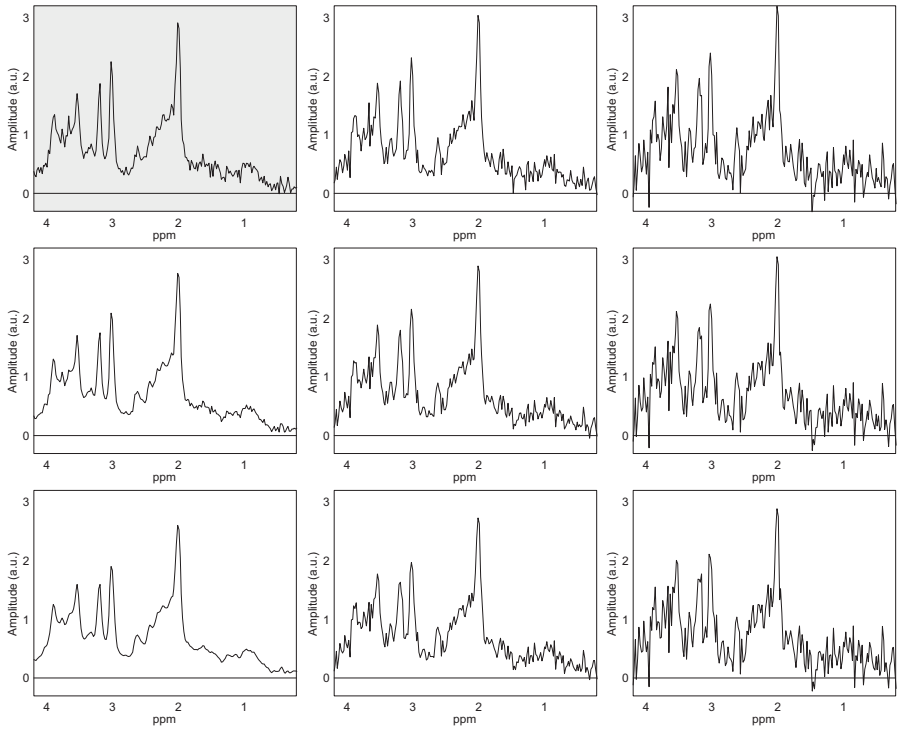

Figure 3.1: A representative in vivo spectrum (grey shadowed) with the various simulations. Each horizontal step corresponds to halving the SNR, each vertical step corresponds to a line broadening of 1 Hz. Vertical scale is expressed in the same arbitrary units for all spectra. The spectral window is the same as the one utilized in the quantitation ($4.1 - 0.2$ ppm). From [173].

3.1.2 Results

A representative spectrum with different line broadening and/or noise level simulations is shown in Fig. 3.1. The original spectrum shows, as expected, large signals overlaps, broad signals ascribable to macromolecules and lipids, and the typical SNR and spectral resolution conditions achievable in a clinical environment. The simulated spectra correspond to progressively deteriorated noise and linewidth conditions.

The estimates of absolute concentrations for the main metabolites in the cerebellum are reported in Table 3.1. As described in Methods, data showing CRLB $> 20\%$ were excluded from this specific part of the study, in order to obtain the most reliable estimates of metabolite concentrations in the cerebellum of healthy subjects. In Fig. 3.2 is reported the number of spectra that, in correspondence of a given level of SNR and

Table 3.1: Absolute concentrations of main cerebral metabolites in the cerebellum.

Metabolite	Concentration without MM		Concentration with MM	
	Absolute (mM)	/Cr	Absolute (mM)	/Cr
a)				
Cho	2.05 ± 0.08	0.24	2.19 ± 0.09	0.24
Cr	8.6 ± 0.3	1	9.1 ± 0.3	1
mI	6.9 ± 0.4	0.80	6.3 ± 0.4	0.69
NAA	8.0 ± 0.2	0.92	8.0 ± 0.3	0.88
b)				
Gln	–	–	6.6 ± 0.4	1.0
Glu	7.4 ± 0.3	1.1	7.0 ± 0.4	1.1
NAA+NAAG	7.5 ± 0.2	1.2	6.9 ± 0.2	1.1
Glx	12.9 ± 0.7	2.0	12.2 ± 0.5	1.9

In section a) the absolute concentrations of the main cerebellar metabolites, corrected for relaxation effects, and their respective ratios to Cr concentration are reported. Section b) reports the absolute concentrations and Cr ratios of other cerebellar metabolites, which have been quantified but not corrected for T_1 and T_2 effects. Values are expressed as mean $\pm$ SEM; the uncertainty on T_1 and T_2 is not taken into account. The concentrations were evaluated without including the broad signals of MacroMolecules (MM), (left side), and in their presence (right side); for details see the Methods. From [173].

line broadening, had the accepted reliability (i.e. CRLB $\leq 20\%$) for the metabolites under examination. As expected, this number decreases with reduced SNR levels. Cho, Cr and NAA+NAAG quantitation does not give any problem, even in the worst experimental conditions. NAA and mI quantification are still reliable with half SNR, while the results become unstable at the lower level of simulated SNR. Quantitation of these two metabolites is also slightly affected by spectral resolution. A further obvious result is that the inclusion of macromolecular baseline modifies the number of 'reliable' quantifications of the sum of L–glutamate and L–glutamine (Glx). When quantitating Glx, lower CRLB values are obtained if MM are included in the basis set, and the quantitation seems to become even more reliable by decreasing SNR and spectral resolution [173]. This feature will be discussed later.

In Fig. 3.3 is reported the relative variation of concentration estimates in correspondence of different spectra quality conditions; in Fig. 3.4 the LCModel fitting of a representative spectrum in the four

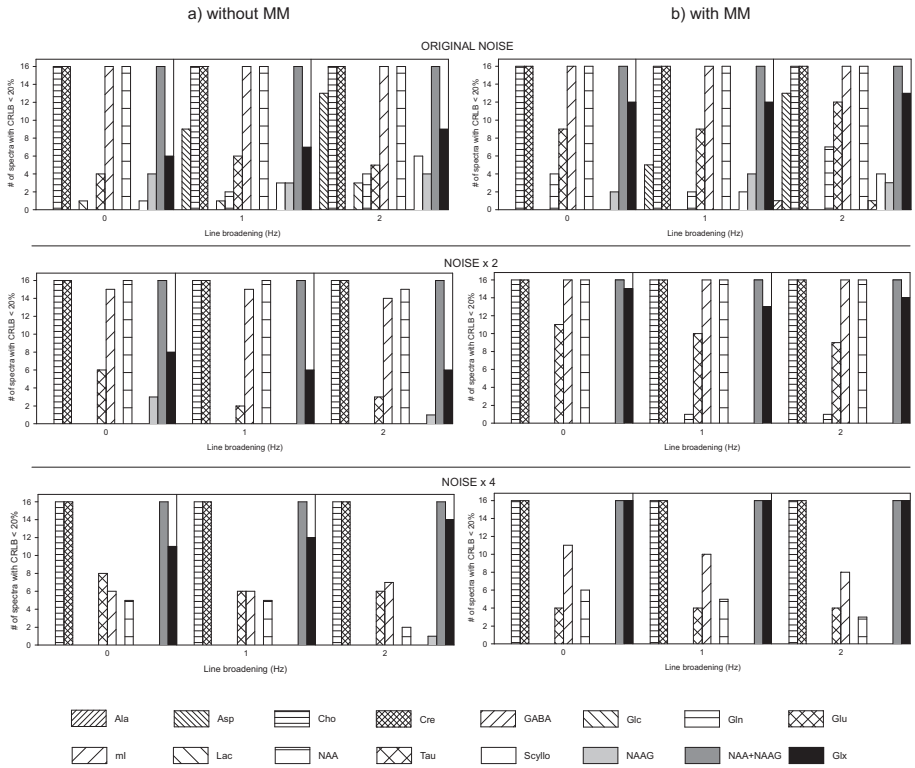

Figure 3.2: a) Number of spectra with CRLB $\leq 20\%$ for each metabolite, without including MM into the basis set. The upper row corresponds to spectra with the original SNR, in the successive rows the results for reduced SNR are reported. In each panel, the left frame shows the results relative to spectra without any line broadening, the middle and right frames report the results for increasing line broadening. b) The same of a), but including MM in the quantitations. From [**?**].

extreme conditions of SNR and line broadening is reported.

The metabolite concentrations found in the cerebellum are compatible with the values known from the literature, relative to brain tissue [168] and, when available, to cerebellum itself. In particular, the values we found for NAA, Cr and Cho are quite similar to those reported by Hennig et al. [174].

The level of glutamine we obtained was high if compared to the values observed in the other brain regions [175, 176]. To our knowledge, no other in vivo evaluation of Gln in the human cerebellum is available from literature, while a value of 4.83 ± 0.32 mM has been measured on ex vivo extracts obtained from various brain regions [176], by proton MRS. Furthermore, our result can be slightly underestimated, due to the lack of correction on T_2 and T_1 effects.

Our results are not directly comparable with those of Kanowski et al. [177], owing to the inherent differences between fully simulated spectra, utilized in [177], and our experimental approach, based on simulated deterioration of in vivo spectra. Indeed, the study of Kanowski et al. investigated the SNR influence in a range of values higher than we did. This can explain why it was therein found that the reduction of SNR mainly increases the uncertainty in quantitation, with few effects on the absolute values of concentrations, while in our study we observed a noticeable variation of the quantitative values in correspondence of reduced SNR, especially for some metabolites.

In this study, the model fitting we used comprised various metabolites whose exact quantitation is almost impossible at 1.5 T. On the other hand, the standard LCModel fitting routine comprises an even larger number of metabolites in the basis set. The aim of this inclusion is essentially to improve the fitting of more prominent signals, by removing, at least partially, some overlapping components. Nonetheless, it is not clear if this approach has positive effects or even makes the quantitation of the main metabolites less reliable. While the inclusion in the model of a larger number of metabolites produces undoubtedly a more accurate overall fitting, the overfitting of the data can easily enlarge the uncertainty of the measurements [178].

The number of data with CRLB $\leq 20\%$ reported in Fig. 3.2 confirms that the inclusion in the fitting of the free parameters related to the 13 simulated MM spectra has great influence on the quantitation of several metabolites. As already observed, Glx concentrations showed increased CRLB values without MM in the basis set (i.e., the number of quantitations with CRLB $\leq 20\%$ is reduced). This unexpected feature, examined

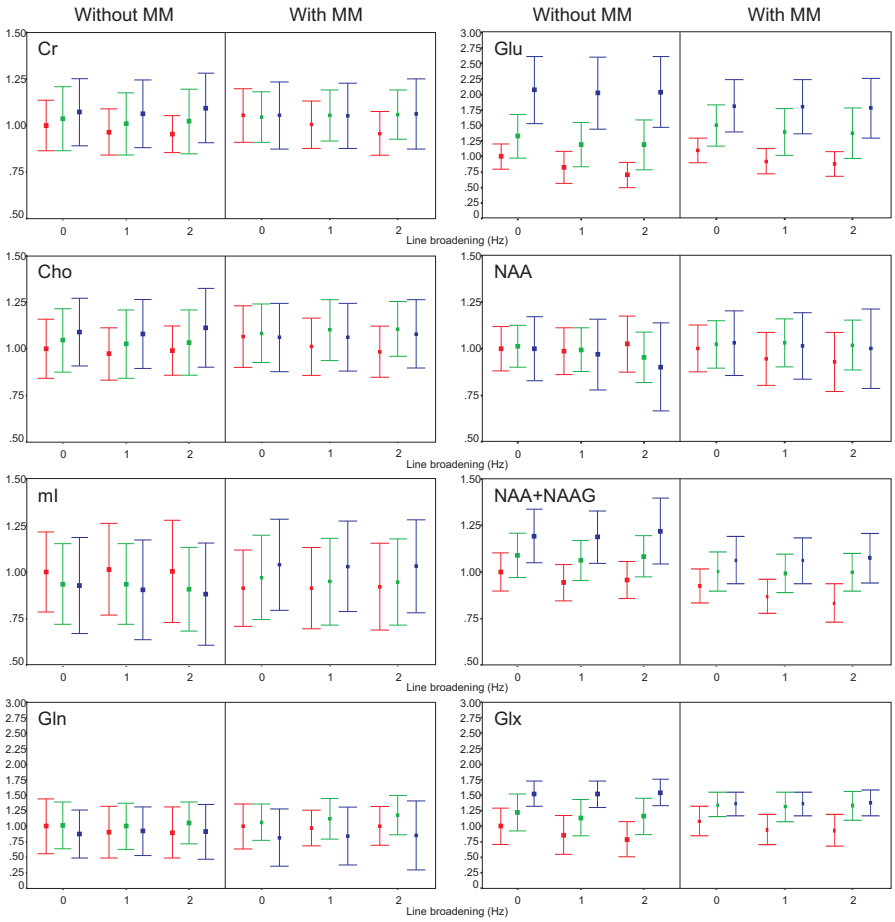

Figure 3.3: Relative variation of concentration estimates of some metabolites in correspondence of different SNR and spectral resolution conditions, referred to the quantitative data obtained from the original spectra without including the MM baseline in the model. In each panel the quantitations without and with MM in the model are reported in the left and in the right frame, respectively. In correspondence of each line broadening, the colors represent different levels of simulated SNR (red: original SNR, green: SNR halved, blue: SNR reduced to 25%. Relaxation effects are in this context not influent and are not taken into account. Values are expressed as mean $\pm$ SD. From [**?**].

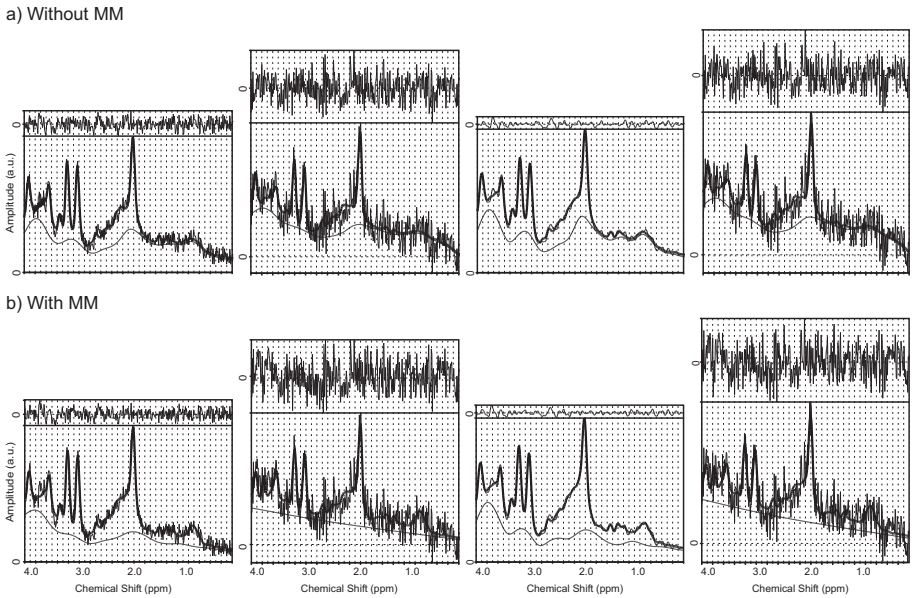

Figure 3.4: A representative in vivo spectrum and overlay of LCModel fitted spectrum, with different simulations. Only extreme cases are reported, i.e. higher/lower SNR and no/maximum line broadening. On top of each spectrum is reported the residue of the quantitation. The same vertical scale, in arbitrary units, is adopted for all spectra. a) Spectra quantified without MM inclusion in the basis. b) Spectra quantified with MM simulation in the basis set. From left to right: original in vivo spectrum, original spectrum with maximum level of noise added, original spectrum with maximum line broadening applied, original spectrum with maximum line broadening applied and maximum noise added. From [**?**].

together with the results of Fig. 3.3 and 3.4, suggests that, in absence of MM from the basis, the degrees of freedom related to Glx quantitation are exploited by the algorithm to fit baseline components instead of the metabolites itself. Actually, such hypothesis is strengthened by the further decrease of CRLBs of Glx when noise and line broadening are increased, and thus the metabolites progressively loss their line shapes.

It has been observed that even a subtle change in the basis composition can affect the concentration estimates of almost all metabolites under consideration. In particular, that holds true if a metabolite, whose spectrum shows large overlapping with other basis spectra, is added or removed from the basis set [178]. The LCModel fitting results, in terms of concentrations and of baseline smoothness, are also strongly influenced by the inclusion of MM in the model [178]. Our results indicate a dependence of these effects on the SNR of the spectra. Indeed, it is apparent from Fig. 3.3 a marked influence of the noise level on some estimated concentrations. This effect is less pronounced if the MM signal is included in the model fitting.

The regularization algorithm that estimates the spectral baseline in LCModel can account for several unwanted signal features, like distortion due to susceptibility or uncorrected eddy–currents [164]. In particular, it has been shown its capability to reproduce the MM broad signal, without any a priori knowledge, when MM measured or simulated components are not included in the fitting [179].

Fig. 3.4 clearly shows that, when the MM are included in the model, the smoothness of the spline baseline is quite modified at low SNR, while this effect is greatly reduced by removing the MM from the model. The residue remains essentially unchanged in both conditions, while the metabolite quantitation remarkably changes, probably due to the change of the baseline estimate. If we assume the concentrations measured on the original spectra as correct, this result, considered with those reported in Fig. 3.3, suggests that, at very low SNR, the quantitation is enhanced by including the MM in the basis set, even though it produces a modification in the estimated baseline.

It is well known from the literature [177] that SNR and spectral resolution influences the SD of quantitative analysis of proton MR spectra, and thus the sensibility of the technique. Our study underlined that different levels of SNR and spectral resolution can affect, in extreme cases, also the mean value of multiple spectra (i.e., the precision of the quantitation). Thus, special attention should be paid when spectra of different quality are examined in the same study.

3.2 An application: cerebellar alterations in migraine

In this Section, our investigation exploiting the time domain model fitting approach in the characterization of a particular form of migraine called 'with aura' is reported.

Migraine is a neurovascular disorder that affects a relevant amount of the general population (12% of the males and 24% of the females) [180]; up to now, there are not available specific biochemical markers for this pathology and the diagnostic methodology routinely used is entirely based on medical history and clinical examination.

According to the International Headache Society classification [181], it is possible to categorize migraine into two main types: Migraine With-Out Aura (MWOA) and Migraine With Aura (MWA). The latter form features a transient focal neurological symptom, generally visual, preceding the attack itself. Although there are conflicting opinions on the familial inheritance of this pathology, there is a rare form of migraine with aura known as familial hemiplegic migraine that is linked to a given gene (CACNA1A), coding for the pore–forming subunit of voltage–gated P/Q Ca^{2+} channels. This gene might also be implied in others forms of MWA, more commonly found, and it is particularly expressed in the cerebellum [182]. Specifically, our aim is to assess by short TE proton spectroscopy possible alterations in the main metabolite concentrations that may be the expression of some metabolic dysfunction characterizing this form of migraine. The etiology is still unknown. Early investigations carried out with ^{31}P spectroscopy have already evidenced defective brain and muscle energy metabolism in patients affected with migraine with different degrees of severity during the interictal period [183].

3.2.1 Methods

Subjects

Prior to investigations, all subjects gave their written informed consent. Eight patients, (6 women and 2 men, age 28±11 yr, mean±SD) suffering from migraine with auras characterized by neurological features, such as somatosensory, motor and/or language impairment, in addition to visual symptoms, and seven healthy volunteers (3 women and 4 men, age 28±9 yr, mean±SD) were included in the study. Two or tree spectra were acquired on each subject.

Phantom preparation

Cr, mI, Glu, Gln, Cho, Tau, Lac, NAA, and GABA were dissolved separately in a buffer solution of KH_2PO_4 + K_2HPO_4 to a concentration of 50 mM. The solution pH was adjusted using NaOH and HCl and set to pH 7.0 ± 0.1. All chemical shifts were referenced to the methyl signal of DSS at low concentration. Each solution was transferred into 100 ml phantoms. Mixture solutions of mI, Cho, Glu, Gln, Lac, NAA, and GABA were prepared in the same way as the individual solutions at two different concentration values, 50 mM and to a concentration 10 times bigger than brain average values [168]. A small amount of sodium azide (0.10%) was added to each preparation as bacteriostatic. The in vitro data were used for the prior knowledge template.

Data acquisition

All measurements were performed with a 1.5 T whole-body system (NV/i, General Electric Medical Systems, Milwaukee, WI, USA) in the MR imaging and spectroscopy unit of IRCSS Neuromed (Pozzilli, IS, Italy). In vivo proton spectra were acquired with a standard birdcage head coil using a single-voxel PRESS sequence (TR/TE = 1500/30 ms). The voxel size was set to $2.0 \times 2.0 \times 1.5$ cm^3 (6 ml) and centered in the cerebellar hemisphere on the dominant side. Typical acquisition parameters were: 128 FID averages and 16 unsuppressed water FID averages, sweep width = 2.5 kHz , data size = 2k points. ^{1}H MR spectra were acquired on patients during their interictal period. In vitro proton spectra were acquired with the same experimental procedures.

Data analysis

All spectra were analyzed with jMRUI software [184]. All data were phase and eddy–current corrected by means of water–unsuppressed data [170]. The residual water was finally removed by the Hankel Lanczos Singular Values Decomposition (HLSVD) filter application. Single metabolite spectra were analyzed by AMARES [165, 185], a non–linear least square fitting algorithm operating in the time domain, included in

jMRUI software. AMARES utilizes the following model function:

$$y_n = \sum_{k=1}^{K} a_k \exp(-d_k(1 - g_k + g_k t_n)t_n) \exp(\imath 2\pi f_k t_n + \imath\phi_k) + e_n \quad (3.4)$$

$$(n = 0, 1, ..., N-1)$$

where the summation is extended to K resonances, a_k represents the peak amplitude and is proportional to the number of protons participating to the resonance of frequency f_k , phase ϕ_k and damping d_k , and g_k allows the choice between pure Lorenzian ($g_k = 0$) or pure Gaussian ($g_k = 1$) line shape, separately for each peak. Finally, t_n is the (discrete) sampling time and e_n is the complex noise, assumed to be white Gaussian.

The spectral modelling from phantom solutions was performed by introducing the prior information on the number of protons participating to each resonance and on J–couplings, phases and the structure of multiplets when these parameters were known, and leaving them unconstrained in the other cases [168]. Damping ratios, frequencies and phase differences were derived from the fits and referred to the most prominent metabolite peak with regards to damping and frequency and to water peak in the case of phase, and then utilized in the analysis of the in vivo spectra.

Metabolite concentrations from the in vivo control spectra were evaluated by considering the total creatine or choline or water as internal reference. The following expression was used:

$$\frac{c_i}{c_{ref}} = \frac{A_i}{A_{ref}} \frac{n_{ref}}{n_i} \quad (3.5)$$

where c is the concentration, A is the peak amplitude and n the number of protons contributing to the resonance peak identified by the subscript i for the metabolite under examination or ref for an internal reference molecule (total Cr, Cho or water).

We didn't apply any correction either for the differential T_2 attenuation and T_1 related partial saturation, or for partial volume effects. Actually, this procedure can lead to concentration ratios between metabolites partially inaccurate, but our approach relies on spectra acquired on the same district and in similar experimental conditions, so these factors equally affect controls and patients and do not influence the statistical distribution of measurement. However, we avoided the evaluation

of absolute metabolite concentrations.

The t–test for unpaired data was used to assess significant differences ($p < 0.05$) of the metabolite ratios between the patients and their age-matched controls. A non–parametric test for unpaired data (Mann–Whitney test) was also applied to assess differences of the metabolite ratios between the two groups.

3.2.2 Results

Fig. 3.5 shows the location of the volume of interest in the cerebellar area with two examples of spectra from a given patient and his age–matched control. The corresponding spectral fittings are also reported.

Table 3.2 contains the results of the metabolite ratios under investigation. Specifically, means, SD, Coefficient of Variation (CV), and p–values of the metabolite ratios relative to NAA, Cr and Cho are shown. As evidenced by the reported data, no changes were detected in the Cr/NAA ratios relative to the two groups of subjects, thus suggesting that Cr and NAA concentrations keep quite stable in this clinical situation. Conversely, Cho/Cr and Cho/NAA ratios in the patients are highly significantly decreased if compared to the corresponding values in the healthy group. The experimental data revealed significance also for mI/Cr and mI/NAA ratios. In particular, they resulted decreased in the patients group. In Fig. 3.6 are depicted the ratios of the metabolites values in the cerebellum obtained from the eight patients suffering from migraine and the normal subjects with the corresponding significance levels.

Our results suggest that subjects suffering from migraine feature alterations in the concentrations of myo–inositol and choline. No statistically significant difference was observed between the two groups when comparing the same metabolites of interest referred to the total amount of unsuppressed water in the volume of interest [186].

Myo–inositol is at the center of a complex metabolite pathway involving among other products inositol phospholipids and inositol phosphates which have well established functions in signal transduction and in Ca^{2+} homeostasis in the CNS and non–neural tissues. Actually, some forms of migraine with aura might be related to some metabolic dysfunction Ca^{2+} channels related [187, 188].

Choline plays an important role in the synthesis of the major constituent of membranes, phosphatidylcholine, and of the neurotransmitter acetylcholine. The choline signal in proton spectra, referenced at

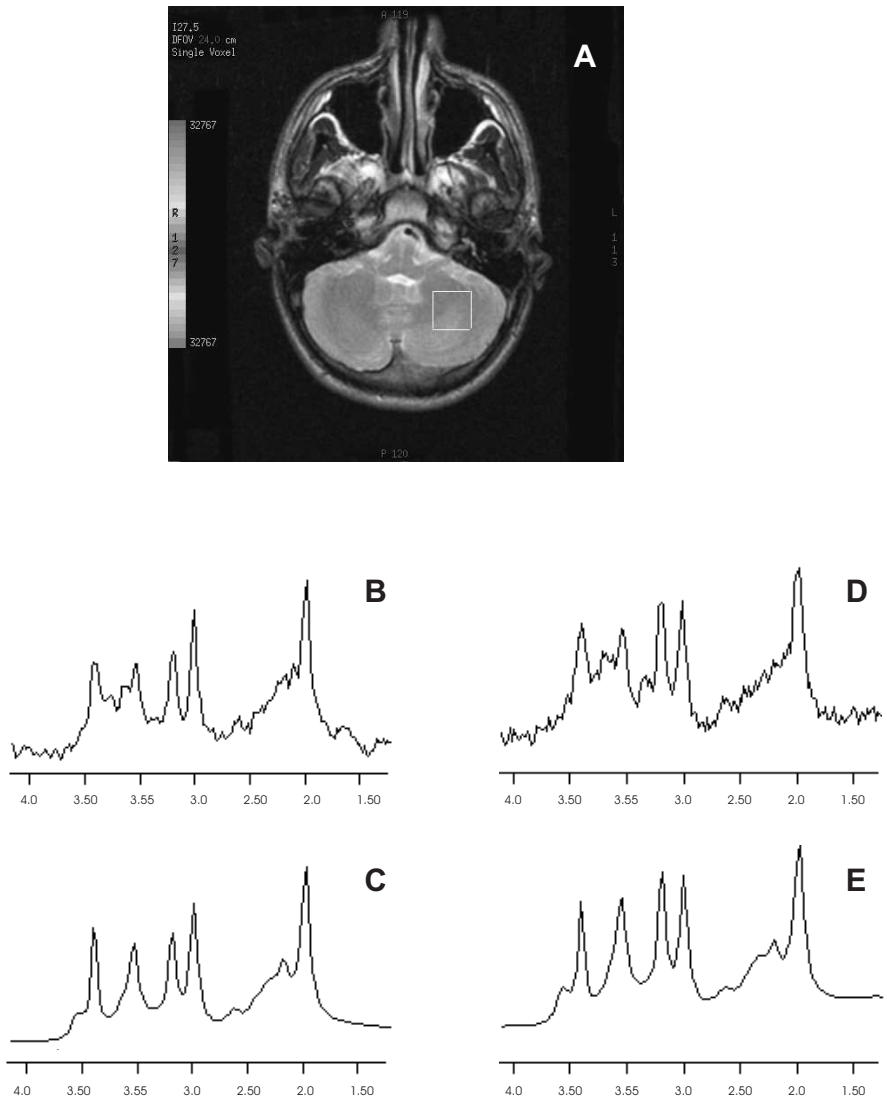

Figure 3.5: Location of the VOI centered in the cerebellar hemisphere on the dominant side. b) Proton spectrum from the volume above relative to a given patient and c) the spectral evaluation of the data reported in b) following the quantification procedure. d) and e) The same as in b) and c) but relative to a normal volunteer investigated in the same experimental conditions. From [186].

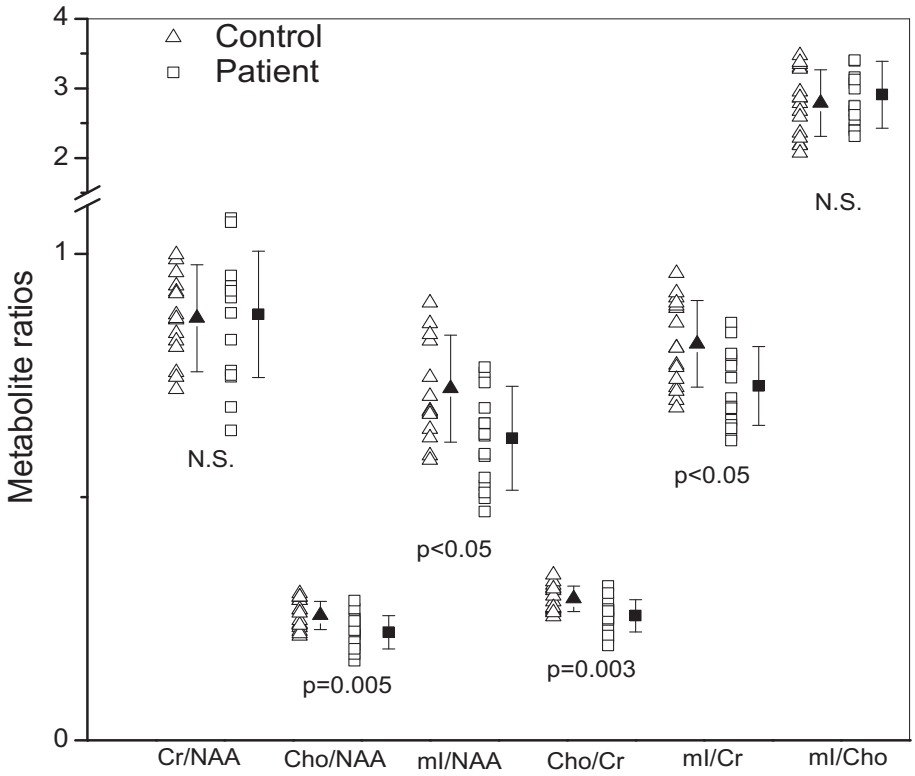

Figure 3.6: Metabolite ratios in the cerebellum obtained from eight patients suffering from migraine and seven normal subjects referred to as controls. Close symbol shows the mean and vertical bars are equal to ±1 SD. Spectra from patients were obtained during their interictal period. N.S.: not statistically significant.. From [186].

Table 3.2: Metabolite ratios relative to NAA, Cr and Cho in controls and patients.

Cr/NAA				Cho/NAA				ml/NAA			
Mean	SD	CV	p	Mean	SD	CV	p	Mean	SD	CV	p
0.868	0.011	13%		0.257	0.029	11%		0.71	0.11	15%	
			0.8				**0.005**				**0.04**
0.876	0.013	15%		0.222	0.034	15%		0.60	0.10	17%	

Cho/Cr				ml/Cr			
Mean	SD	CV	p	Mean	SD	CV	p
0.291	0.026	9%		0.802	0.089	11%	
			0.003				**0.04**
0.256	0.033	13%		0.742	0.081	11%	

ml/Cho			
Mean	SD	CV	p
2.79	0.48	17%	
			0.5
2.91	0.48	16%	

The table reports means, SD, CV and p–values for concentration ratios in controls (first raw of each group, gray background) and patients (second raw, white) Significant values of the differences are in bold characters. From [186].

3.2 ppm, includes, as known, other choline–containing compounds as phosphorylcholine and glycerophosphorylcholine. Besides, at short TEs, this spectral area is further complicated by overlapping contributions from phosphorylethanolamine and taurine. This uncertainty in the metabolites contributing to the signal gives some ambiguity to the biochemical interpretation of the alterations observed in the choline peak. Changes in concentration are generally indicative of alterations in membrane composition. Our results suggest that subjects suffering from migraine feature alterations in the concentrations of myo–inositol and choline peaks. Further studies are in process in order to achieve a better biochemical interpretation of these findings.

The objective of our investigation was to allow, by means of an appropriate quantification procedure, the spectral evaluation of those metabolites visible in spectra acquired at short TE, where the complex spectral pattern and the severe overlap of resonances further complicate the low SNR experimental conditions commonly available in clinical practice. Specifically, an advanced fitting time-domain approach was applied to the evaluation of the metabolic changes in the cerebellum of patients suffering from a particular form of migraine during the interictal period. The quantitative evaluation was based on a library of reference spectra obtained from model metabolite aqueous solutions of known con-

centration built up on purpose and investigated under identical experimental conditions. Our results indicate that patients under examination feature significant changes in some metabolite ratios of clinical interest. Actually, choline and myo–inositol levels, considered normalized both to NAA and Cr, statistically decrease in patients with respect to the corresponding ratios analyzed in normal subjects.

CHAPTER 4

The Brain Metabolism

The metabolic events underlying neuronal activity are still object of intense debate, in spite of the considerable amount of information provided by neuroimaging techniques, like PET and fMRI. This issue was raised up by Fox et al. [4, 5], who observed a focal, stationary uncoupling between CMR_{O_2}, that increases of about 5% during stimulation, CMR_{Glc} (variation under stimulation: $+30 \div 50\%$) and CBF (variation under stimulation: $+30 \div 50\%$). To explain their finding, obtained with PET during prolonged stimulation, the authors suggested the presence of a transient anaerobic glycolysis in neuronal energetic metabolism during functional activation.

Further studies by Pellerin and Magistretti [7] proposed that astrocytes had a pivotal role in neuronal metabolism, by conveying lactate to neurons through an Astrocyte–Neuron Lactate Shuttle. This model hypothesized that the action potential stimulated the anaerobic glycolysis in neighboring astrocytes, producing lactate; this was then conveyed from astrocytes to neurons and converted into pyruvate entering the Krebs cycle to produce the chemical energy needed for neuronal activity.

4.1 Glucose consumption

While several evaluations of cerebral glucose consumption at rest are available, on both humans and animals (e.g. see [189–191]), a relatively low number of studies have been able to assess the variation of this key

parameter under stimulation. Some studies reported a generic decrease of cerebral glucose amount during activation, but did not assess the corresponding variation of CMR_{Glc} [192]; on the other hand, studies on freely moving rats reported a constant level [193] or even an increase of extracellular glucose during stimulation [194]. For a summary of the functional estimations of CMR_{Glc} changes in human subjects, see Table 2.1 at page 37.

The issue of neuronal activation metabolism was raised by the fundamental result obtained with PET strategy by Fox et al. [4, 5], regarding a focal mismatch between the variations of CMR_{O_2} (+5%), CMR_{Glc} ($+30 \div 50\%$) and CBF ($+30 \div 50\%$) during prolonged, stationary neuronal activity (prolonged stimulation). This stationary phenomenon was called uncoupling and, according to the authors, it was the manifestation of a non–aerobic metabolism.

On the opinion of the authors, the exceeding consumption of glucose can follow two pathways:

- it can be utilized in lactic fermentation;
- it can be utilized for glycogen synthesis.

Both these hypotheses imply that the increase of energy due to activation is really low[1], as the maximum increase of ATP production, arising from the aerobic[2] glucose consumption allowed by the small increase of CMR_{O_2} and glycolytic consumption of the remaining glucose, was only +8% above the resting value. This evaluation contrasts with the estimates of energetic requests during activation (for a detailed calculation see Section 4.3 at page 73).

In order to explain this contradiction, the authors hypothesizes that the aerobic enzymatic pool is already saturated in resting state, and so any further energetic requirement must be satisfied anaerobically.

A drawback of these experiments is the very long stimulation utilized: in [4] the tactile stimulation lasts up to 40 min. During this interval, a poor correlation between regions showing variations of CBF and

[1]The first pathway produces a small amount of Adenosine TriPhosphate (ATP), the second even requires energy.

[2]In the literature on brain energetic there is some confusion about the use of the word 'aerobic'. This term is often utilized to indicate that a particular process (anaerobic per se) occurs in presence of oxygen. For instance, Pierre Magistretti in its papers always calls 'aerobic glycolysis' the astrocytic glycolysis. To avoid confusion, in this Thesis the word 'aerobic' is always used to strictly characterize a chemical process that consumes free oxygen.

regions showing variations of CMR_{O_2} is observed, while in resting conditions the basal perfusion is colocalized with the oxygen consumption. As a consequence, the OEF is reduced both in the whole brain and in the activated region (as identified by CBF measures).

In a further study [5] similar results about the uncoupling between ΔCBF and ΔCMR_{O_2} are reported, in an experiment with visual stimulation; furthermore, a large focal increase of CMR_{Glc} is observed (+51%). Unlike the small increase of CMR_{O_2}, the increase of CMR_{Glc} is essentially colocalized with the increase of CBF. The molar ratio for the increase of CMR_{O_2} and CMR_{Glc} is 0.4 : 1 (being 4.1 : 1 the ratio in resting conditions). Consequently, 91% of the functional increase of CMR_{Glc} undergo non–aerobic metabolism.

A subsequent study by Ribeiro et al. [112] essentially confirmed these results, but reported a lower increase of CMR_{Glc}, while Madsen et al. [114] obtained by Kety–Schmidt technique a really low estimation of CMR_{Glc} increase (+12%), and no CMR_{O_2} variation.

The ^{1}H–MRS method can support interesting experimental evidences on the metabolic issue raised up by Fox et al. [4, 5], since it is a valid tool for investigating the metabolic contents of tissues. By means of such approach, a biphasic time course of glucose concentration during about 30 min of photic stimulation was observed by Chen et al. [110], who observed an initial decrease of glucose followed by a slow increase towards the baseline. They utilized a simple Michaelis–Menten kinetics to obtain the variation of CMR_{Glc}, that was estimated to increase by 22% during stimulation. This procedure relied on the assumption of constant transport parameters and constant increase of glucose during stimulation, and only the waning trend was fitted. The latter increase of glucose concentration was related to a decrease of energy requirements due to adaptive phenomena, or to a slight enhancement of the aerobic pathway, leading to equal ATP production with lower glucose consumption. In both cases this datum qualitatively agreed with the observed fall in lactate concentration in the later stages of stimulation (see below for details). By means of ^{1}H–MRS, Frahm et al. confirmed a decrease in cerebral glucose amount due to stimulation increase [10, 115], and evaluated a 21% increase of CMR_{Glc} on the basis of the same kinetic hypothesis adopted by Chen et al. [110]. Finally, Blomqvist et al. [113] utilized two radioactive analogues of glucose to assess during activation the increase of total CMR_{Glc} and the increase of the CMR_{Glc} relevant to an enhancement of the aerobic metabolism. A total increase of CMR_{Glc} about double of the aerobic increase was found, thus suggesting that

aerobic and anaerobic pathways are enhanced by activation in similar degrees.

The variability of the above estimations of glucose consumption is mainly due to the marked experimental complexity and to the ambiguity of the measurements. As already underlined in Section 2.2 at page 36, the PET measures rely on low signals and on several simplifying assumptions, and can be affected by systematic errors due to incomplete trapping of radiotracers [195]. On the other hand, the ^{1}H–MRS studies must evaluate the glucose consumption on the basis of dynamic concentration data, and the results are therefore strictly related to the adopted kinetic model. Both PET and ^{1}H–MRS can evaluate only stationary values of CMR_{Glc}.

4.2 Lactate role

MRS has been widely used in the most recent literature also to measure lactate concentration in the brain of humans and animals during activation (see Table 4.1 for a summary of the data obtained in humans).

Stationary increases of lactate concentration are often related to pathologies which enhance the anaerobic pathway, due to a paroxysmal increase in energetic requests as occurs for example in epileptic seizures [200], or due to an inadequate oxygen delivery compared with the tissue demand as occurs in ischemia, hypoxia, tumoral tissues.

On the other hand, a transient lactate increase during neuronal activation has been reported by several studies. The first observation of this kind was reported in 1991 by Prichard et al. [8]. The authors detected a maximum variation of about +60% in the primary visual cortex of the human brain during the first minutes of stimulation, which lasted for 48 minutes. The intersubject average value of the maximum increase in lactate concentration during a 12 min stimulation was 54% of the resting value (the data spanned in the range of about $+30 \div 90\%$). In several subjects the maximum increase of lactate was observed in the first minutes of stimulation, followed by a slow decline toward the baseline during and after the stimulation. The temporal resolution obtained was $6 \div 8$ min.

Similar observations were done by Sappey–Marinier et al. [9], who measured the lactate concentration in the primary and associative visual cortex during two visual stimulations of 38.4 and 12.8 minutes, spaced by a 12.8 minutes dark period. The maximum lactate increase coming

Table 4.1: ^{1}H–MRS measurements of lactate variations in activated regions of human brain.

Ref.	Stimulation	Stimulation length	Subjects	Lactate variation
[8]	photic	12 min	5	+54%
[8]	photic	48 min	1	$\simeq$ +60%
[9]	photic	38.4 min	6	+150%
[192]	photic	6.5 min (?)	48	$*$
[196] §	photic	3 min	7	+92%
[196] §	photic	6 min	4	+76%
[197] §	auditory	$30 \div 60$ min	6	†
[198]	motor task	6.5 min	7	‡
[10, 115]	photic	$4 \div 6$ min	25	+68%
[199] §	photic	40 s	1	+24%
[11]	photic	1 s	5	$\simeq -50\%$

Lactate variations are expressed as percentage of the rest level. The greatest absolute value reached during or after the stimulation is reported. $*$: no significant variation observed. †: increase ‡: considerable increase. Also preliminary results published only in abstract form are reported; they are marked with § near the reference. From [128].

from the intersubject study was +150% of the basal level, reached during the first minutes of the first stimulation (the temporal resolution was 6.4 min). The authors obtained also PhosphoCreatine (PCr) and Inorganic Phosphate (P_i) measurements by means of ^{31}P MRS and in slightly different experimental conditions; during the first 12.8 min of stimulation was observed a significant decrease of the $[PCr]/[P_i]$ ratio; also the evoked potential amplitude, measured in the same conditions, decreased significantly.

The increase of lactate observed by Prichard et al. [8] and by Sappey–Marinier et al. [9] could be related to a transient phase of physiological anaerobic metabolism [4, 5]. However, as remarked by Prichard et al. [8], the estimate of absolute lactate increase could account only for few minutes of lactate production at the rate computable from Fox's studies [4, 5]. As a consequence, these data suggested that the mismatch between oxygen and glucose consumption must be restricted to the early minutes of stimulation. This calculation, nevertheless, relies on the quite arbitrary hypothesis of a constant lactate transport. The latter decrease of lactate has been interpreted by Sappey–Marinier et al. [9] as an indication of a subsequent phase of adaptive response, which could be also the cause of the decline observed in the evoked potential. This hypothesis implied that the decrease of lactate was not related with a dynamic recoupling of hemodynamic parameters due to a switch towards the aerobic pathway.

The high variability of lactate observed in the intersubject studies [8, 9, 198] was underlined by Merboldt et al. [192], who did not detect any significant lactate dynamics in their work, which was conducted on 48 subjects, in correspondence of a wide range of experimental parameters. The observed lactate levels at rest were markedly variable (in the range of $< 0.3 \div 1$ mM), while the concentration during the prolonged photic stimulation showed multiples patterns in different subjects. The great variability of the adopted experimental conditions makes nonetheless very puzzling the interpretation of this finding, that disagrees with several literature data, including some important following works of the same group [10, 115].

The results described above are not unanimous, probably due to low lactate concentrations and to different experimental conditions. A further confusing effect is the possible lactate binding with proteins, that strongly influence the spectroscopic visibility of lactate [201]. Anyway, the main critical point of these studies is the use of prolonged stimulations, that can easily produce complex and partially uncharacterized

phenomena of habituation or adaptive response. Prolonged photic stimulations, usually employed in lactate experiment, are indeed reported to be stressful for subjects, thus suggesting to reduce the length of the experimental sessions [9]. On the other hand it is known that stressing stimulation can generate anomalous lactate response, and a marked increase in extracellular lactate has been clearly observed with microdialysis on awake, freely moving rats subjected to forms of mild stress (handling, restraint, tail pinch) [202, 203]. Finally, prolonged stimulations can induce stationary metabolic conditions, where the dynamic response to transients is possibly missed.

A second question is the poor temporal resolution normally achieved; the phenomena of neuronal activation span on temporal scales of several orders, which in part are still not exactly known: from milliseconds of electric activity at neuronal level, to several seconds of large scale vascular events, like variations of CBF and CBV. The metabolic events probably lie in the middle of this interval, since they are aroused by the energetic cost of action potential transmission, and, in turn, induce the vascular response. Measuring the metabolite concentrations with the same temporal resolution of the hemodynamic events, together with the use of those stimulations that likely produce a 'physiological' activity, are therefore advisable.

Unfortunately the MRS suffers from a temporal resolution, which is greatly limited by the poor metabolites SNR, that requires the acquisition of tenths or hundreds of spectra to be averaged. A first partial solution to such a problem was given by Frahm et al. [10, 115], who utilized a sliding window averaging to reach a nominal temporal resolution[3] of 30 s. The necessary number of spectra was obtained by repeating 5 times the paradigm of visual stimulation. In any case, also this approach requires the use of long stimulations (4 and 6 minutes stimulations were utilized, with no appreciable differences in lactate accumulation), and thus it can not obviate the relevant problems. The observed increase of lactate, +68% of the resting value, was restricted to the first half of the stimulation, while during the second half the lactate concentration decreased to basal level. The authors measured during the same stimulation protocol also the time courses of glucose concentration and Cerebral Blood Oxygenation (CBO). They observed a glucose consumption during the whole stimulation, and two peaks of

[3]Note that, in fact, the moving average approach between subsequent group of spectra here utilized necessarily induces a smoothing in the measured time–course, so decreasing the sensitivity to fast changes, as in every case of low–pass filtering.

blood iper– and ipo–oxygenation, respectively at the beginning and after the end of the stimulation. In the opinion of the authors, the augment of glucose consumption can account for the increase of lactate concentration by hypothesizing 2 min of anaerobic metabolism, in good agreement with the calculation of Prichard et al. [8] (variations of transport kinetics are ignored also in this estimate); this observation is corroborated by the measured peak of iper–oxygenation, that lasted just about 2 min. Upon this set of experimental observations, Frahm et al. hypothesized a dynamic change in brain metabolism, from anaerobic to aerobic, during the stimulation: the activation onset could be accompanied by a transient phase of glycolysis, coupled with the fast CBF changes but not with the slower beginning of the oxidative phosphorylation. During the subsequent steady–state phase, hemodynamic and metabolic parameters could recouple, and the final undershoot of CBO should compensate the initial anaerobic phase. In this framework, the metabolism as a whole is entirely aerobic, and the decreases of CBO and lactate during the latter phases of stimulations are not related to a habituation effect, but rather depend on a physiological metabolic switch.

This phenomenon was identified with a delay between the astrocytic glycolysis and the subsequent neuronal aerobic oxidization of the produced lactate, according to the ANLS model proposed by Magistretti and Pellerin [7]. This metabolic model provides that astrocytes have a central role in brain energetic, as neuronal released glutamate would stimulate astrocytic glycolysis, which in turn produce lactate. This metabolite would be exported to neurons, that would utilize it as their main energetic substrate (See Section 4.4 at page 77 for details). It must be underlined that the interpretation of Frahm's data [10, 115] in the context of the ANLS model relies on the hypothesis that the oxidative phosphorylation and the lactate diffusion to neurons, that are events at molecular or cellular level, are slower than regional vascular events. Nonetheless, during neuronal activation, the molecular events are required to quickly produce energy, whereas the interpretation suggested by Frahm et al. implies that no energy production occurs during the $2 \div 3$ minutes between the onset of the stimulus and the beginning of aerobic metabolism. Furthermore, the switch towards aerobic metabolism observed during the steady–state phase occurs very early during the stimulation, in contrast with the persistent anaerobic metabolism observed by Fox et al. during prolonged stimulation [4, 5].

In order to further gain in temporal resolution and avoid the ambiguities related to prolonged stimulation, we used a time–locked modality

in an event–related experimental design [11], that involved a MRS intersubject study of lactate concentration in correspondence of a visual impulsive stimulation. We observed a marked decrease of lactate below the resting value within 5 s from the end of the stimulation, followed by a return to the baseline at about 12 s after the end of the stimulation. Such a result was interpreted as an indication that the neuronal metabolism is aerobic from the onset of neuronal activity. For further details, see Section 4.5 at page 78.

Furthermore, we proposed an explanation [12] for the increase of lactate [8, 9, 198] and the uncoupling between CMR_{O_2} and CMR_{Glc} [4, 5, 112] previously observed during prolonged stimulation, without involving neither the switch of neuronal metabolism towards anaerobiosis [4, 5], neither the nutritional coupling between neurons and glia (see Section 4.6 at page 84 for further details).

Anyway, further experimental investigations, together with a quantitative analysis of the involved kinetics, are required to effectively link the early depletion of lactate [11] and the lactate increase observed during prolonged stimulations [8, 9, 198].

4.3 The cost of brain activity

In order to calculate the energy needs of signaling in the brain, anatomic and physiologic data can be utilized: in particular they can be used to analyze the expenditure of excitatory signaling in the grey matter. Attwell and Laughlin [204] recently reviewed the issue. They analyzed the transmitter release triggered by a single action potential passing through a typical neuron of rodent brain. As a simplification, all cells were treated as glutamatergic, because excitatory neurons outnumber inhibitory cells by a factor of $9:1$, and 90% of synapses release glutamate. The energy needs of all the stages of glutamatergic signaling were estimated by considering different parameters, such as the number of vesicles of glutamate released per action potential, the number of postsynaptic receptors activated per vesicle released, the ion fluxes and metabolic consequences of activating a single receptor, and the energy costs of taking up and recycling glutamate.

The following step was to compare the energy expended on the effects of glutamate to that needed for the action potential that triggers glutamate release and for maintenance of the resting potential between action potentials. By basing their calculations on the passage of signals

through a single neuron, Attwell and Laughlin [204] obtained a clear picture of the relative amounts of energy used by different cellular processes and the relation between energy usage and action potential frequency. Finally, they multiplied these results by the number of action potentials occurring in the neurons of a given brain volume to obtain the absolute energy expenditure.

At rest, a cell with a membrane permeable to Na^+ and K^+ reaches an equilibrium with no net charge flux across the membrane, in which Na^+ entry and K^+ exit through the membrane conductances exactly balanced by the pumped fluxes in the opposite directions. Action potential and synaptic signaling involve an influx of Na^+, and an equal efflux of K^+ to bring the membrane potential essentially back to its resting value. The estimates of the ATP consumption by action potential and synaptic signaling depend on how much extra ATP (above the resting consumption) is used to reverse these ion movements. To calculate this it is necessary to take into account the fact that the changes in ion concentrations and pump rate, which are evoked by signaling activity, alter slightly the membrane potential and the resting ion fluxes through the membrane conductances.

Signaling with one vesicle of glutamate, containing approximately 4000 molecules of glutamate, requires energy to trigger the release of the vesicle, to power the postsynaptic events activated by the glutamate, and to recycle the vesicle and its glutamate. The major energy expenditure is on reversing the ion movements evoked by glutamate's actions on postsynaptic N–Methyl–D–Aspartate (NMDA) and non–NMDA ionotropic receptors, which together require hydrolysis of approximately 1.37×10^5 ATP molecules/vesicle. The energy usage resulting from activation of G protein–coupled receptors, including the generation of Ca^{2+} transients in spines, is more difficult to predict, but may be approximately estimated in3000 ATP molecules/vescicle. This metabotropic receptor consumption is low because of the small volume of a spine and because the intracellular concentrations of second messengers are low. In total, the postsynaptic actions of a vesicle of glutamate are powered by the hydrolysis of 1.4×10^5 ATP molecules. Furthermore, the recycling of 1 vesicle of glutamate uses 11000 ATP molecules, used to take glutamate up (mainly into astrocytes), convert it to glutamine, export it to neurons, and package it into vesicles. Finally, pumping out the Ca^{2+} that triggers the release of the vesicle is estimated to consume 12000 ATP molecules, and the mechanisms of vesicle exocytosis and endocytosis may each consume other 400 ATPs, however this mechanism is still in-

completely understood.

Summing the above mentioned estimates, the energy expended per vesicle of glutamate released is 1.64×10^5 ATP molecules. Postsynaptic ion fluxes dominate the distribution of energy use (84%). Presynaptic calcium influx and transmitter recycling are of secondary importance (7% each); the metabotropic responses of spines and vesicle recycling, are negligible (2% and 0.5%, respectively). This distribution reflects the fact that chemical synapses work as an amplifier: approximately 100 ions enter the postsynaptic terminal for each molecule of glutamate released. The energetic costs of recycling glutamate and vesicles are low because, despite the complexity of the mechanisms, the number of molecules involved is small.

Vesicle release is triggered by action potentials, which are produced by ion movements that must be reversed. From the membrane area and capacitance that needs to be polarized, 1.15×10^9 Na^+ ions are required to propagate a single action potential through a typical neuron [204]. Pumping out these ions requires hydrolysis of 3.84×10^8 ATP molecules. Of this amount, 82% supports action potential propagation to output synapses along axon collaterals, 14% supports depolarization of the dendrites, and 4% supports depolarization of the soma.

Averaged over rodent neocortex, each action potential can evoke glutamate release from approximately 8000 boutons. However, boutons do not always release a vesicle, and the release probability is dependent on action potential frequency. At the climbing fiber synapse, the release probability (at 23°C) is 0.9 at low stimulus rates, but decreases to 0.15 at 4 Hz (the mean action potential frequency used below). At about 37°C in cortical neurons, the average release probability is 0.5 to 0.64 at low stimulation frequencies, and may be more than halved for frequencies greater than 5 Hz. As an estimate for an action potential frequency of 4 Hz at 37°C, therefore, it can be assumed a release probability of 0.25, so that each action potential will release 2000 vesicles from 8000 boutons. From these results, the energy expended on releasing one vesicle of glutamate is 1.64×10^5 ATP molecules, so these 2000 vesicles have an energetic cost of 3.28×10^8 ATP molecules, slightly less than the cost of the action potential that releases them (3.84×10^8 ATP). Thus, when a neuron fires an action potential, the total ATP consumption is 7.1×10^8 ATP/neuron/spike, most of which is expended on ion fluxes in axons and at synapses.

From their studies on membrane potentials and input resistances, Attwell and Laughlin [204] calculated that 3.42×10^8 and 1.02×10^8 ATPs/s

are needed to maintain the resting potential of a typical neuron and glial cell. In cortical grey matter, there are approximately the same number of glia as neurons, resulting in a total consumption of 4.44×10^8 ATPs/s per neuron (and associated glial cell).

The mean firing rates of neurons in intact animals, engaged in natural patterns of behavior, are only approximately known. For freely moving rats, the rates of cortical units range from 0.15 to 16 Hz. The means, for neuronal populations in different areas and studies, range from 1.5 to 4 Hz. Since these data were obtained in laboratories where sensory stimuli were controlled and limited, they took the higher value of mean rate, 4 Hz. Thus, for rodents, the ATP usage on signaling by action potentials and glutamate will be $4(3.84 \times 10^8 + 3.28 \times 10^8) = 2.85 \times 10^9$ ATPs/neuron/s. Adding the consumption on the resting potential gives a total rate of 3.29×10^9 ATPs/neuron/s at 4 Hz mean action potential frequency.

Therefore, 3.42×10^8 ATPs/s are used to maintain the resting potential of a neuron, 1.02×10^8 ATPs/s are used to maintain the resting potential of associated glial cells, 15.4×10^8 ATPs/s are used for action potential signaling at 4 Hz in the neuron, and 13.0×10^8 ATPs/s are used for glutamatergic signaling from that neuron. This estimate of energy usage is broadly confirmed by the distribution of mitochondria in the brain.

These calculations were made by analyzing data coming from rodent brain, and an adjustment for comparison with human brain data is required. Few data are available to calculate the postsynaptic ion fluxes activated by a glutamatergic vesicle in humans. Action potential–related energy usage may be increased by a greater axon and dendrite length for at least some neurons in the larger brain, and by the higher mean firing frequency (perhaps 9 Hz rather than 4 Hz) in primates; anyway it would be decreased by the lower vesicle release probability at the higher frequency. More major changes in the predicted energy budget of the brain will result from the 3– to 10–fold lower density of neurons in humans, with an unchanged density of synapses, implying a 3– to 10–fold higher number of synapses/neuron. A 10–fold change will increase the fraction of ATP usage devoted to reversing the postsynaptic effects of glutamate, but will reduce by 54% the specific prediction for the percentage of energy expended on other phenomena, like axonal action potentials, presynaptic Ca^{2+} entry, accumulating glutamate into vesicles, and recycling vesicles. The close spacing of terminals along axons (5 μm, implying a diffusion time of only 25 ms) will make terminal

and axonal mitochondria functionally indistinguishable.

A first important attempt in drawing a mathematical model for neuronal activation, including the present knowledge on relevant physiologic and metabolic events, was recently proposed [205]. This model utilizes the neuronal sodium inflow as the input of the system, and it estimates the time course of the main observable parameters (BOLD signal, PCr, ATP, glucose, lactate). The model includes electrophysiological, metabolic, and hemodynamic aspects of the local response of brain tissue during activation. By adopting this model, the simulations of an activation lasting 6 minutes were shown to quantitatively agree with the experimental data of Frahm et al. [10, 115] on the maximum absolute variation of glucose and lactate amount, even if the simulated time courses were inaccurate. In fact, these simulated maximum values were reached only after the end of the stimulation, unless an ad hoc delay in mitochondrial respiration was introduced. Also a decrease of $[PCr]/[P_i]$ ratio was predicted, in qualitative agreement with the measures of Sappey–Marinier et al. [9]. At this stage of the studies, the model has relied on the transport between only two compartments (capillary and neuron), and has not accounted neither for a possible compartmentalization of metabolism in neurons and astrocytes, nor for diffusion phenomena in extracellular space and in remote tissue regions. Although the effectiveness of this model remains to be proven, it is a fascinating approach that could develop in a more complex and comprehensive model of brain metabolism and physiology.

4.4 A Model for the brain energetic: the lactate shuttle

The ANLS model is mainly based on the observation that astrocyte end–feet surround intraparenchymal microvessels, and then represent the first cellular barrier for glucose entering the brain; furthermore, some neurotransmitters were shown to stimulate the glycogenolysis in astrocytes [206], which also possess receptors for a variety of neurotransmitters [207], in particular glutamate. Moreover, it was demonstrated that the absorption in astrocytes of some neurotransmitters, in particular of glutamate, stimulates glucose uptake, glycolysis and lactate release in the extracellular space [7].

More in detail, the ANLS model (Fig. 4.1) hypothesizes that the glutamate released in the inter–synaptic space, as a consequence of the action potential propagation, is absorbed by astrocytes together with

other ions, mainly Na^+; the increase of the intracellular Na^+ concentration causes an increase over basal level of the Na^+/K^+ ATPase activity, and, thanks to the activity of the glutamine synthetase, the absorbed glutamate is converted in glutamine which is then released outside the astrocyte and absorbed by the neuron where it will be reconverted in glutamate to be reutilized as neurotransmitter. The ATP consumption by the Glu–Gln cycle and by the Na^+/K^+ pump activity primes glucose uptake in astrocytes and the beginning of the glycolysis; at the same time, the glycogenolysis is stimulated, providing further glucose to the glycolysis. Due to the fact that the Krebs cycle is not stimulated in astrocytes, the Lactate DeHydrogenase (LDH) converts the excess of pyruvate in lactate, which then diffuses in the intercellular space and is absorbed into neurons. Finally, within neurons, LDH oxidizes lactate to pyruvate, which enters the Krebs cycle to be completely oxidized by the aerobic metabolism, producing the energy necessary for the neuron.

Also subsequent experimental results have been taken to support the ANLS model. For example, it was found that the GLUcose Transporter protein type 1 (GLUT1) is present in astrocytes and in the endothelium of the Blood–Brain Barrier (BBB) [208]. Another finding was that neurons mainly express the lactate dehydrogenase LDH–1 (more suited to oxidize lactate) while astrocytes mainly express the form LDH–5 (more suited to reduce pyruvate) [209]; this fact, according to the authors, would indicate that lactate is produced in astrocytes and consumed in neurons.

Furthermore Sibson et al. [15] determined the stoichiometry between the oxidative Glc metabolism and the glutamate–neurotransmitter cycling in the cortex to be close to 1 : 1; this finding indicates the close coupling between the neuronal metabolism and the recycling of the glutamine released by astrocytes. Finally, it was proposed by Bliss et al. [210] that lactate may present some advantages as the substrate of choice during neuronal activity, since it can be converted to pyruvate in absence of ATP; this thesis is suggested by the mandatory role of lactate for the recovery of synaptic activity after acute brain pathologies, like ischemia [211–213], or traumatic brain injury [214].

4.5 The fast dynamics of lactate

The literature has reported so far only experiments performed upon prolonged stimulations and with low temporal resolution [8–10]. These

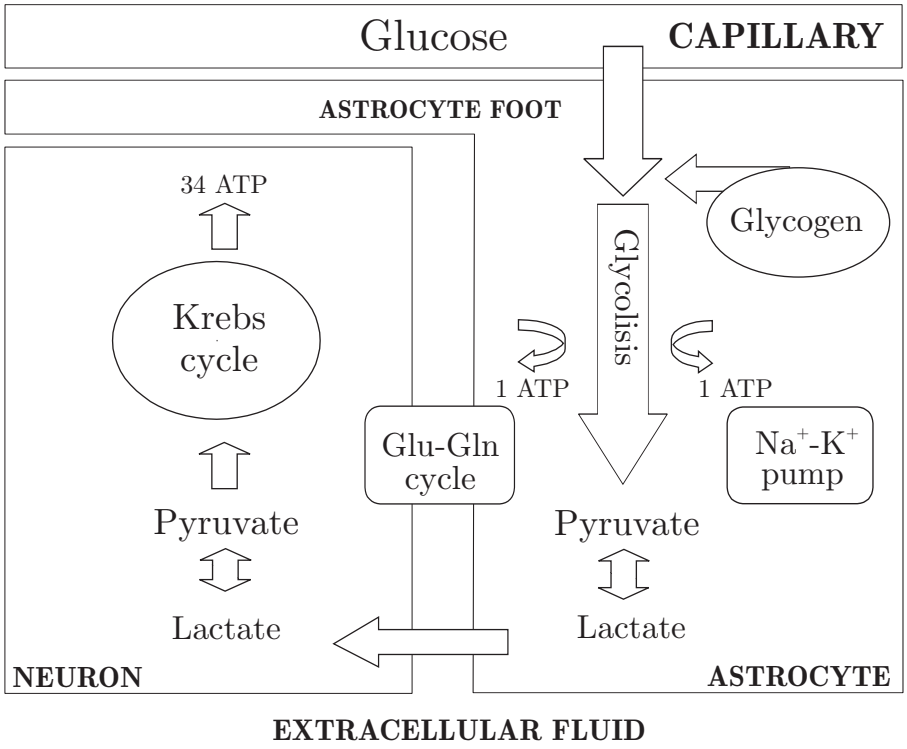

Figure 4.1: The ANLS model: astrocytes undergo 'activation', beginning glycolysis triggered by neurotransmitters, to feed neurons with lactate, which then is the main metabolic substrate of neurons during activation. Direct neuronal uptake of glucose is limited by the unfavorable position of neurons in relation to capillaries. From [12].

studies, performed in vivo by means of ^{1}H–MRS, showed an increase in lactate during the first minutes of stimulation. Nonetheless, it is crucial to investigate the early dynamics of the energetic metabolism, with particular attention to the variations of lactate concentration, since lactate can be a suitable indicator of the coupling between oxygen and glucose consumption. To this purpose, we investigated lactate metabolism with high temporal resolution in order to single out the underlying metabolic events. We utilized an event–related single–voxel ^{1}H–MRS, that measures the time–resolved concentrations of lactate during the first seconds following a very brief visual stimulus, with a temporal resolution of 1 s. This method supplies dynamic information that is impossible to obtain in stationary conditions and avoids the appearance of adaptation and habituation (generally produced by prolonged stimuli) which could mask transient metabolic events. However, one should keep in mind that the

role of lactate can not be completely addressed by this approach alone, first of all because single-voxel spectroscopy can not directly reveal the compartmentation of lactate between glia and neurons, and secondly because it is not possible to discriminate among simultaneous changes in lactate production, consumption and efflux from the region of interest by measuring only lactate concentration. Anyway, this acquisition strategy can provide information suitable to be potentially integrated with the various findings reported in literature in a comprehensive model of energetic metabolism during neural activation.

4.5.1 Methods

Five normal volunteers (aging $23 \div 40$ years) were studied on a whole-body system 1.5 T (Signa Horizon LX, standard birdcage head coil - General Electric Medical Systems, Milwaukee, WI). Written informed consent was obtained from all subjects prior to investigation. The visual stimulation was designed to activate selectively 'interblob' regions of primary visual cortex. These neuronal populations are relatively poor of cytochrome oxidase with respect to the neighboring 'blob' regions [215]. Under these conditions the detection of lactate should be favored. The 'interblob stimulation' consisted of an achromatic square grid of white/black stripes (angular frequency = 6 cycle/°, duty cycle = 50%, eccentricity = 5 °, brightness contrast white/black = 100%) with a central fixation point, on a grey background set at the average brightness of the grid. The projection device was synchronized with the NMR scanner.

In order to obtain the requested temporal resolution during the first seconds following the stimulation, we acquired the spectra in a time-locked modality (Fig. 4.2). This method consists of the presentation of 1 s visual stimulus, followed by a single acquisition after a fixed Acquisition Delay (AD); The time course is investigated by varying the AD in separate sessions. ADs of 0 s, 3 s, 5 s, 8 s and 12 s were utilized. within each session the spectrum was obtained by averaging 128 acquisitions. The rest condition consisted of a uniformly grey image with a central fixation point, asking the volunteer to keep the eyes open. The selection of the VOI, measuring $20 \times 30 \times 20$ mm^3(12 cm^3) and centered on the calcarine fissure, was guided by sagittal SE T_1weighted scans. Proton Nuclear Magnetic Resonance (^{1}H–NMR) single voxel spectra were acquired by using PRESS sequence in fully relaxed conditions (TR ranging between 7500 ms and 15000 ms depending on AD used, TE = 270 ms). Of course, this approach implies that the Inter–Stimuli Interval (ISI)

is equal to the TR. The shorter ISI utilized should be longer that the expected extension of the time–course, to avoid that consecutive spectra measure the metabolic effect of several precedent stimulation, while it is required that each spectrum represents only the metabolic state at AD seconds from the stimulus.

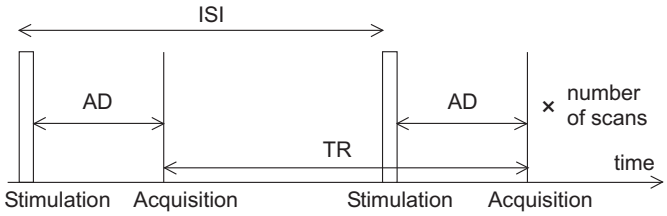

Figure 4.2: Schematic of the time-locked experimental strategy: each spectrum to be averaged is acquired after an Acquisition Delay (AD) from the presentation of a visual stimulus lasting 1 s. Varying the AD it is possible to obtain a lactate time–course during the early moments following a stimulation with high temporal resolution. With this design, the Inter–Stimuli Interval (ISI) is equal to the TR, being the same interval, translated of AD. From [11].

To quantitatively estimate the lactate variations we developed and used an automatic Matlab routine [169] that allows the choice of the baseline and the extremes of integration best suitable for each spectrum. The distribution of lactate and creatine concentration corresponding to each AD was evaluated, and its significance was assessed by ANalysis Of VAriance (ANOVA). Then, if the ANOVA suggested the presence of a dynamics in the metabolite time course, the Least Significant Difference (LSD) and Scheffe post hoc tests were used to closely identify the values statistically different from each other. Equality of variances was verified with Levene's test, while normal distribution of data was visually checked with normal Q-Q plot. The null hypothesis was rejected at 0.01 probability level.

4.5.2 Results

Examples of the spectra obtained on the same subject during rest and after AD of 0 s, 3 s, 5 s, 8 s and 12 s from stimulus presentation are shown in Fig. 4.3, while in Fig. 4.4 we report the intersubject time–course of the lactate variations. These variations are expressed as percentage of the rest level of each individual, in order to remove the large intersubject variability (observed in the range of 100%) of the basal lactate concentration already reported in the literature [192]. As a control

reference we used the creatine peak, which in fact does not exhibit any significant variations at different delays (ANOVA: $p > 0.57$). Within the time–range investigated, the lactate concentration exhibits an appreciable decrease at 5 s and 8 s after stimulation (ANOVA: $p < 0.005$ and $p < 0.008$ respectively, LSD post hoc test). The points corresponding to a delay of 0 s, 3 s, 12 s, are not statistically different from the rest condition. Instead, utilizing a more conservative post hoc test, like the Scheffe test, only the point at 5 s appears significantly different; this fact leads to suppose that 8 s after activation lactate concentration is returning to the basal level. Anyway, our results indicate that the lactate level is surely normalized at 12 s [11].

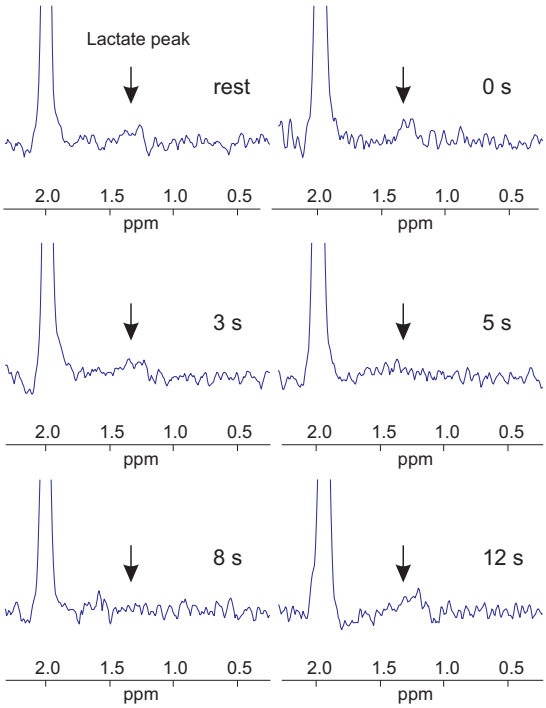

Figure 4.3: Examples of the ^{1}H–NMR spectra obtained in correspondence of rest, and AD of 0 s, 3 s, 5 s, 8 s and 12 s. The lactate peak is marked by an arrow. From [11].

Our findings show a decrease in lactate concentration during the early phase of neural activation. This finding is apparently in contrasts with the increase observed by others during prolonged stimulations [8–10], and suggests that the onset of neural activity is accompanied by lactate consumption. As a further inference, our result is consistent with

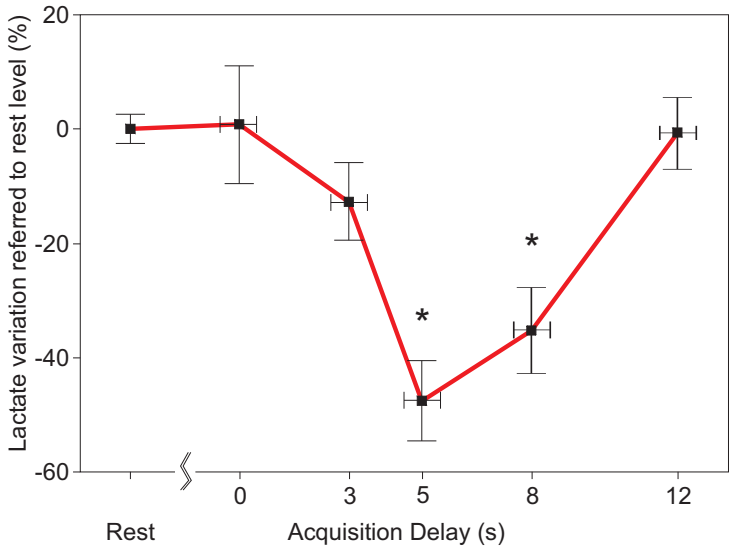

Figure 4.4: Intersubject time–course of lactate percentage variations with respect to the basal level of each individual, after the presentation of a 1 s visual stimulus. The data reported are mean±SD. The values which are significantly different from control are indicated with an asterisk (ANOVA and LSD post hoc test: $p<0.01$). From [11].

an aerobic behavior of neurons from the early stage of their activation. Our result diverges from the ANLS model, since this model should imply an initial lactate overproduction, rather than a lactate decrease, because of a transient uncoupling between astrocytic glycolysis and neuronal oxidation [216].

However, without having quantitative information about the kinetic of lactate production, consumption and transport between neurons and glia, we cannot rule out an intrinsic latency in the start–up of the ANLS; in that case, an initial lactate decrease, followed by an increase over the basal concentration, could be produced. Nevertheless, our data exclude an increase in the lactate amount within 12 s after a brief stimulation, and it is unlikely that further metabolic dynamics could extend after the observed recovery of baseline, given the experimental conditions adopted here (impulsive stimulation). Several findings from other groups challenge the validity of the ANLS model, which is still not supported by definitive experimental evidence [217]. It is the case, for instance, of the presence of highly–specific channels for glucose in neurons [218], the absence of astrocytic metabolic response to increased concentration of neuronal activity indicators such as K^+ [219], and the absence of spe-

cific mechanisms able to ensure lactate transport to neurons without dispersion or leakage [220]. Moreover, the findings of Gjedde and Marrett [221] suggest that, during prolonged stimulations, neurons utilize pyruvate generated directly by neuronal, rather than astrocytic, glycolysis.

Without involving the nutritional coupling between neurons and glia, the lactate depletion we observed could be explained by a transient hypoglycaemia which is likely to happen locally due to the physiological delay in the hemodynamic response to activation. In fact, a regional blood flow increase is reported by the perfusion–based event–related studies just around 5 seconds [222], which correspond to the minimum we observed in lactate concentration. The direct measure of CMR_{Glc} could investigate the hypothesis of a transient condition of hypoglycaemia, but MRS cannot produce this information with temporal resolution high enough to match the results we obtained for lactate. The early use of lactate could have the purpose of replacing glucose when glucose is not available in sufficient amount (i.e. during the first 5 seconds); but, once flow has increased, neurons could use again glucose as the main metabolic substrate. In this way, neuronal energetics would simply change substrate during brain activity due to the changing environmental conditions, without requiring to fulfil all the hypotheses of the ANLS model.

4.6 An intriguing hypothesis: the 'superaerobic' brain

Several conceptual and experimental evidences suggest reformulating the energetic role of lactate and the nutritional coupling between neurons and glia. Some of these motivations are described by Dienel and Hertz [195], who emphasized the ambiguity of the large lactate release observed in cells cultures [7], the likely presence in astrocytes of glucose oxidative metabolism during activation, and the slowness of the rates of metabolism–driven lactate uptake both in astrocytes and neurons. Other motivations are discussed in the works of Chih et al. [217, 223], who, for example, criticized the use of α–cyano–4–hydroxycinnamate (4-CIN) to inhibit the plasmalemmal lactate transport and the use of neonatal cortical cells in in–vitro experiments to evaluate the role of lactate. Moreover, these authors underlined two crucial facts: the first is that the LDH–1/LDH–5 expression respectively in neurons/astrocytes does not imply at all that lactate is produced in astrocyte and consumed in

neurons; the second is that the participation of astrocytic end–feet to the BBB could not be sufficient to demonstrate a preferential uptake of glucose by astrocytes, since neurons have highly–specific channels for glucose – the channel GLUcose Transporter protein type 3 (GLUT3) – which are much more efficient and faster than those of the astrocytes [218].

Other findings, some of them here reported, challenge the validity of the ANLS model:

- the absence of astrocytic metabolic response to increased concentration of neuronal activity indicators such as K^+ [219];
- the evidence that, during prolonged stimulations, neurons utilize pyruvate generated directly by neuronal rather than astrocytic glycolysis [221];
- the model, proposed as a general metabolic pathway, has some experimental evidence only for glutamatergic neurons. No evidence is available to support the existence of an astrocytic response to activity of other classes of neurons (for instance, GABAergic);
- the evidence that lactate concentration decreases in the early phase after stimulation [11], while the ANLS model should imply an initial lactate overproduction, because of a transient uncoupling between astrocytic glycolysis and neuronal oxidation.

.

We would like to focus the attention on the following points.

The absence of a specific transport for lactate

Even if the presence of MonoCarboxylic acid Transporter protein type 1 (MCT1) on astrocytes and of MonoCarboxylic acid Transporter protein type 2 (MCT2) on neurons was considered to support the ANLS model [220] Actually, the absence of a specific mechanism able to ensure lactate transport to neurons without dispersion or leakage it is quite surprising. Lactate transport is passively governed by concentration gradients trough these generic channels, and this is strange if we accept that astrocytic lactate is the mandatory substrate for neurons, as the involved kinetics appears slow and inefficient.

The unresolved question of the 'uncoupling'

Even if the ANLS hypothesis was suggested to imply the reported mismatch between CMR_{Glc} and CMR_{O_2} [10, 211, 212], actually, this de-

duction is quite debatable, because, if the glycolysis in the astrocytes is aimed at producing lactate to be forwarded to neurons and used in the Krebs cycle, then the process as a whole is aerobic, and glucose catabolism is coupled to oxygen consumption. At the most, the ANLS model could predict an increase in CMR_{Glc} without a concomitant increase in CMR_{O_2} only in the early stage of activation, but of course this transient phase reasonably extends in a temporal range of seconds, and not of minutes as hypothesized by Frahm et al. [10]. Only a leakage of astrocytic lactate could account for the well–known mismatch between CMR_{Glc} and CMR_{O_2} [4, 5].

It is advisable to stress that the uncoupling observed by Fox et al. [4, 5] is a stationary mismatch between glucose and oxygen consumption increases during neuronal activity. It is well known that, in resting conditions, the brain energetics is entirely aerobic, with a stoichiometric coupling between glucose and oxygen consumption[4] [50]. Fox et al. measured in the visual cortex [5] a resting consumption of oxygen and glucose of 1.71 ± 0.18 μmol min^{-1}100 g^{-1} and 0.42 ± 0.03 μmol min^{-1}100 g^{-1} respectively, with a resting–state molar ratio of $4.1 : 1$[5]. The visual stimulation induced a 51% increase of CMR_{Glc}, up to 0.63 μmol min^{-1}100 g^{-1}, and only a 5% increase of CMR_{O_2} (up to 1.79 μmol min^{-1}100 g^{-1}). Consequently, the molar ratio between ΔCMR_{O_2} and ΔCMR_{Glc} was only $0.4 : 1$ and this stationary mismatch between metabolic substrates increases led to a ratio CMR_{O_2}/CMR_{Glc} near $2.8 : 1$.

The doubtful advantage of using lactate instead of glucose

Even if lactate was proposed to have some advantages during neuronal activation since it can be converted to pyruvate in absence of ATP [210], actually, in this latter case, lactate should be however produced at the expense of an initial consumption of ATP in astrocytes, then, the energetic convenience is not evident at all, unless neurons had a large basal reserve of lactate. But the basal concentration of lactate is low in human

[4]The complete reaction for glucose aerobic oxidization via glycolysis, Krebs cycle and respiratory chain is:

$$Glc + 36ADP + 36P_i + 36H^+ + 6O_2 \rightharpoonup 6CO_2 + 36ATP + 42H_2O.$$

[5]This value is somewhat less than the canonical value of $6 : 1$. Anyway, PET measurements suffer from several possible systematic effects and are model–dependent. In this context, the essential fact is the remarkable variation between resting and activated molar ratios, measured in the same experimental conditions.

brain, $0.5 \div 1$ mM [168], and a local accumulation of lactate must be avoided not to alter the intracellular redox state.

It is important to note that lactate is preferentially used instead of glucose only when lactate is present in high amounts, as shown just by Bliss et al. [210]. Nevertheless, while accumulation of lactate is a known effect of acute brain pathologies (so the consumption of lactate during the recovery phase could also have the purpose of cleaning the environment from this 'waste' damage product), it unlikely occurs during neuronal activation, since brain lactate concentration increases slightly during physiological stimulations [8]. Moreover, recent findings have shown that lactate can support only some neuronal functions within some neuronal populations [217], and that among the supported functions a normal synaptic activity is not guaranteed [224].

A different hypothesis about the roles of lactate and astrocytes

In our opinion, astrocytes do undergo metabolic activation by beginning glycolysis triggered by neurotransmitters, as stated in the ANLS model as well, but only in order to support the Glu–Gln cycle [15], which removes neurotransmitters from the intersynaptic space in order to avoid a saturation of the stimulation. Beside this 'cleaning' function, glia could certainly have other functional tasks, for example it has been recently proposed that they could be intimately involved in brain information processing [225]. However, a major nutritional role for them does not seem to be acceptable, since this hypothesis implies too many ambiguities, as largely above discussed.

Of course, it is reasonable that part of lactate produced in astrocytes, as a consequence of glycolysis, is conveyed to neurons; anyway, here it would be metabolized together with the main neuronal metabolic substrate, which is the glucose directly uptaken trough the high specific receptors GLUT3 (Fig. 4.5). In this way, the neuronal consumption of lactate would have the twofold meaning of reducing the excess of lactate and coping with the energetic demand if needed, without necessarily being the final aim of astrocytic activation.

Supporting this interpretation, we observed a lactate decrease under its rest level in the first seconds following an impulsive stimulation [11]. This result suggests that the lactate consumed in this stage is not provided entirely by astrocytes. Indeed, lactate appears to be equally accumulated in neurons and astrocytes [195]. Moreover, the early lactate consumption can be explained by a transient hypoglycaemia which

is likely to happen locally due to the physiological delay in the hemodynamic response to activation. In fact, a regional blood flow increase is reported by the perfusion–based event-related studies just around 5 seconds [222], which correspond to the minimum observed in lactate concentration [11]. Then, the use of lactate would have the purpose of replacing glucose when glucose is not available in sufficient amount (i.e. during the first 5 seconds), while, once the flow has increased, it is reasonable that neurons use again glucose as their principal metabolic substrate. In other words, neuronal energetics would change substrate during brain activity due to the changing environmental conditions, and would not require the hypothesis of a specialized mechanism to feed neurons.

By accepting this more traditional picture of neuronal energetics, the several ambiguities previously described are consequently solved. In particular, the absence of an efficient mechanism for lactate transport is not surprising if astrocytes are not required to feed neurons. Furthermore, the uncoupling between CMR_{Glc} and CMR_{O_2} can be accounted for. Indeed, when lactate concentration increases due to the activation of astrocytes, lactate diffuses through the generic channels in the intercellular space surrounding astrocytes. Following the gradients of concentration, part of this exogenous lactate will go into activated neurons where it can be oxidized together with glucose, and the remaining will go into blood vessels [193], or will diffuse towards other brain regions. Consequently, an amount of glucose consumed by astrocytes to produce lactate would be subtracted from the utilization in the Krebs cycle and, thus, would be uncoupled to the oxygen consumption, originating the previously discussed mismatch, that is a major experimental finding not accounted by the ANLS model.

Numerous findings present in literature appear not to perfectly fit into the largely accepted hypothesis of glia feeding neurons with lactate (ANLS model), at least in its stronger formulation, of obliged and 'stoichiometric' coupling between neuronal and astrocytic metabolism [226]. The return to a more traditional description of neuronal energetics, in which neurons can metabolize directly uptaken glucose to support their activity, at least during some stage of their activation, allows an easier 'solution of the puzzle', where both the points in favor of and the points contrary to the ANLS model, may find a more appropriate collocation.

Important findings supporting this view were recently reported by Kasischke et al. [227]. By means of the intrinsic β–Nicotinamide Adenine Dinucleotide (NADH) fluorescence, they observed in hippocampal slice a spatiotemporal partitioning of glycolytic and aerobic metabolism

between astrocytes and neurons during stimulation: an early aerobic metabolism confined in neurons is eventually sustained by late activation of the ANLS. This interpretation is compatible with the initial decrease of lactate observed by us, as the initial aerobic stage implies the consumption of metabolic substrates (glucose and/or lactate) not produced by the astrocytes.

According to this model, the transient mitochondrial NADH oxidation is the direct consequence of respiratory chain activation as the physiological event underlying the macroscopic signs of aerobic metabolism, all of which occur within the first seconds after onset of induced activity. These results confirm that early neuronal aerobic metabolism is the default response to increased neural activity. Only after a significant period (10 s) with possible depletion of substrates for oxidative metabolism (mainly lactate [11, 228]) is the astrocytic glycolysis activated.

Thereby, extracellular lactate might serve as a buffer preventing activation of the ANLS during minor or short–lasting neural activity. The observation that the transient NADH production as an indicator of glycolysis in astrocytes exceeds neuronal NADH consumption and further increases with longer stimulation strengthens this interpretation.

The further (difficult) step is the exact determination of the degree of activity normally sustained without the ANLS activation. It is possible that normal, 'physiological' activity doesn't require the intervention of astrocytes, and that only prolonged activations trigger the lactate shuttle, just as suggested in our model [11, 12].

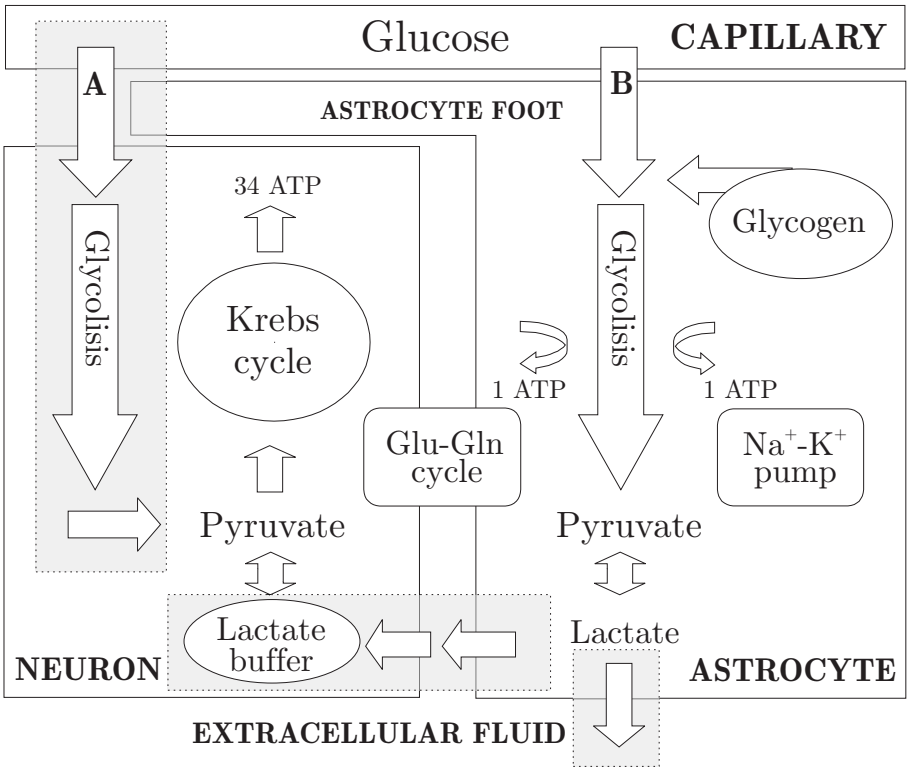

Figure 4.5: Alternative to the ANLS model: astrocytes activate themselves, beginning glycolysis triggered by neurotransmitters (B), simply to support the Glu-Gln cycle, which cleans the intersynaptic space from neurotransmitters. The unfavorable position of neurons in relation to capillaries is not limiting for the direct glucose uptake (A), thanks to the high specific receptors GLUT3 present in neurons. Part of lactate produced in astrocytes is conveyed to neurons, and used together with the principal neuronal metabolic substrate, which is the glucose directly uptaken by neurons. In this way part of lactate can be recycled if needed, leading to an optimal use of all the available metabolic substrates. The lactate consumed in the first moments is already reasonably present in neurons (lactate buffer), in dynamic equilibrium with pyruvate. The shaded regions emphasize the modifications made to the ANLS model. From [12].

CHAPTER 5

Conclusions

The main aim of the work described in this Thesis was to provide more detailed and accurate information on the CNS activation. In this framework, a method to obtain high–temporally–resolved MRS spectra and an adequate spectra quantification method were developed and applied.

Our results on brain metabolism under activation [11, 12] showed a *dynamic* decrease and a subsequent increase of lactate in the active brain, in the few seconds following an impulsive stimulation. These results are quite interesting and unexpected, as every lactate measurement in past studies showed a stationary increase of lactate, on temporal scales of minutes. This finding conducted us to slightly reformulate the ANLS model, deemphasizing the role of lactate and hypothesizing that cerebral metabolism switches from purely aerobic to partially anaerobic (due to astrocytic contribution), while neuronal metabolism remains aerobic in every phase. This view address both the mismatch between oxygen and glucose consumption [4], the increase of lactate during long stimulations [8] and the dynamic decrease observed by us [11].

In a recent, important article [227] an analogue triggering of astrocytic glycolysis by neuronal aerobic metabolism was observed with two–photon fluorescence imaging on an hippocampal slice preparation. The observation of an early lactate consumption by neurons is giving a contribution to a further developing of our knowledge of the brain activity.

Useful information on BOLD contrast and in particular on the influence of the vascular network structure on its generation can be provided by the studies on spinal cord functional activity. Obviously, further in-

vestigations are required to identify the experimental conditions more suitable to reliably obtain functional maps of the spinal cord activation, and to assess the specificity of the observed signal and its relationships with the underlying neuronal activity. However, spinal cord fMRI in healthy and injured subjects would probably become a valuable clinical and scientific tool for the non–invasive assessment of spinal cord function.

The contributions of several Nuclear Magnetic Resonance techniques to the knowledge of the CNS are important, and would bring to further increase with the integration of different modalities, like PET and Electro–EncephaloGraphy (EEG), in the same experimental session. This integration is predicted to greatly increase the obtainable data, compensating the weaknesses of each technique, with the integration of complimentary information.

Nonetheless, a key feature for a further development of our knowledge of the human brain by Nuclear Magnetic Resonance techniques is the availability of ultra–high field magnets (7 T and above). They have been used in human research only recently. The results published so far indicate that significant improvements can be obtained in many applications in the fields of MR imaging (functional and anatomic) and spectroscopy (of proton and of low–γ nuclei) [31].

During the last decade an increasing amount of experimental data on brain function has been produced. A clear vision of how the human brain works is still not possible, and the research on the higher mental functions is just at the beginning. However it is evident that the unpaired ability of NMR to obtain information on the brain in a non–invasive way, and the continuous developing of new NMR–based techniques, give us an incredible cognitive power. The correct and full exploitation of this power lies with us.

APPENDIX A

An outlook on an alternative fMRI technique: perfusion imaging

Functional techniques of neuroimaging based on a metabolic-vascular approach, such as fMRI or PET, reveal neuronal activation in terms of an increase in measured signal during the execution of a task, when compared to a control state, with lower or different functional involvement. This response reflects the task–induced switch between two different levels of neuronal activity [1].

Areas showing a significant decrease of the signal have also been observed during functional fMRI and PET experiments [229–233]. Were the relationship linking neuronal firing, local metabolism and circulation hold true also for decreased synaptic activity, then the signal decrease could well be regarded as related to neuronal deactivation [230]. With this in mind, the investigation of signal decreases proves quite intriguing, especially given that many decreases appear to be largely task–independent [230]. This fact supports the idea of an organized mode of brain function that is present as a baseline or default state, and suggests a modern approach to functional studies. One example of this is that suggestive deactivations of the limbic and paralimbic structures have recently been observed during cognitive tasks [233], and have been ascribed to an inhibition of emotional activity in order to improve the performance during on–going higher cognitive processing.

Several possible scenarios are compatible with the presence of task–related signal decreases, and the investigation of the physiological origins of such phenomena, together with the definition of the intrinsic meaning

of 'neuronal deactivation', has become an issue of debate. A reduced neural activity, when intended as a drop in the neural firing, can in fact result either from decreased neural input, or from an increase in synaptic inhibition due to local GABA release. The former case is associated with decreased glucose consumption and CBF, whereas the latter one causes a rise in energy demands and CBF.

Metabolic–vascular approaches can thus reveal the cortical regions where the afferent function decreases, but they are not capable of distinguishing between the zones of inhibition and those of excitation [2]. The fact that the afferent function, and not the neuronal spiking, determines all properties of the functional hemodynamic signals has widely been demonstrated by Logothetis et al. [1] and by Lauritzen [2]. The conclusion drawn from these observations is that, in this context, neuronal deactivation merely refers to a decreased input to a brain region.

As regards the physiological genesis of signal decreases, Harel et al. [234] suggested caution when interpreting the negative signals as deactivations, given that a simple hemodynamic effect, consisting of the so–called vascular steal, can also generate such phenomena. They indeed observed a reduction of both the BOLD signal and cerebral blood volume in higher–order visual areas of the anaesthetized cat in response to full–field drifting gratings, whereas such regions are known to increase their neural activity during the task used. Somewhat similar experiments were conducted on conscious humans at 7 T by Shmuel et al. [235]. Following a partial visual field stimulation, some areas in the medial occipital cortex, strictly adjacent to the activated regions of the primary visual cortex, exhibited a drop in both the BOLD signal and cerebral blood flow. Given the stimulation used, the authors excluded an increase of neural activity in such areas; on the contrary, they showed that a reduction of the oxygen consumption rate can be deduced by applying Hoge's model [124], thus inferring that the observed phenomenon originated from a decreased neural activity (albeit that a contextual intervention of a pure hemodynamic effect was not excluded). Most importantly, neuronal deactivation, as emphasized by Gusnard et al. [236], seems to be the most suitable mechanism whenever the signal decreases are located in spatial positions which are remote from the regions where the positive signal changes take place, as the premise of a vascular steal would only be applicable to areas strictly adjacent to the activated tissue, at least in physiological conditions.

Such considerations imply ambiguity in interpreting signal decreases. As a first step of investigation, before inferring deductions about the

physiology and role of deactivation, we believe that it is essential to verify if different functional techniques give congruent results. In the studies conducted by Harel et al. [234] and by Shmuel et al. [235], overlapping areas exhibiting a drop in BOLD and perfusion signals were shown in the visual region in correspondence of partial visual stimulation. The determination of whether or not the convergence of perfusion and BOLD data also holds true in different cortices was the main purpose of our experiment. To address this question, we focused on a human pathological model of task–related flow reduction, namely an ArterioVenous Malformation (AVM). It is known that the AVM presence determines a global redistribution of brain perfusion. Function–related phenomena of flow steal can be expected in such pathologies, due to an increased flow in the AVM which subtracts blood flow to other brain areas [237]. The presence of a large AVM thus creates ideal conditions for studying how decreases in regional blood flow are detected by functional MRI, and combined BOLD–perfusion experiments can be applied to evaluate the relative sensitivity of different functional MRI approaches to reductions in CBF. In particular, we utilized an Arterial Spin Labeling (ASL) sequence to obtain BOLD maps and perfusion maps in the same experimental session.

Methods

A 30 year–old patient affected by a large AVM of the superior frontal gyrus of the right hemisphere, associated with an isolated enlargement of the lateral ventricle of the same hemisphere, was examined on a whole–body 1.5 T system (GE Signa Horizon LX, standard birdcage head coil). The patient was neurologically normal, except for a slight impairment in the movement of the toes of his left foot. Written informed consent, according to the declaration of Helsinki, was obtained prior to investigation.

In order to evaluate the basal condition of brain blood circulation, perfusion–weighted images were acquired utilizing the multi–slice Flow–sensitive Alternating Inversion–Recovery (FAIR) sequence introduced by Yang et al. [238]. The sequence parameters were: thickness of the inversion slab = 100 mm, TE = 25 ms, TR = 56 ms, Inversion Time (TI) = 1.2 s, delay time = 3 s, number of slices = 10, slice thickness = 5 mm, number of repetitions = 100 (50 slice–selective and 50 non–selective inversion recovery images).

The patient was then studied during a simple motor task (finger–

tapping of the left hand), utilizing the FAIR sequence (delay time= 1.8 s, the other parameters are described above) in order to obtain perfusion–based and BOLD–based functional maps. The BOLD maps resulted from the detection of the BOLD effect, as revealed by the analysis of the FAIR images acquired in the absence of selective inversion. The functional stimulation consisted of a block–designed paradigm with 10 task periods of motor stimulation which alternated with 10 periods of rest. Each period lasted for 10 functional volumes, and each volume was composed of 10 slices. The original time–series of 200 volumes preliminary underwent a motion–correction procedure based on the Levenberg-Marquart's least square fit of two translational and one rotational parameters. Linear drifts were removed from the time–series, and a bi–dimensional spatial filter was applied to each image slice using a 6 mm FWHM gaussian kernel. Two subseries of 100 repetitions of tagged and non–tagged volumes were subsequently extracted from the 200 volumes time–series. In order to produce the time–series of perfusion–weighted images, the two subseries first underwent a scan–by–scan subtraction. This combination produced the image time–series which were used in perfusion–based signal change detection. Ordinary functional time–series, to be used in BOLD contrast mapping, were obtained by considering the partial time–series of non–selectively inverted volumes. CBF and BOLD activation maps were generated by performing Student t–test for each voxel between rest and task conditions. Since BOLD–based and perfusion–based functional maps do not exhibit the same CNR (with the former being higher than the latter [124]), applying the same threshold to the correspondent t–score images was not useful for descriptive purposes. In order to optimize the visual comparison of the resulting readouts of brain activity, it was assumed that both methods could reproduce the same positively activated areas in the primary motor cortex as identified by one of the two methods. Statistical maps of perfusion responses were generated choosing a threshold correspondent to $p< 0.05$, and the threshold for the BOLD maps was then adjusted to realize the same number of positively activated voxels in the primary motor cortex of the perfusion maps, which intrinsically possess an higher degree of specificity [239, 240]. A similar approach was used in the studies by Luh et al. [239] and by Shmuel et al. [235] to evaluate the different locations of the same number of activated and, respectively, deactivated pixels revealed by perfusion and BOLD. Here, since we were interested in investigating the sensitivity of the two methods to task–related signal decreases, we decided to fix only the number of positively activated

pixels in the primary motor cortex. Minimum cluster size was not imposed. The red–yellow colors were chosen to represent positive t–score values (task–related signal increases), while the blue–cyan colors indicated negative t–score values (task–related signal decreases). Functional maps were finally overlaid to the mean (static) reference image slices.

Results

The perfusion-weighted images acquired in basal condition (Fig. A.1) reveal a strong flow increase in the superior frontal cortex of the right hemisphere, corresponding to the nidus of the AVM. Less evident are a decreased flow in the most posterior right occipito–parietal cortex and a slight decrease in the dorsal frontal cortex compared with the left (normal) side. The ventricular enlargement is recognizable as hypointense.

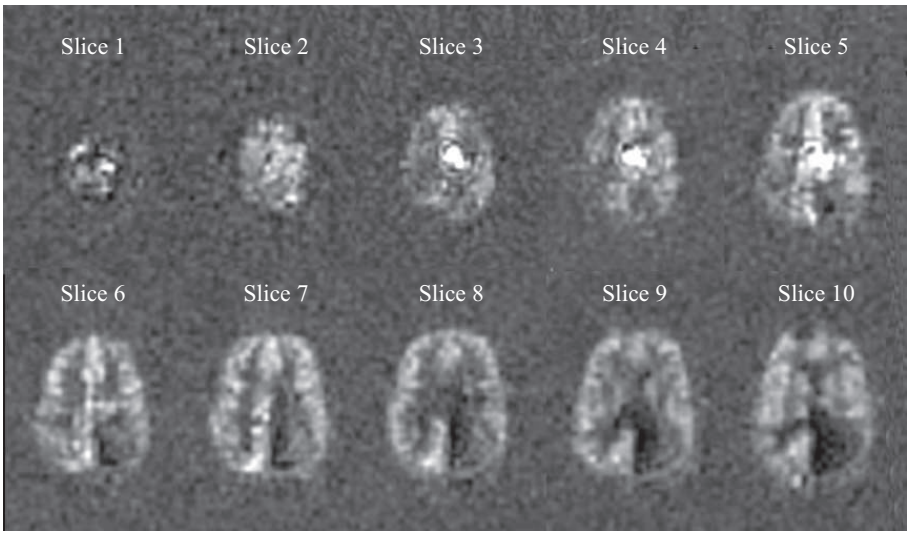

Figure A.1: Perfusion–weighted images of the examined patient affected by an AVM associated with an isolated enlargement of the lateral ventricle of the same hemisphere. The images were acquired utilizing a multislice FAIR sequence. From [241].

The perfusion–based and the BOLD–based functional maps obtained in the present study (Fig. A.2) are basically similar, since both depict the expected motor activation in the right rolandic cortex. Several marked difference exist, however, one of which being that in the functional perfusion map it is more evident that the activation of the motor cortex in the right side is accompanied by a decreased CBF in the frontal and occipito–parietal territories subserved by branches of the anterior, mid-

dle and posterior cerebral arteries. This evidence can be explained by the steal phenomena which can be induced by the presence of the AVM. The perfusion map also shows a more evident activation of the ipsilateral motor cortex, whereas there is no activation in the supplementary motor region, present in the BOLD map.

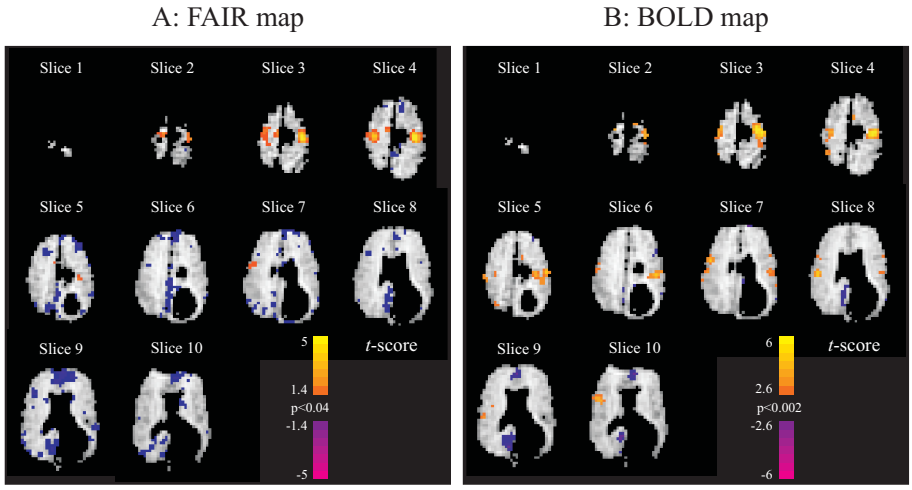

Figure A.2: A: Perfusion–based activation map obtained through the FAIR sequence during a motor activation of the left hand. B: Activation map obtained by revealing the BOLD effect present in the images of the FAIR time–series without the selective inversion. Color bar indicates t–score values. Negative t–score values occur for task–related signal decreases. From [241].

Investigating the sensitivity of BOLD and perfusion MRI to flow–reductions holds a particular interest. Our results, obtained on a pathological model for flow–reductions, deriving from task–related flow–steal, show that the ASL technique is capable of detecting the areas where a task–related CBF decrease occurs as a vascular consequence of the pathology examined (Fig. A.2 A). On the other hand, the spatial extents of the regions of decreased perfusion signal differ from what revealed by BOLD maps (Fig. A.2 B). As the perfusion–based maps must be taken as a reference in the detection of vascular phenomena, the above finding indicates that BOLD maps can be susceptible to ambiguities in the detection of reduced flow areas, and, specifically, might underestimate flow decreases. Given that flow reductions in physiological conditions can be related to a decreased functional activity [2] (if phenomena of vascular steal are known not to occur), we further suggest that perfusion functional maps may prove generally more reliable than BOLD maps in the

localization of deactivated areas.

In principle, the perfusion–based fMRI approach also shows several advantages over the BOLD–based approach in the detection of deactivated areas. By virtue of its high spatial specificity [239, 240], perfusion–based fMRI has been proposed as gold standard [242] for functional imaging. As demonstrated by Lauritzen [2], the degree of perfusion is highly correlated with the neural input of the system, and flow reductions are expected in correspondence to deactivation due to decreased input, although it might occur that large deactivations are represented by very moderate changes of blood flow [243]. Therefore, whenever flow–steal phenomena can be excluded by other a–priori knowledge, perfusion methods enable a plain interpretation of decreased signal in terms of neuronal deactivation, without involving over–reaching hypotheses about a complex interplay of more metabolic–vascular parameters.

As regards the BOLD contrast, on the other hand, Logothetis et al. [1] have firmly assessed a linear correlation between neural activity (specifically, the neural input) and BOLD contrast in the primary visual cortex of anesthetized monkeys. This finding unambiguously demonstrates the link between neuronal electric events and metabolic–vascular phenomena. Despite the above evidence, it should be recalled that BOLD contrast can suffer from poor spatial specificity, and false activations can be observed in draining veins, especially for single–condition mapping [3]. Furthermore, the dynamics of the local metabolic-vascular parameters might result from the interaction of several modulation factors, which may be typical to each single subject, each single physiological condition and each single brain region [98]. BOLD signal decreases could thus occur (apart from in regions eventually interested by vascular steal) in activated regions with a modified metabolic–vascular dynamics, where the consumption rate or the local blood volume would increase more than blood flow. Such an eventuality would imply the production of false deactivations.

The detection of deactivated areas gathers the opportunity to greatly extend our knowledge of brain function, as it permits the in–depth study of the potential suppression of information processing in regions that are not engaged in task performance. Nonetheless, the presence of task–related signal decreases does not necessarily imply deactivation phenomena, and relating measured signals with deactivation phenomena remains a challenge for scientific research. Although the occurrence of decreases in CBF was not physiologically related to the activation, but was rather generated from recognized pathological phenomena, the re-

sults obtained in the present study encourage an extensive application of functional perfusion MRI in the study of deactivation.

APPENDIX B

Acronyms

^{1}H–NMR	Proton Nuclear Magnetic Resonance
^{1}H–MRS	Proton Magnetic Resonance Spectroscopy
^{13}C–MRS	Carbon Magnetic Resonance Spectroscopy
4-CIN	α–cyano–4–hydroxycinnamate
AD	Acquisition Delay
Ala	L–alanine
ANLS	Astrocyte–Neuron Lactate Shuttle
ANOVA	ANalysis Of VAriance
ASL	Arterial Spin Labeling
Asp	Aspartate
ATP	Adenosine TriPhosphate
AVM	ArterioVenous Malformation
BBB	Blood–Brain Barrier
BOLD	Blood–Oxygenation Level–Dependent
CBF	Cerebral Blood Flow
CBO	Cerebral Blood Oxygenation
CBV	Cerebral Blood Volume
CV	Coefficient of Variation
Cho	Choline
CMR_{Glc}	Cerebral Metabolic Rate of Glucose
CMR_{O_2}	Cerebral Metabolic Rate of Oxygen
CNR	Contrast–to–Noise Ratio
CNS	Central Nervous System

Cr	Creatine
CSF	Cerebro–Spinal Fluid
CRLB	Cramér–Rao Lower Bounds
dHb	deoxyhemoglobin
DSS	2,2–dimethyl–2–silapentane–5–sulfonate
DTI	Diffusion Tensor Imaging
EEG	Electro–EncephaloGraphy
EPI	Echo Planar Imaging
FA	Flip Angle
FAIR	Flow–sensitive Alternating Inversion–Recovery
FID	Free Induction Decay
FLASH	Fast Low Angle SHot imaging
fMRI	functional Magnetic Resonance Imaging
FOV	Field Of View
FSE	Fast Spin Echo
FWHM	Full–Width Half–Maximum
GE	Gradient Echo
GABA	γ–AminoButyric Acid
Glc	D–glucose
Gln	L–glutamine
Glu	L–glutamate
GLUT1	GLUcose Transporter protein type 1
GLUT3	GLUcose Transporter protein type 3
Glx	sum of L–glutamate and L–glutamine
Gly	Glycine
HbO_2	oxyhemoglobin
HLSVD	Hankel Lanczos Singular Values Decomposition
hrf	hemodynamic response function
ISI	Inter–Stimuli Interval
Lac	Lactate
LDH	Lactate DeHydrogenase
LSD	Least Significant Difference
MCT1	MonoCarboxylic acid Transporter protein type 1
MCT2	MonoCarboxylic acid Transporter protein type 2
mI	Myo–inositol
MM	MacroMolecules
MR	Magnetic Resonance

MRI	Magnetic Resonance Imaging
MRS	Magnetic Resonance Spectroscopy
MWA	Migraine With Aura
MWOA	Migraine WithOut Aura
NAA	N–acetyl–L–aspartate
NAAG	N–acetyl–L–aspartylglutamate
NADH	β–Nicotinamide Adenine Dinucleotide
NIRS	Near InfraRed Spectroscopy
NMDA	N–Methyl–D–Aspartate
NMR	Nuclear Magnetic Resonance
OEF	Oxygen–Extracted Fraction
PCr	PhosphoCreatine
PET	Positron Emission Tomography
P_i	Inorganic Phosphate
PFC	PerFluoroCarbon
PRESS	Point–RESolved Spectroscopy
Scyllo	Scyllo–inositol
SD	Standard Deviation
SE	Spin Echo
SEEP	Signal Enhancement by Extravascular water Protons
SNR	Signal–to–Noise Ratio
SSFSE	Single Shot Fast Spin Echo
SVD	Singular–Value Decomposition
Tau	Taurine
TCA	TriCarboxylic Acid
TE	Echo Time
TI	Inversion Time
TR	Repetition Time
VOI	Volume Of Interest

APPENDIX C

Publications

Edited books

1) Proceedings of the International School on Magnetic Resonance and Brain Function, edited by Bruno Maraviglia, Federico Giove, and John C. Gore, Magnetic Resonance Imaging, Volume 21, Issue 10, Pages 1111-1332 (December 2003).

International papers

1) S. Mangia, F. Giove, M. Bianciardi, F. Di Salle, G. Garreffa, B. Maraviglia. Issues about the construction of a metabolic model for neuronal activation. *J. Neurosci. Res.*, 71:463–467 (2003).
2) S. Mangia, G. Garreffa, M. Bianciardi, F. Giove, F. Di Salle, B. Maraviglia. The aerobic brain: lactate decrease at the onset of neural activity. *Neuroscience*, 118:7–10 (2003).
3) M. A. Macrì, G. Garreffa, F. Giove, A. Ambrosini, M. Guardati, F. Pierelli, J. Schoenen, C. Colonnese, B. Maraviglia. Cerebellar metabolite alterations detected in vivo by proton MR spectroscopy. *Magn. Reson. Imaging*, 21:1201–1206 (2003).
4) F. Giove, S. Mangia, M. Bianciardi, G. Garreffa, F. Di Salle, R. Morrone, B. Maraviglia. The physiology and metabolism of neuronal activation: "in vivo" studies by NMR and other methods. *Magn. Reson. Imaging*, 21:1283–1293 (2003).

5) S. Mangia, F. Di Salle, G. Garreffa, F. Esposito, F. Giove, S. Cirillo, R. Morrone, B. Maraviglia. Perfusion–based fMRI in the study of a pathological model for neuronal deactivation. *Brain Res. Bull.*, 63:1–5 (2004).
6) F. Giove, G. Garreffa, G. Giulietti, S. Mangia, C. Colonnese, B. Maraviglia. Issues about the functional MR Imaging of the human spinal cord. *Magn. Reson. Imaging*, 22:1505–1516 (2004).
7) M. A. Macrì, G. Garreffa, F. Giove, M. Guardati, A. Ambrosini, C. Colonnese, B. Maraviglia. In vivo quantitative ^{1}H–MRS of cerebellum and evaluation of quantitation reproducibility by simulation of different levels of noise and spectral resolution. *Magn. Reson. Imaging*, 22:1385–1393 (2004).

Conference contributions — refereed

1) S. Mangia, G. Garreffa, M. Bianciardi, F. Giove, F. Di Salle, R. Morrone, B. Maraviglia. Lactate concentration during neuronal activation studied by ^{1}H–MRS. Proceedings INFMeeting, National Conference on the Physics of the Matter, Roma (Italy), 18–22 June 2001, pag. 159.
2) S. Mangia, G. Garreffa, F. Di Salle, R. Morrone, F. Giove, B. Maraviglia. Evaluation of cerebral perfusion by ASL (Arterial Spin Labeling) techniques in healthy and pathological condition. Proceedings INFMeeting, National Conference on the Physics of the Matter, Roma (Italy), 18–22 June 2001, pag. 104.
3) S. Mangia, F. Giove, M. Bianciardi, G. Garreffa, F. Di Salle, B. Maraviglia. Lactate dynamics during activation of the human visual cortex. 9th Annual Meeting of the Organization for Human Brain Mapping, New York (USA), 18–22 June 2003. Available on CD-ROM in NeuroImage, AbsTrak ID: 18747
4) F. Giove, S. Mangia, G. Garreffa, G. Giulietti, C. Colonnese, B. Maraviglia. Functional NMR imaging of the spinal cord at 1.5 T. Proceedings INFMeeting, National Conference on the Physics of the Matter, Genova (Italy), 23–25 June 2003, pag. 85–86.
5) M. A. Macrì, G. Garreffa, F. Giove, A. Ambrosini, M. Guardati, F. Pierelli, J. Schoenen, C. Colonnese, B. Maraviglia. An in vivo ^{1}H–MRS investigation of cerebellum: an alternative approach for the assessment of some metabolic dys-

functions. Proceedings INFMeeting, National Conference on the Physics of the Matter, Genova (Italy), 23–25 June 2003 , pag. 108.

6) F. Giove, S. Mangia, G. Garreffa, G. Giulietti, C. Colonnese, B. Maraviglia. Functional MR imaging of the human spinal cord at 1.5 T. 10^{th} Annual Meeting of the Organization for Human Brain Mapping, Budapest (Hungary), 14–17 June 2004. Available on CD-ROM in NeuroImage, Vol. 22.

References

[1] Logothetis NK, Pauls J, Augath M, Trinath T, Oeltermann A. Neurophysiological investigation of the basis of the fMRI signal. *Nature*, 412:150–157 (2001).

[2] Lauritzen M. Relationship of spikes, synaptic activity, and local changes of cerebral blood flow. *J. Cereb. Blood Flow Metab.*, 21:1367–1383 (2001).

[3] Uğurbil K, Toth L, Kim DS. How accurate is magnetic resonance imaging of brain function? *Trends Neurosci.*, 26:108–114 (2003).

[4] Fox PT, Raichle ME. Focal physiological uncoupling of cerebral blood flow and oxidative metabolism during somatosensory stimulation in human subjects. *Proc. Natl. Acad. Sci. USA*, 83:1140–1144 (1986).

[5] Fox PT, Raichle ME, Mintun MA, Dence C. Nonoxydative glucose consumption during focal physiologic neural activity. *Science*, 241:462–464 (1988).

[6] Malonek D, Grinvald A. Interactions between electrical activity and cortical microcirculation revealed by imaging spectroscopy: implications for functional brain mapping. *Science*, 272:551–554 (1996).

[7] Pellerin L, Magistretti PJ. Glutamate uptake into astrocytes stimulates aerobic glycolysis: a mechanism coupling neuronal activity to glucose utilization. *Proc. Natl. Acad. Sci. USA*, 91:10625–10629 (1994).

[8] Prichard J, Rothman D, Novotny E, Petroff O, Kuwabara T, Avison M, Howseman A, Hanstock C, Shulman R. Lactate rise detected by ^{1}H–NMR in human visual cortex during physiologic stimulation. *Proc. Natl. Acad. Sci. USA*, 88:5829–5831 (1991).

[9] Sappey-Marinier D, Calabrese G, Fein G, Hugg JW, Biggins C, Weiner MW. Effect of photic stimulation on human visual cortex lactate and phosphates using ^{1}H and ^{31}P magnetic resonance spectroscopy. *J. Cereb. Blood Flow Metab.*, 12:584–592 (1992).

[10] Frahm J, Kruger G, Merboldt KD, Kleinschmidt A. Dynamic uncoupling and recoupling of perfusion and oxidative metabolism during focal brain activation in man. *Magn. Reson. Med.*, 35:143–148 (1996).

[11] Mangia S, Garreffa G, Bianciardi M, Giove F, Di Salle F, Maraviglia B. The aerobic brain: lactate decrease at the onset of neural activity. *Neuroscience*, 118:7–10 (2003).

[12] Mangia S, Giove F, Bianciardi M, Di Salle F, Garreffa G, Maraviglia B. Issues concerning the construction of a metabolic model for neuronal activation. *J. Neurosci. Res.*, 71:463–467 (2003).

[13] Duncan GE, Stumpf WE, Pilgrim C. Cerebral metabolic mapping at the cellular level with dry–mount autoradiography of[3H]2-deoxyglucose. *Brain Research*, 401:43–49 (1987).

[14] Magistretti PJ, Pellerin L. The contribution of the astrocytes to the 18F–2–deoxyglucose signal in PET activation studies. *Molecular Psychiatry*, 1:445–452 (1996).

[15] Sibson NR, Dhankhar A, Mason GF, Behar KL, Rothman DL, Shulman RG. In vivo ^{13}C NMR measurements of cerebral glutamine synthesis as evidence for glutamate–glutamine cycling. *Proc. Natl. Acad. Sci. USA*, 94:2699–2704 (1997).

[16] Thulborn KR, Waterton JC, Matthews PM, Radda GK. Oxygenation dependence of the transverse relaxation time of water protons in whole blood at high field. *Biochem. Biophys. Acta*, 714:265–270 (1982).

[17] Ogawa S, Lee TM, Kay AR, Tank DW. Brain magnetic resonance imaging with contrast dependent on blood oxygenation. *Proc. Natl. Acad. Sci. USA*, 87:9868–9872 (1990).

[18] Ogawa S, Menon RS, Tank DW, Kim SG, Merkle H, Ellermann JM, Uğurbil K. Functional brain mapping by blood oxygenation level-dependent contrast magnetic resonance imaging. A comparison of signal characteristics with a biophysical model. *Biophys. J.*, 64:803–812 (1993).

[19] Menon RS, Ogawa S, Tank DW, Uğurbil K. 4 Tesla gradient recalled echo characteristics of photic stimulation-induced signal changes in the human primary visual cortex. *Magn. Reson. Med.*, 30:380–386 (1993).

[20] Song AW, Wong EC, Tan SG, Hyde JS. Diffusion weighted fMRI at 1.5T. *Magn. Reson. Med.*, 35:155–158 (1996).

[21] Uğurbil K, Ogawa S, Kim SG, Hu X, Chen W, Zhu X. Imaging brain activity using nuclear spins. In *Proceedings of the International School of Physics "Enrico Fermi"*, edited by B Maraviglia, 261–310. IOS Press, Amsterdam, 1999.

[22] Fransson P, Kruger G, Merboldt K, Frahm J. Temporal characteristics of oxygenation-sensitive MRI response to visual activations in humans. *Magn. Reson. Med.*, 36:912–919 (1998).

[23] Ernst T, Hennig J. Observation of a fast response in furnctional MR. *Magn. Reson. Med.*, 32:146–149 (1994).

[24] Menon RS, Ogawa S, Strupp JP, Anderson P, Uğurbil K. BOLD based functional MRI at 4 T includes a capillary bed contribution: echo-planar imaging correlates with previous optical imaging using intrinsic signal. *Magn. Reson. Med.*, 33:453–459 (1995).

[25] Hu X, Le TH, Uğurbil K. Evaluation of the early response in fMRI in individual subjects using short stimulus duration. *Magn. Reson. Med.*, 37:877–884 (1997).

[26] Yacoub E, Le TH, Uğurbil K, Hu X. Further evaluation of the initial negative response in functional magnetic resonance imaging. *Magn. Reson. Med.*, 41:436–441 (1999).

[27] Yacoub E, Hu X. Detection of the early decrease in fMRI signal in the motor area. *Magn. Reson. Med.*, 45:184–190 (2001).

[28] Yacoub E, Hu X. Detection of the early negative response in fMRI at 1.5 T. *Magn. Reson. Med.*, 41:1088–1092 (1999).

[29] Marota JA, Ayata C, Moskowitz MA, Weisskoff RM, Rosen BR, Mandeville JB. Investigation of the early response to rat forepaw stimulation. *Magn. Reson. Med.*, 41:247–252 (1999).

[30] Hathout GM, Varjavand B, Gopi RK. The early response in fMRI: a modeling approach. *Magn. Reson. Med.*, 41:550–554 (1999).

[31] Uğurbil K, Adriany G, Andersen P, Chen W, Garwood M, Gruetter R, Henry PG, Kim SG, Lieu H, Tkac I, Vaughan T, Van De Moortele PF, Yacoub E, Zhu XH. Ultrahigh field magnetic resonance imaging and spectroscopy. *Magn. Reson. Imaging*, 21:1263–1281 (2003).

[32] Ogawa S, Lee TM, Nayak A, Glynn P. Oxygenation-sensitive contrast in magnetic resonance image of rodent brain at high magnetic fields. *Magn. Reson. Med.*, 14:68–78 (1990).

[33] Ogawa S, Lee TM. Magnetic resonance imaging of blood vessels at high fields: in vivo and in vitro measurement and image simulation. *Magn. Reson. Med.*, 16:9–18 (1990).

[34] Ogawa S, Lee TM, Kay AR, Tank DW. Intrinsic signal changes accompanying sensory stimulation: functional brain mapping with magnetic resonance imaging. *Proc. Natl. Acad. Sci. USA*, 89:5951–5955 (1990).

[35] Blamire AM, Ogawa S, Uğurbil K, Rothman D, McCarthy G, Ellermann JM, Hyder F, Rattner Z, Shulman RG. Dynamic mapping of the human visual cortex by high-speed magnetic resonance imaging. *Proc. Natl. Acad. Sci. USA*, 89:11069–11073 (1992).

[36] Yoshizawa T, Nose T, Moore GJ, Sillerud LO. Functional magnetic resonance imaging of motor activation in the human cervical spinal cord. *Neuroimage*, 4:174–182 (1996).

[37] Stroman PW, Nance PW, Ryner LN. BOLD MRI of the human cervical spinal cord at 3 tesla. *Magn. Reson. Med.*, 42:571–576 (1999).

[38] Stroman PW, Ryner LN. Functional MRI of motor and sensory activation

in the human spinal cord. *Magn. Reson. Imaging*, 19:27–32 (2001).

[39] Stroman PW, Krause V, Malisza KL, Frankenstein UN, Tomanek B. Characterization of contrast changes in functional MRI of the human spinal cord at 1.5 T. *Magn. Reson. Imaging*, 19:833–838 (2001).

[40] Stroman PW, Krause V, Malisza KL, Frankenstein UN, Tomanek B. Functional magnetic resonance imaging of the human cervical spinal cord with stimulation of different sensory dermatomes. *Magn. Reson. Imaging*, 20:1–6 (2002).

[41] Stroman PW, Krause V, Malisza KL, Frankenstein UN, Tomanek B. Extravascular proton-density changes as a non-BOLD component of contrast in fMRI of the human spinal cord. *Magn. Reson. Med.*, 48:122–127 (2002).

[42] Stroman PW, Tomanek B, Krause V, Frankenstein UN, Malisza KL. Mapping of neuronal function in the healthy and injured human spinal cord with spinal fMRI. *Neuroimage*, 17:1854–1860 (2002).

[43] Stroman PW, Tomanek B, Malisza KL. Functional magnetic resonance imaging of the human brain and spinal cord by means of signal enhancement by extravascular protons. *Concepts in Magnetic Resonance Part A*, 16A:28–34 (2003).

[44] Stroman PW, Kornelsen J, Bergman A, Krause V, Ethans K, Malisza KL, Tomanek B. Noninvasive assessment of the injured human spinal cord by means of functional magnetic resonance imaging. *Spinal Cord*, 42:59–66 (2004).

[45] Kornelsen J, Stroman PW. fMRI of the lumbar spinal cord during a lower limb motor task. *Magn. Reson. Med.*, 52:411–414 (2004).

[46] Backes WH, Mess WH, Wilmink JT. Functional MR imaging of the cervical spinal cord by use of median nerve stimulation and fist clenching. *Am. J. Neuroradiol.*, 22:1854–1859 (2001).

[47] Stroman PW, Tomanek B, Krause V, Frankenstein UN, Malisza KL. Functional magnetic resonance imaging of the human brain based on signal enhancement by extravascular protons (SEEP fMRI). *Magn. Reson. Med.*, 49:433–439 (2003).

[48] Stroman PW, Malisza KL, Onu M. Functional magnetic resonance imaging at 0.2 Tesla. *Neuroimage*, 20:1210–1214 (2003).

[49] Giove F, Garreffa G, Giulietti G, Mangia S, Colonnese C, Maraviglia B. Issues about the functional MR Imaging of the human spinal cord. *Magn. Reson. Imaging*, 22:1505–1516 (2004).

[50] Kandel ER, Schwartz JH, Jessel TM. *Principles of neural sciences*. Elsevier, New York, 1991.

[51] Horner PJ, Gage FH. Regenerating the damaged central nervous system. *Nature*, 407:963–970 (2000).

[52] Woerly S, Doan VD, Evans-Martin F, Paramore CG, Peduzzi JD. Spinal cord reconstruction using NeuroGel implants and functional recovery after chronic injury. *J. Neurosci. Res.*, 66:1187–1197 (2001).

[53] Oudega M, Gautier SE, Chapon P, Fragoso M, Bates ML, Parel JM, Bunge MB. Axonal regeneration into Schwann cell grafts within resorbable poly(alpha-hydroxyacid) guidance channels in the adult rat spinal cord. *Biomaterials*, 22:1125–1136 (2001).

[54] Wickelgren I. Neuroscience. Animal studies raise hopes for spinal cord repair. *Science*, 297:178–181 (2002).

[55] Woerly S, Pinet E, de Robertis L, Van Diep D, Bousmina M. Spinal cord repair with PHPMA hydrogel containing RGD peptides (NeuroGel). *Biomaterials*, 22:1095–1111 (2001).

[56] Teng YD, Lavik EB, Qu X, Park KI, Ourednik J, Zurakowski D, Langer R, Snyder EY. Functional recovery following traumatic spinal cord injury mediated by a unique polymer scaffold seeded with neural stem cells. *Proc. Natl. Acad. Sci. USA*, 99:3024–3029 (2002).

[57] Bligth AR. Just one word: plasticity. *Nat. Neurosci.*, 7:206–208 (2004).

[58] Resnick DK, Schmitt C, Miranpuri GS, Dhodda VK, Isaacson J, Vemuganti R. Molecular evidence of repair and plasticity following spinal cord injury. *Neuroreport*, 15:837–839 (2004).

[59] Fouad K, Pearson K. Restoring walking after spinal cord injury. *Prog. Neurobiol.*, 73:107–126 (2004).

[60] Cheng H, Liao KK, Liao SF, Chuang TY, Shih YH. Spinal cord repair with acidic fibroblast growth factor as a treatment for a patient with chronic paraplegia. *Spine*, 29:E284–E288 (2004).

[61] Gomez-Anson B, MacManus DG, Parker GJ, Davie CA, Barker GJ, Moseley IF, McDonald WI, Miller DH. In vivo ^{1}H-magnetic resonance spectroscopy of the spinal cord in humans. *Neuroradiology*, 42:515–517 (2000).

[62] Cooke FJ, Blamire AM, Manners DN, Styles P, Rajagopalan B. Quantitative proton magnetic resonance spectroscopy of the cervical spinal cord. *Magn. Reson. Med.*, 51:1122–1128 (2004).

[63] Clark CA, Werring DJ, Miller DH. Diffusion imaging of the spinal cord in vivo: estimation of the principal diffusivities and application to multiple sclerosis. *Magn. Reson. Med.*, 43:133–138 (2000).

[64] Ries M, Jones RA, Dousset V, Moonen CT. Diffusion tensor MRI of the spinal cord. *Magn. Reson. Med.*, 44:884–892 (2000).

[65] Barker GJ. Diffusion-weighted imaging of the spinal cord and optic nerve. *J. Neurol. Sci.*, 186 Suppl. 1:S45–S49 (2001).

[66] Murphy BP, Zientara GP, Huppi PS, Maier SE, Barnes PD, Jolesz FA, Volpe JJ. Line scan diffusion tensor MRI of the cervical spinal cord in preterm infants. *J. Magn. Reson. Imaging*, 13:949–953 (2001).

[67] Clark CA, Werring DJ. Diffusion tensor imaging in spinal cord: methods and applications – a review. *NMR Biomed.*, 15:578–586 (2002).

[68] Wheeler-Kingshott CA, Hickman SJ, Parker GJ, Ciccarelli O, Symms MR, Miller DH, Barker GJ. Investigating cervical spinal cord structure

using axial diffusion tensor imaging. *Neuroimage*, 16:93–102 (2002).

[69] Cercignani M, Horsfield MA, Agosta F, Filippi M. Sensitivity-encoded diffusion tensor MR imaging of the cervical cord. *Am. J. Neuroradiol.*, 24:1254–1256 (2003).

[70] Mamata H, Jolesz FA, Maier SE. Characterization of central nervous system structures by magnetic resonance diffusion anisotropy. *Neurochem. Int.*, 45:553–560 (2004).

[71] Madi S, Flanders AE, Vinitski S, Herbison GJ, Nissanov J. Functional MR imaging of the human cervical spinal cord. *Am. J. Neuroradiol.*, 22:1768–1774 (2001).

[72] Schroth G, Klose U. Cerebrospinal fluid flow. I. Physiology of cardiac-related pulsation. *Neuroradiology*, 35:1–9 (1992).

[73] Schroth G, Klose U. Cerebrospinal fluid flow. II. Physiology of respiration-related pulsations. *Neuroradiology*, 35:10–15 (1992).

[74] Schroth G, Klose U. Cerebrospinal fluid flow. III. Pathological cerebrospinal fluid pulsations. *Neuroradiology*, 35:16–24 (1992).

[75] Mikulis DJ, Wood ML, Zerdoner OA, Poncelet BP. Oscillatory motion of the normal cervical spinal cord. *Radiology*, 192:117–121 (1994).

[76] Thron AK. *Vascular anatomy of the spinal cord: neurological investigations and clinical syndromes*, 8–64. Springer-Verlag, New York, 1988.

[77] Gati JS, Menon RS, Uğurbil K, Rutt BK. Experimental determination of the BOLD field strength dependence in vessels and tissue. *Magn. Reson. Med.*, 38:296–302 (1997).

[78] Pattany PM, Khamis IH, Bowen BC, Goodkin K, Weaver RG, Murdoch JB, Donovon Post MJ, Quencer RM. Effects of physiologic human brain motion on proton spectroscopy: quantitative analysis and correction with cardiac gating. *Am. J. Neuroradiol.*, 23:225–230 (2002).

[79] Jokich PM, Rubin JM, Dohrmann GJ. Intraoperative ultrasonic evaluation of spinal cord motion. *J. Neurosurg.*, 60:707–711 (1984).

[80] Levy LM. Evaluation of spinal cord function using functional MR Imaging with neurophysiological stimuli. *Am. J. Neuroradiol.*, 22:1811–1812 (2001).

[81] Lee KH, Chung TS, Jeon TJ, Kim YH, Chien D, Laub G. Application of spatial modulation of magnetization to cervical spinal stenosis for evaluation of the hydrodynamic changes occurring in cerebrospinal fluid. *Korean J. Radiol.*, 1:11–18 (2000).

[82] Itabashi T. Quantitative analysis of cervical CSF and syrinx fluid pulsations. *Nippon Seikeigeka Gakkai Zasshi*, 64:523–533 (1990).

[83] Henry-Feugeas MC, Idy-Peretti I, Blanchet B, Hassine D, Zannoli G, Schouman-Claeys E. Temporal and spatial assessment of normal cerebrospinal fluid dynamics with MR imaging. *Magn. Reson. Imaging*, 11:1107–1118 (1993).

[84] Enzmann DR, Pelc NJ. Normal flow patterns of intracranial and spinal

cerebrospinal fluid defined with phase-contrast cine MR imaging. *Radiology*, 178:467–474 (1991).

[85] Enzmann DR, Pelc NJ. Brain motion: measurement with phase-contrast MR imaging. *Radiology*, 185:653–660 (1992).

[86] Enzmann DR, Pelc NJ. Cerebrospinal fluid flow measured by phase-contrast cine MR. *Am. J. Neuroradiol.*, 14:1301–1307 (1993).

[87] Darian-Smith I, Johnson KO, Dykes R. "Cold" fiber population innervating palmar and digital skin of the monkey: responses to cooling pulses. *J. Neurophysiol.*, 36:325–346 (1973).

[88] LaMotte RH, Thalhammer JG. Response properties of high-threshold cutaneous cold receptors in the primate. *Brain Res.*, 244:279–287 (1982).

[89] Maier MA, Perlmutter SI, Fetz EE. Response patterns and force relations of monkey spinal interneurons during active wrist movement. *J. Neurophysiol.*, 80:2495–2513 (1998).

[90] Bandettini PA, Wong EC, Jesmanowicz A, Hinks RS, Hyde JS. Spin-echo and gradient-echo EPI of human brain activation using BOLD contrast: a comparative study at 1.5 T. *NMR Biomed.*, 7:12–20 (1994).

[91] Darquié A, Poline JB, Poupon C, Saint-Jalmes H, Le Bihan D. Transient decrease in water diffusion observed in human occipital cortex during visual stimulation. *Proc. Natl. Acad. Sci. USA*, 98:9391–9395 (2001).

[92] Stroman PW, Krause V, Frankenstein UN, Malisza KL, Tomanek B. Spin-echo versus gradient-echo fMRI with short echo times. *Magn. Reson. Imaging*, 19:827–831 (2001).

[93] Wehrli FW, MacFallJ R, Schutts D, Breger R, Herfkens RJ. Mechanism of contrast in NMR. *J. Comput. Assist. Tomogr.*, 8:369–380 (1984).

[94] Yacoub E, Duong TQ, Van De Moortele PF, Lindquist M, Adriany G, Kim SG, Uğurbil K, Hu X. Spin-echo fMRI in humans using high spatial resolutions and high magnetic fields. *Magn. Reson. Med.*, 49:655–664 (1996).

[95] Cox RW. AFNI: software for analysis and visualization of functional magnetic resonance neuroimages. *Comput. Biomed. Res.*, 29:162–173 (1996).

[96] Giove F, Mangia S, Garreffa G, Giulietti G, Colonnese C, Maraviglia B. Functional NMR imaging of the spinal cord at 1.5 T. In *Proceedings INFMeeting, National Conference on the Physics of the Matter*, 85–86. Genova, 23–25 June 2003.

[97] Giove F, Mangia S, Garreffa G, Giulietti G, Colonnese C, Maraviglia B. Functional MR imaging of the human spinal cord at 1.5 T. In 10^{th} *Annual Meeting of the Organization for Human Brain Mapping.*, vol. 22, Available on CD–ROM in NeuroImage. Budapest, 14–17 June 2004.

[98] Di Salle F, Formisano E, Linden DE, Bonavita S, Pepino A, Smaltino F, Tedeschi G. Exploring brain function with magnetic resonance imaging. *Eur. J. Radiol.*, 30:84–94 (1999).

[99] Detre JA, Leigh JS, Williams DS, Koretsky AP. Perfusion Imaging.

Magn. Reson. Med., 23:37–45 (1992).

[100] Kim SG, Tsekos NV. Perfusion imaging by a flow–sensitive alternating inversion recovery (FAIR) technique: application to functional brain imaging. *Magn. Reson. Med.*, 37:425–435 (1997).

[101] Buxton RB, Wong EC, Frank LR. Dynamics of blood flow and oxygenation changes during brain activation: the balloon model. *Magn. Reson. Med.*, 39:855–864 (1998).

[102] Buxton RB, Frank LR. A model for the coupling between cerebral blood flow and oxygen metabolism during neural stimulation. *J. Cereb. Blood Flow Metab.*, 17:64–72 (1997).

[103] Grubb RL Jr, Raichle ME, Eichling JO, Ter-Pogossian MM. The effects of changes in $PaCO_2$ on cerebral blood volume, blood flow, and vascular mean transit time. *Stroke*, 5:603–609 (1974).

[104] Mandeville JB, Marota JJ, Kosofsky BE, Keltner JR, Weissleder R, Rosen BR, Weisskoff RM. Dynamic functional imaging of relative cerebral blood volume during rat forepaw stimulation. *Magn. Reson. Med.*, 39:615–624 (1998).

[105] Mandeville JB, Marota JJ, Ayata C, Moskowitz MA, Weisskoff RM, Rosen BR. MRI measurement of the temporal evolution of relative CMR_{O_2} during rat forepaw stimulation. *Magn. Reson. Med.*, 42:944–951 (1999).

[106] Friston KJ, Mechelli A, Turner R, Price CJ. Nonlinear responses in fMRI: the Balloon model, Volterra kernels, and other hemodynamics. *Neuroimage*, 12:466–477 (2000).

[107] Mintun MA, Lundstrom BN, Snyder AZ, Vlassenko AG, Shulman GL, Raichle ME. Blood flow and oxygen delivery to human brain during functional activity: theoretical modeling and experimental data. *Proc. Natl. Acad. Sci. USA*, 98:6859–6864 (2001).

[108] Roland PE, Eriksson L, Stone-Elander S, Widen L. Does mental activity change the oxydative metabolism of the brain? *J. Neurosci.*, 7:2373–2389 (1987).

[109] Seitz RJ, Roland PE. Vibratory stimulation increases and decreases the regional cerebral blood flow and oxydative metabolism: a positron emission tomography (PET) study. *Acta Neurol. Scand.*, 86:60–67 (1992).

[110] Chen W, Novotny EJ, Zhu XH, Rothman DL, Shulman RG. Localized ^{1}H–NMR measurement of glucose consumption in the human brain visual stimulation. *Proc. Natl. Acad. Sci. USA*, 90:9896–9900 (1993).

[111] Marrett S *et al*. Stimulus specific increase of oxidative metabolism in human visual cortex. In *Quantification of brain function. Tracer kinetics and image analysis in brain PET*, edited by K Uemura, *et al.*, 217–224. Elsevier Science Publication, Amsterdam, 1993.

[112] Ribeiro L *et al*. Cerebral blood flow and metabolysm during nonspecific bilateral visual stimulation in normal subjects. In *Quantification of brain function. Tracer kinetics and image analysis in brain PET*, edited by K Uemura, *et al.*,

229–234. Elsevier Science Publication, Amsterdam, 1993.

[113] Blomqvist G, Seitz RJ, Sjogren I, Halldin C, Stone-Elander S, Widen L, Solin O, Haaparanta M. Regional cerebral oxidative and total glucose consumption during rest and activation studied with positron emission tomography. *Acta Physiol. Scand.*, 151:29–43 (1994).

[114] Madsen PL, Hasselbalch SG, Hagemann LP, Olsen KS, Bulow J, Holm S, Wildschiodtz G, Paulson OB, Lassen NA. Persistent resetting of the cerebral oxygen/glucose uptake ratio by brain activation: evidence obtained with the Kety–Schmidt technique. *J. Cereb. Blood Flow Metab.*, 15:485–491 (1995).

[115] Frahm J, Krueger G, Merboldt KD, Kleinschmidt A. Dynamic NMR studies of perfusion and oxidative metabolism during focal brain activation. *Adv. Exp. Med. Biol.*, 413:195–203 (1997).

[116] Marrett S *et al*. Differential increases of oxygen metabolism in visual cortex. *J. Cereb. Blood Flow Metab.*, 15 (suppl. 1):S80 (1995).

[117] Marrett S, Gjeddie A. Changes of blood flow and oxygen consumption in visual cortex of living humans. In *Optical Imaging of Brain Function and Metabolism II*, edited by A Villringer, *et al.*, 205–208. Plenum Press, New York, 1997.

[118] Kim SG, Uğurbil K. Comparison of blood oxygenation and cerebral blood flow effects in fMRI: estimation of relative oxygen consumption change. *Magn. Reson. Med.*, 38:59–65 (1997).

[119] Davis TL, Kwong KK, Weisskoff RM, Rosen BR. Calibrated functional MRI: mapping the dynamics of oxidative metabolism. *Proc. Natl. Acad. Sci. USA*, 95:1834–1839 (1998).

[120] Vafaee MS, Marrett S, Meyer E, Evans AC, Gjedde A. Increased oxygen consumption in human visual cortex: response to visual stimulation. *Acta Neurol. Scand.*, 98:85–89 (1998).

[121] Schwarzbauer C, Heinke W. Investigating the dependence of BOLD contrast on oxidative metabolism. *Magn. Reson. Med.*, 41:537–543 (1999).

[122] Kim SG, Rostrup E, Larsson HB, Ogawa S, Paulson OB. Determination of relative CMR_{O_2} from CBF and BOLD changes: significant increase of oxygen consumption rate during visual stimulation. *Magn. Reson. Med.*, 41:1152–1161 (1999).

[123] Kastrup A, Kruger G, Glover GH, Moseley ME. Assessment of cerebral oxidative metabolism with breath holding and fMRI. *Magn. Reson. Med.*, 42:608–611 (1999).

[124] Hoge RD, Atkinson J, Gill B, Crelier GR, Marrett S, Pike GB. Linear couplig between cerebral blood flow and oxygen consumption in activated human cortex. *Proc. Natl. Acad. Sci. USA*, 96:9403–9408 (1999).

[125] Chen W, Zhu XH, Gruetter R, Seaquist ER, Adriany G, Uğurbil K. Study of tricarboxylic acid cycle flux changes in human visual cortex during hemifield visual stimulation using ^{1}H-[^{13}C] MRS and fMRI. *Magn. Reson.*

Med., 45:349–355 (2001).

[126] Chhina N, Kuestermann E, Halliday J, Simpson LJ, Macdonald IA, Bachelard HS, Morris PG. Measurement of human tricarboxylic acid cycle rates during visual activation by ^{13}C magnetic resonance spectroscopy. *J. Neurosci. Res.*, 66:737–746 (2001).

[127] Kastrup A, Kruger G, Neumann-Haefelin T, Glover GH, Moseley ME. Changes of cerebral blood flow, oxygenation, and oxidative metabolism during graded motor activation. *Neuroimage*, 15:74–82 (2002).

[128] Giove F, Mangia S, Bianciardi M, Garreffa G, Di Salle F, Morrone R, Maraviglia B. The physiology and metabolism of neuronal activation: "in vivo" studies by NMR and other methods. *Magn. Reson. Imaging*, 21:1283–1293 (2003).

[129] Mintun MA, Raichle ME, Martin WR, Herscovitch P. Brain oxygen utilization measured with ^{15}O radiotracers and positron emission tomography. *J. Nucl. Med.*, 25:177–187 (1984).

[130] Gruetter R, Novotny EJ, Boulware SD, Mason GF, Rothman DL, Shulman GI, Prichard JW, Shulman RG. Localized ^{13}C NMR spectroscopy in the human brain of amino acid labeling from D–[1–^{13}C]glucose. *J. Neurochem.*, 63:1377–1385 (1994).

[131] Hyder F, Rothman DL, Mason GF, Rangarajan A, Behar KL, Shulman RG. Oxidative glucose metabolism in rat brain during single forepaw stimulation: a spatially localized ^{1}H [^{13}C] nuclear magnetic resonance study. *J. Cereb. Blood Flow Metab.*, 17:1040–1047 (1997).

[132] Zhu XH, Zhang Y, Tian RX, Lei H, Zhang N, Zhang X, Merkle H, Uğurbil, Chen W. Development of ^{17}O NMR approach for fast imaging of cerebral metabolic rate of oxygen in rat brain at high field. *Proc. Natl. Acad. Sci. USA*, 99:13194–13199 (2002).

[133] Li TQ, Haefelin TN, Chan B, Kastrup A, Jonsson T, Glover GH, Moseley ME. Assessment of hemodynamic response during focal neural activity in human using bolus tracking, arterial spin labeling and BOLD techniques. *Neuroimage*, 12:442–451 (2000).

[134] Hyder F, Kida I, Behar KL, Kennan RP, Maciejewski PK, Rothman DL. Quantitative functional imaging of the brain: towards mapping neuronal activity by BOLD fMRI. *NMR Biomed.*, 14:413–431 (2001).

[135] Wu G, Luo F, Li Z, Zhao X, Li SJ. ransient relationships among BOLD, CBV, and CBF changes in rat brain as detected by functional MRI. *Magn. Reson. Med.*, 48:987–993 (2002).

[136] Lee SP, Duong TQ, Yang G, Iadecola C, Kim SG. Relative changes of cerebral arterial and venous blood volumes during increased cerebral blood flow: implications for BOLD fMRI. *Magn. Reson. Med.*, 45:791–800 (2001).

[137] Duong TQ, Kim SG. In vivo MR measurements of regional arterial and venous blood volume fractions in intact rat brain. *Magn. Reson. Med.*, 43:393–402 (2000).

[138] An H, Lin W. Cerebral venous and arterial blood volumes can be estimated separately in humans using magnetic resonance imaging. *Magn. Reson. Med.*, 48:583–588 (2002).

[139] Villringer A, Planck J, Hock C, Schleinkofer L, Dirnagl U. Near infrared spectroscopy (NIRS): a new tool to study hemodynamic changes during activation of brain function in human adults. *Neurosci. Lett.*, 154:101–104 (1993).

[140] Villringer A, Chance B. Non–invasive optical spectroscopy and imaging of human brain function. *Trends Neurosci.*, 20:435–442 (1997).

[141] Frostig RD, Lieke EE, Ts'o DY, Grinvald A. Cortical functional architecture and local coupling between neuronal activity and the microcirculation revealed by in vivo high–resolution optical imaging of intrinsic signals. *Proc. Natl. Acad. Sci. USA*, 87:6082–6086 (1990).

[142] Silva AC, Lee SP, Iadecola C, Kim SG. Early temporal characteristics of cerebral blood flow and deoxyhemoglobin changes during somatosensory stimulation. *J. Cereb. Blood Flow Metab.*, 20:201–206 (2000).

[143] Lindauer U, Royl G, Leithner C, Kuhl M, Gold L, Gethmann J, Kohl–Bareis M, Villringer A, Dirnagl U. No evidence for early decrease in blood oxygenation in rat whisker cortex in response to functional activation. *Neuroimage*, 13:988–1001 (2001).

[144] Jones M, Berwick J, Johnston D, Mayhew J. Concurrent optical imaging spectroscopy and laser–Doppler flowmetry: the relationship between blood flow, oxygenation, and volume in rodent barrel cortex. *Neuroimage*, 13:1002–1015 (2001).

[145] Mayhew J, Johnston D, Berwick J, Jones M, Coffey P, Zheng Y. Spectroscopic analysis of neural activity in brain: increased oxygen consumption following activation of barrel cortex. *Neuroimage*, 12:664–675 (2000).

[146] Mayhew J, Johnston D, Martindale J, Jones M, Berwick J, Zheng Y. Increased oxygen consumption following activation of brain: theoretical footnotes using spectroscopic data from barrel cortex. *Neuroimage*, 13:975–987 (2001).

[147] Hyder F, Shulman RG, Rothman DL. A model for the regulation of cerebral oxygen delivery. *J. Appl. Physiol.*, 85:554–564 (1998).

[148] Buxton RB. The elusive initial dip. *Neuroimage*, 13:953–958 (2001).

[149] Vanzetta I, Grinvald A. Increased cortical oxydative metabolism due to sensory stimulation: Implications for functional brain imaging. *Science*, 286:1555–1558 (1999).

[150] Obrig H, Hirth C, Junge–Hulsing JG, Doge C, Wolf T, Dirnagl U, Villringer A. Cerebral oxygenation changes in response to motor stimulation. *J. Appl. Physiol.*, 81:1174–1183 (1996).

[151] Michaelis T, Merboldt K, Bruhn H, Hanicke W, Frahm J. Absolute concentrations of metabolites in the adult human brain in vivo: quantification of localized proton MR spectra. *A. Radiology*, 187:219–227 (1993).

[152] Tkác I, Andersen P, Adriany G, Merkle H, Uğurbil K, Gruetter R. In Vivo ^{1}H MRS Spectroscopy of the human brain at 7 T. *Magn. Reson. Med.*, 46:451–456 (2001).

[153] Tkác I, Henry PG, Andersen P, Keene CD, Low WC, Gruetter R. Highly resolved in vivo ^{1}H NMR spectroscopy of the mouse brain at 9.4 T. *Magn. Reson. Med.*, 52:478–84 (2004).

[154] Trabesinger AH, Meier D, Boesiger P. In vivo ^{1}H NMR spectroscopy of individual human brain metabolites at moderate field strengths. *Magn. Reson. Imaging*, 21:1295–302 (2003).

[155] Srinivasan R, Vigneron D, Sailasuta N, Hurd, R, Nelson S. A comparative study of myo-inositol quantification using LCModel at 1.5 T and 3.0 T with 3D ^{1}H proton spectroscopic imaging of the human brain. *Magn. Reson. Imaging*, 22:523–528 (2004).

[156] Mierisova S, Ala-Korpela M. MR spectroscopy quantitation: a review of frequency domain methods. *NMR Biomed.*, 14:247–259 (2001).

[157] Vanhamme L, Sundin T, Hecke PV, Huffel SV. MR spectroscopy quantitation: a review of time-domain methods. *NMR Biomed.*, 14:233–246 (2001).

[158] van den Boogaart A, Ala-Korpela M, Jokisaari J, Griffiths JR. Time and frequency domain analysis of NMR data compared: an application to 1D 1^{H} spectra of lipoproteins. *Magn. Reson. Med.*, 31:347–358 (1994).

[159] Stephenson DS. Linear prediction and maximum entropy methods in NMR spectroscopy. *Prog. NMR Spectrosc.*, 20:515–626 (1988).

[160] Pijnappel WWF, van den Boogaart A, de Beer R, van Ormondt D. SVD–based quantification of magnetic resonance signals. *J. Magn. Reson.*, 97:122–134 (1992).

[161] Young K, Govindaraju V, Soher BJ, Maudsley AA. Automated spectral analysis. I. Formation of a priori information by spectral simulation. *Magn. Reson. Med.*, 40:812–815 (1998).

[162] Slotboom J, Boesch C, Kreis R. Versatile frequency domain fitting using time domain models and prior knowledge. *Magn. Reson. Med.*, 39:899–911 (1998).

[163] Provencher SW. Estimation of metabolite concentrations from localized in vivo proton NMR spectra. *Magn. Reson. Med.*, 30:672–679 (1993).

[164] Provencher SW. Automatic quantitation of localized in vivo ^{1}H spectra with LCModel. *NMR Biomed.*, 14:260–4 (2001).

[165] Vanhamme L, van den Boogaart A, Van Huffel S. Improved method for accurate and efficient quantification of MRS data with use of priori–knowledge. *J. Magn. Reson.*, 129:35–43 (1997).

[166] Van den Boogaart A, Van Hecke A, Van Huffel P, Graveron-Demilly S, Van Ormondt D, de Beer R. MRUI: a graphical user interface for accurate routine MRS data analysis. In *Proceedings of the European Society of Magnetic Resonance in Medicine and Biology 13th Annual Meeting*, 318. Prague, 1996.

[167] Provencher SW. *LCModel & LCMgui user's manual*. http://S-provencher.com (2004).

[168] Govindaraju V, Young K, Maudsley AA. Proton NMR chemical shifts and coupling constants for brain metabolites. *NMR Biomed.*, 13:129–153 (2000).

[169] The MathWorks, Inc. *Matlab*. http://www.mathworks.com.

[170] Klose U. In vivo proton spectroscopy in presence of eddy currents. *Magn. Reson. Med.*, 14:26–30 (1990).

[171] Frahm J, Bruhn H, Gyngell ML, Merboldt KD, Hanicke W, Sauter R. Localized proton NMR Spectrosopy in different regions of the human brain in vivo. Relaxation times and concentrations of cerebral metabolites. *Magn. Reson. Med.*, 11:47–63 (1989).

[172] Cavassila S, Deval S, Huegen C, van Ormondt D, Graveron-Demilly D. Cramér–Rao bounds: an evaluation tool for quantitation. *NMR Biomed.*, 14:278–83 (2001).

[173] Macrì MA, Garreffa G, Giove F, Guardati M, Ambrosini A, Colonnese C, Maraviglia B. In vivo quantitative ^{1}H–MRS of cerebellum and evaluation of quantitation reproducibility by simulation of different levels of noise and spectral resolution. *Magn. Reson. Imaging*, 22:1385–1393 (2004).

[174] Hennig J, Pfister H, Ernst T, Ott D. Direct absolute quantification of metabolites in the human brain with in vivo localized proton spectroscopy. *NMR Biomed.*, 5:193–9 (1992).

[175] van Zijl PC, Moonen CT. In situ changes in purine nucleotide and N–acetyl concentrations upon inducing global ischemia in cat brain. *Magn. Reson. Med.*, 29:381–385 (1993).

[176] Klunk WE, Xu C, Panchalingam K, McClure RJ, Pettegrew JW. Quantitative ^{1}H and ^{31}P MRS of PCA extracts of postmortem Alzheimer's disease brain. *Neurobiol. Aging*, 17:349–57 (1996).

[177] Kanowski M, Kaufmann J, Braun J, Bernarding J, Tempelmann C. Quantitation of simulated short echo time ^{1}H human brain spectra by LCModel and AMARES. *Magn. Reson. Med.*, 51:904–12 (2004).

[178] Hofmann L, Slotboom J, Jung B, Maloca P, Boesch C, Kreis R. Quantitative ^{1}H-magnetic resonance spectroscopy of human brain: Influence of composition and parameterization of the basis set in linear combination model-fitting. *Magn. Reson. Med.*, 48:440–53 (2002).

[179] Pfeuffer J, Tkác I, Provencher SW, Gruetter R. Toward an in vivo neurochemical profile: quantification of 18 metabolites in short echo–time ^{1}H–NMR spectra of the rat brain. *J. Magn. Reson.*, 141:104–20 (1999).

[180] Russel MB, Rasmussen BK, Thorvaldsen P, Olesen J. Prevalence and sex–ratio of the subtypes of migraine. *Int. J. Epidemiol.*, 24:612–618 (1995).

[181] Headache Classification Committee of the International Headache Society. Classification and diagnostic criteria for headache disorders, cranial neuralgias and facial pain. *Cephalalgia*, 8:1–96 (1988).

[182] Volsen SG, Day NC, McCormack AL, Smith W, Craig PJ, Beattie R, Ince PJ, Shaw PJ, Ellis SB, Gillespie A, Harpold MM, Lodge D. The expression of neuronal voltage–dependent calcium channels in human cerebellum. *Mol. Brain Res.*, 34:271–282 (1995).

[183] Barbiroli B, Montagna P, Cortelli P, Funicello R, Iotti S, Monari L, Pierangeli G, Zaniol P, Lugaresi E. bnormal brain and muscle energy metabolism shown by ^{31}P magnetic resonance spectroscopy in patients affected by migraine with aura. *Neurology*, 42:1209–1214 (1992).

[184] Naressi A, Couturier C, Devos JM, Janssen M, Mangeat C, de Beer R, Graveron–Demilly D. Java–based Graphical User Interface for the MRUI Quantitation Package. *MAGMA*, 12:141–152 (2001).

[185] Mierisova S, van den Boogaart A, Tkác I, Van Hecke P, Vanhamme L, Liptaj T. New approach for quantitation of short echo time in vivo ^{1}H MR spectra of brain using AMARES. *NMR Biomed.*, 11:32–39 (1998).

[186] Macrì MA, Garreffa G, Giove F, Ambrosini A, Guardati M, Pierelli F, Schoenen J, Colonnese C, Maraviglia B. Cerebellar metabolite alterations detected in vivo by proton MR spectroscopy. *Magn. Reson. Imaging*, 21:1201–1206 (2003).

[187] Ashcroft FM. *Ion channels and disease. Channelopathies.* Academic Press, San Diego, 2000.

[188] Berridge MJ. Neuronal calcium signalling. *Neuron*, 21:13–26 (1998).

[189] Siesjo B. *Brain energy metabolism.* Wiley, New York, 1978.

[190] Mason GF, Gruetter R, Rothman DL, Behar KL, Shulman RG, Novotny EJ. Simultaneous determination of the rates of the TCA cycle, glucose utilization, alpha-ketoglutarate/glutamate exchange, and glutamine synthesis in human brain by NMR. *J. Cereb. Blood Flow Metab.*, 15:12–25 (1995).

[191] Cohen DM, Wei J, O'Brian Smith E, Gao X, Quast MJ, Sokoloff L. A method for measuring cerebral glucose metabolism in vivo by ^{13}C–NMR spectroscopy. *Magn. Reson. Med.*, 48:1063–1067 (2002).

[192] Merboldt KD, Bruhn H, Hanicke W, Michaelis T, Frahm J. Decrease of glucose in the human visual cortex during photic stimulation. *Magn. Reson. Med.*, 25:187–194 (1992).

[193] Madsen PL, Cruz NF, Sokoloff L, Dienel GA. Cerebral oxygen/glucose ratio is low during sensory stimulation and rises above normal during recovery: excess glucose consumption during stimulation is not accounted for by lactate efflux from or accumulation in brain tissue. *J. Cereb. Blood Flow Metab.*, 19:393–400 (1999).

[194] Fellows LK, Boutelle MG. Rapid changes in extracellular glucose levels and blood flow in the striatum of the freely moving rat. *Brain Res.*, 604:225–231 (1993).

[195] Dienel GA, Hertz L. Glucose and lactate metabolism during brain activation. *J. Neruosci. Res.*, 66:824–838 (2001).

[196] Jenkins BG, Belliveau JW, Rosen BR. Confirmation of lactate production during photic stimulation. Improved protocols using inter– and intra–subject averaging. In *Book of abstracts:* 11^{th} *annual scientific meeting SMRM*, vol. 2, 2145. 1992.

[197] Singh M, Kim H, Huang H, Kim T. Effect of stimulus rate on lactate in the human auditory cortex. In *Book of abstracts:* 11^{th} *annual scientific meeting SMRM*, vol. 2, 2146. 1992.

[198] Kuwabara T, Watanabe H, Tsuji S, Yuasa T. Lactate rise in the basal ganglia accompanying finger movements: a localized ^{1}H–MRS study. *Brain Res.*, 670:326–328 (1995).

[199] Menon RS, Gati JS. Two second temporal resolution measurements of lactate correlate with EPI BOLD fMRI timecourses during photic stimulation. In *Book of abstracts:* 5^{th} *annual meeting of International Society for Magnetic Resonance in Medicine*, 152. 1997.

[200] Najm IM, Wang Y, Shedid D, Luders HO, Ng TC, Comair YG. MRS metabolic markers of seizures and seizure–induced neuronal damage. *Epilepsia*, 39:244–250 (1998).

[201] Chatham JC, Forder JR. Lactic acid and protein interactions: implications for the NMR visibility of lactate in biological systems. *Biochem. Biophys. Acta*, 1426:177–184 (1999).

[202] Kuhr WG, Korf J. Extracellular lactic acid as an indicator of brain metabolism: continuous online measurement in conscious, freely moving rats. *J. Cereb. Blood Flow Metab.*, 8:130–137 (1988).

[203] Fellows LK, Boutelle MG, Fillenz M. Physiological stimulation increases nonoxidative glucose metabolism in the brain of the freely moving rat. *J. Neurochem.*, 60:1258–1263 (1993).

[204] Attwell D, Laughlin SB. An Energy Budget for Signaling in the Grey Matter of the Brain. *J. Cereb. Blood Flow Metab.*, 21:1133–1145 (2001).

[205] Aubert A, Costalat R. A model of the coupling between brain electrical activity, metabolism, and hemodynamics: application to the interpretation of functional neuroimaging. *Neuroimage*, 17:1162–1181 (2002).

[206] Magistretti PJ, Hof PR, Martin JL. Adenosine stimulates glycogenolysis in mouse cerebral cortex: a possible coupling mechanism between neuronal activity and energy metabolism. *J. Neurosci.*, 6:2558–2562 (1986).

[207] Murphy S, Pearce B. Functional receptors for neurotransmitters on astroglial cells. *Neuroscience*, 22:381–394 (1987).

[208] Morgello S, Uson RR, Schwartz EJ, Haber RS. The human blood–brain–barrier glucose transporter (GLUT1) is a glucose transporter of gray matter astrocytes. *Glia*, 14:43–54 (1995).

[209] Pellerin L, Pellegri G, Bittar PG, Charnay Y, Bouras C, Martin JL, Stella N, Magistretti PJ. Evidence supporting the existence of an activity–dependent astrocyte–neuron lactate shuttle. *Dev. Neurosci.*, 20:291–299 (1998).

[210] Bliss TM, Sapolsky RM. Interactions among glucose, lactate and adenosine regulate energy substrate utilization in hippocampal cultures. *Brain Res.*, 134:134–141 (2001).

[211] Schurr A, Payne RS, Miller JJ, Rigor BM. Glia are the main source of lactate utilized by neurons for recovery of function posthypoxia. *Brain Res.*, 774:221–224 (1997).

[212] Schurr A, Payne RS, Miller JJ, Rigor BM. Brain lactate, not glucose, fuels the recovery of synaptic function from hypoxia upon reoxygenation: an in vitro study. *Brain Res.*, 774:105–111 (1997).

[213] Yamagata K, Tagami M, Ikeda K, Noguchi T, Yamori Y, Nara Y. Reduced production of lactate during hypoxia and reoxygenation in astrocytes isolated from stroke–prone spontaneously hypertensive rats. *Neurosci. Lett.*, 296:113–116 (2000).

[214] Chen T, Qian YZ, Rice A, Zhu JP, Di X, Bullock R. Brain lactate uptake increases at the site of impact after traumatic brain injury. *Brain Res.*, 861:281–287 (2001).

[215] Tootell RB, Silverman MS, Hamilton SL, Switkes E, De Valois RL. Functional anatomy of macaque striate cortex. V. Spatial frequency. *J. Neurosci.*, 8:1610–1624 (1988).

[216] Magistretti PJ. Cellular basis of functional brain Imaging: insights from neuron–glia metabolic coupling. *Brain Res.*, 886:108–112 (2000).

[217] Chih CP, He J, Sly TS, Roberts EL Jr. Comparison of glucose and lactate as substrate during NMDA–induced activation of hippocampal slices. *Brain Res.*, 893:143–154 (2001).

[218] Vannucci SJ, Maher F, Simpson IA. Glucose transporter proteins in brain: delivery of glucose to neurons and glia. *Glia*, 21:2–21 (1997).

[219] Takahashi S, Driscoll BF, Law MJ, Sokoloff L. Role of sodium and potassium ions in regulation of glucose metabolism in cultured astroglia. *Proc. Natl. Acad. Sci. USA*, 92:4616–4620 (1995).

[220] Pierre K, Pellerin L, Debernardi R, Riederer BM, Magistretti PJ. Cell–specific localization of monocarboxylate transporters, MCT1 and MCT2, in the adult mouse brain revealed by double immunohistochemical labeling and confocal microscopy. *Neuroscience*, 100:617–627 (2000).

[221] Gjedde A, Marett S. Glycolysis in neurons, not astrocytes, delays oxidative metabolism of human visual cortex during sustained checkerboard stimulation in vivo. *J. Cereb. Blood Flow Metab.*, 21:1384–1392 (2001).

[222] Yang Y, Engelien W, Pan H, Xu S, Silbersweig DA, Stern E. CBF–based event–related brain activation paradigm: characterization of impulse–response function and comparison to BOLD. *Neuroimage*, 12:287–297 (2000).

[223] Chih CP, Lipton P, Roberts EL Jr. Do active cerebral neurons really use lactate rather than glucose? *Trends Neurosci.*, 24:573–578 (2001).

[224] Takata T, Sakurai T, Yang B, Yokono K, Okada Y. Effect of lactate on

the synaptic potential, energy metabolism, calcium homeostasis and extracellular glutamate concentration in the dentate gyrus of the hippocampus from Guinea–pig. *Neuroscience*, 104:371–378 (2001).

[225] Hydon PG. Glia: listening and talking to the synapse. *Nat. Rev. Neurosci.*, 2:185–193 (2001).

[226] Magistretti PJ, Pellerin L, Rothman DL, Shulman RG. Energy on demand. *Science*, 283:496–497 (1999).

[227] Kasischke KA, Vishwasrao HD, Fisher PJ, Zipfel WR, Webb WW. Neural activity triggers neuronal oxidative metabolism followed by astrocytic glycolysis. *Science*, 305:99–103 (2004).

[228] Hu YB, Wilson GS. A temporary local energy pool coupled to neuronal activity: fluctuations of extracellular lactate levels in rat brain monitored with rapid-response enzyme-based sensor. *J. Neurochem*, 69:1484–1490 (1997).

[229] Pietrini P, Guazzelli M, Basso G, Jaffe K, Grafman J. Neural correlates of imaginal aggressive behavior assessed by positron emission tomography in healthy subjects. *Am. J. Psychiatry*, 157:1772–1781 (2000).

[230] Raichle ME, MacLeod AM, Snyder AZ, Powers WJ, Gusnard DA, Shulman GL. A default mode of brain function. *Proc. Natl. Acad. Sci. USA*, 98:676–682 (2001).

[231] Mazoyer B, Zago L, Mellet E, Bricogne S, Etard O, Houde O, Crivello F, Joliot M, Petit L, Tzourio–Mazoyer N. Cortical networks for working memory and executive functions sustain the conscious resting state in man. *Brain Res. Bull.*, 54:287–298 (2001).

[232] Laurienti PJ, Burdette JH, Wallace MT, Yen YF, Field AS, Stein BE. Deactivation of sensory–specific cortex by cross-modal stimuli. *J. Cogn. Neurosci.*, 14:420–429 (2002).

[233] Pochon JB, Levy R, Fossati P, Lehericy S, Poline JB, Pillon B, Le Bihan D, Dubois B. The neural system that bridges reward and cognition in humans: an fMRI study. *Proc. Natl. Acad. Sci. USA*, 99:5669–5674 (2002).

[234] Harel N, Lee SP, Nagaoka T, Kim DS, Kim SG. Origin of negative blood oxygenation level–dependent fMRI signals. *J. Cereb. Blood Flow Metab.*, 22:908–917 (2002).

[235] Shmuel A, Yacoub E, Pfeuffer J, Van de Moortele PF, Adriany G, Hu X, Uğurbil K. Sustained negative BOLD, blood flow and oxygen consumption response and its coupling to the positive response in the human brain. *Neuron*, 36:1195–1210 (2002).

[236] Gusnard DA, Raichle ME, Raichle ME. Searching for a baseline: functional imaging and the resting human brain. *Nat. Rev. Neurosci.*, 2:685–694 (2001).

[237] Batjer HH, Devous MD Sr, Seibert GB, Purdy PD, Ajmani AK, Delarosa M, Bonte FJ. Intracranial arteriovenous malformation: contralateral steal phenomena. *Neurol. Med. Chir.*, 29:401–406 (1989).

[238] Yang Y, Frank JA, Hou L, Ye FQ, McLaughlin AC, Duyn JH. Multislice imaging and quantitative cerebral perfusion with pulsed arterial spin labeling. *Magn. Reson. Med.*, 39:825–832 (1998).

[239] Luh WM, Wong EC, Bandettini PA, Ward BD, Hyde JS. Comparison of simultaneously measured perfusion and BOLD signal increases during brain activation with T_1–based tissue identification. *Magn. Reson. Med.*, 44:137–143 (2000).

[240] Pfeuffer J, Adriany G, Shmuel A, Yacoub E, Van De Moortele PF, Hu X, Uğurbil K. Perfusion–based high–resolution functional imaging in the human brain at 7 Tesla. *Magn. Reson. Med.*, 47:903–911 (2002).

[241] Mangia S, Di Salle F, Garreffa G, Esposito F, Giove F, Cirillo S, Morrone R, Maraviglia B. Perfusion–based fMRI in the study of a pathological model for neuronal deactivation. *Brain Res. Bull.*, 63:1–5 (2004).

[242] Lee SP, Silva AC, Kim SG. Comparison of diffusion–weighted high–resolution CBF and spin–echo BOLD fMRI at 9.4 T. *Magn. Reson. Med.*, 47:736–741 (2002).

[243] Gold L, Lauritzen M. Neuronal deactivation explains decreased cerebellar blood flow in response to focal cerebral ischemia or suppressed neocortical function. *Proc. Natl. Acad. Sci. USA*, 99:7699–7704 (2002).

This PhD Thesis was typeset with LaTeX 2_ε